

**NASA CONTRACTOR
REPORT**



NASA CR-13

0060450



NASA CR-1365

LOAN COPY: RETURN TO
AFWL (WLIL-2)
KIRTLAND AFB, N MEX

**SYNTHESIS OF OPTIMUM
STRUCTURAL DESIGNS FOR
CONICAL AND TENSION SHELL
MARS ENTRY CAPSULES**

by Gerald A. Cohen, Richard M. Foster, and James R. Dowty

Prepared by
PHILCO-FORD CORPORATION
Newport Beach, Calif.
for Langley Research Center



SYNTHESIS OF OPTIMUM STRUCTURAL DESIGNS
FOR CONICAL AND TENSION SHELL
MARS ENTRY CAPSULES

By Gerald A. Cohen, Richard M. Foster, and James R. Dowty

Distribution of this report is provided in the interest of information exchange. Responsibility for the contents resides in the author or organization that prepared it.

Prepared under Contract No. NAS 1-5554-4 by
PHILCO-FORD CORPORATION
Newport Beach, Calif.

for Langley Research Center

NATIONAL AERONAUTICS AND SPACE ADMINISTRATION



PREFACE

This study was initiated while the authors were employed by Philco-Ford Corporation. Technical responsibility for the completion of the work and the preparation of this report resides in Structures Research Associates under subcontract to Philco-Ford. The contribution of Charles G. Dietz, who assisted in the analysis, is gratefully acknowledged.

ABSTRACT

Optimum design procedures are developed for lightweight, low ballistic coefficient entry capsules of both sandwich and ring-stiffened construction. These procedures are used to obtain specific point designs for 120° blunted cone and OA.833 tension shell capsule configurations. Aeroshell and base ring weight correlations are presented for the 120° sandwich cones. The effects of variation in structural temperature, ballistic coefficient, peak dynamic pressure, capsule size, and structural material are considered.



CONTENTS

	Page
SUMMARY	1
INTRODUCTION	3
SYMBOLS	4
FLOW FIELD ANALYSIS	7
Pressure Loads	7
Analytical methods	7
Results	9
120° sphere-cone	9
OA.833 tension shell	9
OA.833 tension shell at angle of attack	10
OA.65 tension shell	11
140° sphere-cone	11
Spherical dish	11
Convective Heating Rate Distributions	12
Analytical methods	12
Results	15
120° and 140° sphere-cones and spherical dish.	15
OA.65 and OA.833 tension shells	16
AEROSHELL STRUCTURAL SYNTHESIS	16
Analytical Methods	16
Design-analysis iteration procedure	16
Aeroshell loads	17
Conical capsules	18
Tension shell capsules	18
Base ring and payload ring design	18
Shell design	19
Sandwich cone	20
Ring-stiffened cone	22
Ring and stringer-stiffened tension shell	23
Shell analysis	24
Heat shield weights	25
Results	25
Point designs	25
Sandwich cones	26
Ring-stiffened cones	26
Tension shells	27
Configuration comparison	28
Aeroshell weight correlation	29
Effect of size and dynamic pressure	30
Effect of material	31
DESIGN EVALUATION	31
Fabrication Feasibility	31

Manufacturing processes and facilities	31
Material availability	32
Forming of structural elements	32
Joining and attaching techniques	33
Fabrication of large shell structures	34
Alternate section for aeroshell base ring	35
Detail Drawings of Optimized Designs	35
Honeycomb sandwich cone	35
Ring-stiffened cone	36
OA.833 tension shell	36
CONCLUDING REMARKS	37
APPENDIX - COMPARISON OF THEORETICAL FLOW FIELD RESULTS WITH EXPERIMENT	38
REFERENCES	42
TABLES	45
FIGURES	55

SYNTHESIS OF OPTIMUM STRUCTURAL DESIGNS

FOR

CONICAL AND TENSION SHELL

MARS ENTRY CAPSULES

by

Gerald A. Cohen, Richard M. Foster, and James R. Dowty

Structures Research Associates and Philco-Ford Corporation,

Newport Beach, California

SUMMARY

Optimum design procedures are developed for lightweight, low ballistic coefficient entry capsules of both sandwich and ring-stiffened construction. Essentially, the method developed consists of an iteration between design, based on certain approximations, and analysis, evaluating and modifying these approximations. The analysis is performed by existing shell analysis computer programs. The design step for the ring-stiffened capsules necessitated the development of a new computer program. This program allows variable ring size and spacing distributions, and trades off ring weight with shell skin weight to achieve minimum total weight.

Using these procedures, specific capsule designs have been obtained for 120° blunted cone and OA.833 tension shell geometries. These designs are based on pressure and convective heating rate distributions obtained analytically for out-of-orbit Martian entry trajectories. As is consistent with the shroud limitation of the Saturn V booster, the designs have 19 foot base diameters. Ballistic coefficients of $\beta = 0.32$ and 0.64 slug/ft² are considered, and the structure heat shield weight trade-off is studied by considering structural temperatures of both 300°F and 550°F . For the conical geometry, both sandwich and ring-stiffened construction is treated, whereas, for reasons of fabrication feasibility, only ring-stiffened tension shells are considered.

Comparison of the designs obtained reveals the following three main conclusions of this study:

1) The lower structural temperature is best - the reduction in heat shield weight in designing for 550^oF does not compensate for the increase in structural weight.

2) Because of minimum face sheet gage and adhesive weight limitations on the sandwich cones, optimized ring-stiffened construction is lighter at the low ballistic coefficient, whereas sandwich construction is lighter at the high ballistic coefficient. Assuming a linear variation of the nonusable (total structure plus heat shield) entry weight with the ballistic coefficient in the range of $0.32 \leq \beta \leq 0.64$ slug/ft², it follows that for $\beta < 0.42$ slug/ft², ring-stiffened construction is lighter than sandwich construction.

3) The nonusable entry weights for the tension shell designs are generally greater than those for the corresponding cone designs. However, because of their larger computed drag coefficient and consequent larger total entry weights, they have significantly larger usable entry weights. Since, however, the flow field analysis does not allow for the possibility of flow separation, which may occur on the tension shell, the tension shell results cannot be considered as reliable as those for the conical capsules.

In order to bare the effects of material, size, and peak dynamic pressure variation, the structural weights of the low temperature sandwich cones have been correlated algebraically. This correlation is displayed graphically with respect to base diameter and dynamic pressure for aluminum material, and tabularly with respect to several materials for typical values of base diameter and dynamic pressure.

Additional pressure and heat transfer distributions were obtained for several other candidate aeroshell shapes, viz. 140^o cone, 60^o spherical dish, and OA.65 tension shell.

INTRODUCTION

Because of the tenuous nature of the Martian atmosphere, conventional entry capsule designs are not applicable to Mars missions. As discussed in Reference 1, very low ballistic coefficients, for which structural weight is a limiting factor, are necessary to meet system requirements. Under these conditions, the aeroshell design significantly affects the residual entry weight available for the landed payload.

In Reference 2 are presented several preliminary aeroshell designs for out-of-orbit entry into the Mars atmosphere. These designs, which are based on the geometric shapes of a 120° cone and OA.833 tension shell, represent a first attempt based on a trial and error approach, and are not, in any sense, optimum. The present study is a sequel to Reference 2, towards the goal of achieving optimum aeroshell design. Specifically, the objectives of this study are fourfold;

- 1) Develop the methodology for optimum design of low ballistic coefficient entry capsules,
- 2) Obtain for Martian orbit entry optimum point designs for the geometric configurations considered in Reference 2,
- 3) Investigate the trade-offs related to variation in structural temperature and ballistic coefficient, and
- 4) Develop parametric structural weight correlations - manifesting the effects of size, peak dynamic pressure, and material selection - for use in future system studies.

As in Reference 2, the point designs are conservatively based on peak dynamic pressure loads associated with an uncontrolled tumbling mode entry trajectory. The 120° cone pressure distribution used was computed by the steady state method of integral relations and is taken from Reference 2. On the other hand, because of the inability of this method to treat the tension shell accurately, the OA.833 tension shell pressure distribution was recalculated by a more accurate computer program which obtains the steady state flow as a limiting solution of the transient flow equations.

Only designs which meet the constraint of fabrication feasibility are considered. However, the presented designs, which are defined in sufficient detail for the prediction of structure and heat shield weight, are not necessarily defined in the detail required for actual fabrication. This is particularly true at the payload interface since the payload itself, is as yet undefined. It is noted further that, although the effect of temperature on material properties was considered, the effect of thermal stress was neglected in this study.

SYMBOLS

C	general instability correlation factor
C_A	axial force coefficient
C_D	drag coefficient
d_T	rivet diameter, in.
d	local value of interior ring spacing, in.
E	Young's modulus, psi; or total fluid energy, BTU/lb
e	internal energy, BTU/lb
f_R	riveted flange width, in.
H	stagnation enthalpy, BTU/lb
h	thickness of Z-section interior ring, in.; or enthalpy, BTU/lb
I	base ring moment of inertia, in. ⁴
L	meridional length of truncated aeroshell, in.
l	ideal cross section perimeter of Z-section interior ring, in.
M	number of interior rings
N	circumferential harmonic number
N_C	critical value of N
P	axial load, lb
P_O	critical value of P for pure axial loading, lb
p	(critical) pressure, psi or psf
p_O	critical value of p for pure hydrostatic pressure loading, psi
q	convective heat transfer rate, BTU/ft ² -sec

q_d	maximum dynamic pressure, psf
R	cross-sectional radius of tubular base ring, in.
r	radial distance from axis of revolution, in.
\bar{R}_N	spherical nose radius of curvature, ft or in.
\bar{R}_2	average radius of curvature, in.
Re	Reynolds number
s	meridional distance from spherical nose, ft
T	Temperature, $^{\circ}F$ or $^{\circ}K$
t	thickness, in.; or time, sec
u, v	velocity components in axial and radial directions, respectively, fps
V	flight velocity, fps
u	meridional velocity component, fps
W	weight, lb
w	normal deflection of buckling mode, in.; or circumferential velocity component, fps
X	mole fraction
x	axial distance from spherical nose, ft
x	axial distance from tension shell base
z	distance measured along normal to shell surface, ft
α	angle of attack, deg; or cone half-angle, deg
β	ballistic coefficient, slug/ft ²
γ	specific heat ratio
Δ	increase in riveted flange width necessary to accommodate a rivet, in.
ϵ	ratio of free stream density to stagnation point density

θ	circumferential angle measured leeward plane, rad
λ	load factor
λ_{SF}	stability factor of safety
μ	viscosity, slug/ft-sec
ν	Poisson's ratio
ρ	density, slug/ft ³ or lb/in. ³
τ	$\rho_c/2\rho_f$

Subscripts:

B	value at base of capsule
BL	classical boundary layer result
c	pertaining to sandwich core; or critical value
e	envelope value
f	pertaining to sandwich face sheet
P	value at payload attachment
s	stagnation point value
∞	free stream value
()*	minimum gage value

FLOW FIELD ANALYSIS

The purpose of this portion of the study is to provide design pressure and convective heating rate distributions for several candidate geometric shapes for Martian entry capsules. In Reference 2, steady state flow field solutions for 120° cone and OA.833 tension shell shapes at angle of attack are obtained by a first approximation integral relations method. Although this method is adequate for the cone, it is inadequate for the tension shell, on which triple point bifurcated shocks occur. The results presented here are based on a more versatile computer program which obtains steady state solutions by solving the transient flow field equations at increasing values of time until steady state conditions are reached. The accuracy of this program is demonstrated in the Appendix, giving a comparison of flow field solutions with experiment for 120° cones at zero and 10° angle of attack.

Using this program the tension shell pressure distribution of Reference 2 was recalculated. Additional flow field solutions for both shapes at zero angle of attack were also obtained in order to determine convective heating rate distributions. In order to examine the effect of configuration variations on aerodynamic performance, zero angle of attack pressure and convective heating rate distributions were obtained for three more blunt shapes, viz. 140° cone, 60° spherical dish, and an OA.65 tension shell. In all these calculations the Martian atmosphere was assumed to be 100 percent CO_2 and real gas effects were included. Low Reynolds number effects were included in the convective heating analysis.

Pressure Loads

Analytical methods. - The primary assumption in the flow field calculation is that the shock layer fluid is inviscid. The free stream densities associated with the model Martian atmosphere are quite low and rarefied gas effects significantly influence shear stress and convective heating over large portions of the trajectory. At peak aerodynamic loading conditions, however, the majority of the shock layer is inviscid and the aerodynamic drag is due to pressure forces.

Direct steady state solutions of the blunt body inviscid flow fields were obtained with a finite difference transient flow computer program. The basic idea of the time-dependent technique, as suggested by von Neumann (Ref. 3) is to consider the unsteady flow equations and to follow the evolution of flow in time until it settles down to a steady pattern. This procedure has the advantage that the steady inviscid mixed elliptic-hyperbolic partial differential equations that describe the subsonic and transonic flow field are hyperbolic when the time terms are added. Thus, the complete flow field may be treated as an initial value problem, and the difficult multiple saddle point boundary value problem associated with higher order integral solutions and the body geometry limitations of inverse methods are avoided. In addition, the imbedded shocks associated with the triple-point flow conditions on the tension shell are calculated automatically in the transient method and shock fitting is not required.

The transient program follows the evolution in time of a specified region of the flow field using the numerical method developed by Godunov (Ref. 4). The region of integration is assumed to be bounded by the body, the detached bow shock wave, the axis of symmetry of the body, and a downstream surface across which there is no upstream influence. The body and shock wave profiles are approximated by straight line segments and the region of integration divided into a mesh of quadrilateral cells.

The initial flow field is usually specified by linear interpolation between flow variables behind an assumed shock and body values determined by a Newtonian pressure distribution. The evolution of this flow field is followed in time by integration of finite difference approximations to the Eulerian conservation laws within the flow field and application of the Rankine-Hugoniot relations for a moving shock to determine the shock boundary motion. The flow field and region of integration thus changes in time in accordance with the full equations of motion. When the flow field approaches steadiness, it satisfies the full set of steady state equations of motions. The method is described in detail in Reference 5.

The angle of attack calculation is made by an approximate solution of the unsteady three-dimensional inviscid conservation equations. As in the case of the two-dimensional program, Godunov's method is used to obtain a stable finite difference approximation to the time dependent equations of motion. The computation is carried out by performing calculations similar to those in the two-dimensional program in both the windward and leeward planes of symmetry of the flow field. A crossflow approximation couples the two computational planes. In the present simplified crossflow approximation, the flow variables are assumed to vary sinusoidally in the circumferential direction, and the program is limited to small angles of attack.

The 100 percent CO_2 , 5 mb surface pressure VM-8 model atmosphere was assumed to characterize the free stream properties. Real gas and nonequilibrium chemistry effects were included in the flow field solution. Across the bow shock, the rotational and vibrational internal energy modes were assumed to be fully equilibrated with the translational mode, while the chemical species were assumed to be frozen at the free stream concentrations, i.e., 100 percent CO_2 . The assumption of equilibrium internal degrees of freedom for CO_2 and O_2 normal shocks has been verified experimentally (References 7 and 8) and is a good assumption for these cases. At the stagnation point, the fluid was assumed to be in thermochemical equilibrium. Along the body, it was found that the characteristic flow time is much shorter than the characteristic chemical reaction time and hence, the chemistry was treated as frozen at the stagnation equilibrium species concentrations. The value of γ characterizing the shock density ratio is approximately 1.17, while the frozen chemistry isentropic exponent γ on the body at the peak dynamic pressure condition is 1.18. Thus, the isentropic exponent approximating the real gas chemistry conditions in the shock layer is nearly constant. Because of the frozen chemistry conditions in the shock layer, the pressure distributions are essentially independent of body size and thus can be scaled for similar body shapes.

The steady state flow field solutions obtained with the transient computer program have been compared with experiments and found to give almost identical results (Ref. 5). A comparison of theory with 120° cone experiments (Ref. 6) at zero and finite angle of attack is presented in the Appendix.

Results. - The zero angle of attack body pressure distribution and shock layer properties were calculated for peak dynamic pressure conditions for blunt 120° and 140° cones, OA.65 and OA.833 blunt tension shell configurations, and a 60° spherical dish. The free stream and stagnation point properties used in these calculations are shown in Table I. These correspond to orbit mode entry with a ballistic coefficient of 0.32 slug/ft^2 . Additionally, an angle of attack calculation was made for the OA.833 blunt tension shell.

120° sphere-cone: The shock shape and body pressure distribution for the 120° cone are shown in Figure 1. The bow shock is concentric with the body in the region of the nose and the flow field is locally subsonic. The sonic line position is very similar to the hemispherical blunt body case and extends from bow shock to the body in the region of the sphere-cone junction. The sonic line does not actually touch the body, but runs from the sphere-cone junction to the base roughly parallel to the cone surface at a distance approximately 5 percent of the standoff distance. The flow in the conical portion of the shock layer is almost entirely supersonic. The slight concavity in the bow shock just aft of sphere-cone junction is produced by the reflection of compression waves emanating from the sphere-cone region.

In Figure 1, the cone pressure as a function of the ratio of local body radius to base radius is also shown. The two prominent features of the pressure distribution are the rapid decrease in pressure recovery at the sphere-cone junction and the pressure plateau in the conical region. The pressure distribution in the nose region is similar to a hemispherical shock layer result and the pressure plateau in the conical region is similar to a pointed cone supersonic flow result. It is seen that the Newtonian flow model, which is a low γ limit of the hypersonic inviscid flow field equations, provides a useful approximation in the nose region pressure distribution but is in error in the conical region. The drag coefficient obtained from the pressure distribution on the 120° sphere-cone is 1.47.

OA.833 tension shell: The OA.833 tension shell inviscid shock shape and surface pressure distribution are shown in Figure 2. In the nose region, the flow is subsonic and the shocklayer is similar to that of a hemispherical body. Aft of the junction of the spherical cap and tension shell, the shock layer flow is supersonic except for a narrow region of high entropy subsonic flow adjacent to the body surface. The shock layer flow decelerates in this region because of the concave shape of the body. Approximately two-thirds of the way along the body, a shock triple point occurs and the flow in the shock layer aft of this point is all subsonic until a flow expansion occurs at the base corner. Note that the sonic line is continuous, since it starts at the bow shock, connects with the triple-point imbedded shock, and returns to the bow shock. The corner sonic line is continuous also, but a base region and wake neck calculation would be required to show the sonic line position.

The triple-point shock and slipline flow configuration is calculated automatically by the transient finite difference method. The embedded shock and slipline are smeared over three or four cells, and a finer grid size than was used is required to obtain near discontinuous shock and slipline properties. If such detail is required at a later date, the flow in this region should be recalculated with a finer grid size.

The surface pressure distribution is similar to Newtonian in the nose region. The supersonic flow decelerates along the tension shell and a large positive pressure gradient results. The flow aft of the triple point is all subsonic, and the pressure level is constant and higher than at the stagnation point. This phenomena of high pressure recovery in the base region has been observed experimentally for less blunt tension shells tested in air (Ref. 9). The high pressure recovery results from the fact that the stagnation pressure of the supersonic shock layer is characterized by an oblique shock entropy and, hence, this stagnation pressure is considerably larger than the normal shock value.

The assumption that the flow over the tension shell is inviscid during Martian entry may not be valid. The combination of the low Reynolds numbers associated with the Martian entries and the large positive pressure exhibited in the tension shell inviscid flow field result makes it highly probable that a viscous separated shock layer flow would exist on the tension shell during a large portion of entry trajectory. The inviscid calculation is useful, however, since it represents an upper bound on the magnitude of the body pressures. It would be useful to make an accurate low Reynolds number viscous calculation, but presently it is not possible. The effect of viscous flow separation would be to make the majority of the shock layer subsonic, hence, smoothing out the pressure gradients. The resulting drag coefficient would be significantly lower than the 1.78 value obtained from the inviscid flow field calculation.

OA.833 tension shell at angle of attack: In Reference 2, an attempt was made to calculate the pressure loading for the tension shell at 12° angle of attack. This calculation was made for the peak dynamic pressure conditions associated with a critical failure tumbling mode trajectory in the VM-8 model atmosphere. These conditions are shown in Table II. A computer program based on the method of integral relations was used to make the calculation. Although the results obtained in the windward plane are reasonable, it was found that a triple point existed in the leeward plane and it was not possible to calculate or make an accurate estimate of the leeward flow without a more accurate computer program. Therefore, the transient flow finite difference computer program, which calculates triple points and embedded shocks automatically, was used to recalculate the angle of attack flow field. The shock configuration and the pressure distribution obtained are shown in Figure 3. In the windward plane, the shock and pressure distribution in the nose region are similar to a hemispherical body result. The flow is transonic in the spherical cap tension shell junction region, and a weak triple point at the bow shock is noted. Aft of the junction, the flow in the windward plane is subsonic and the pressure distribution is at a constant level, approximately equal to the stagnation point pressure.

In the leeward plane, the shock layer flow becomes sonic just prior to the spherical cap tension shell junction. The shock layer flow is accelerated to supersonic velocities and then is compressed in the initial concave region of the tension shell. A gradual pressure rise occurs up to the triple point. A shock emanating from the triple point produces an abrupt increase in pressure. Aft of the triple point, the shock layer flow is subsonic and a pressure peak of 1.72 times the stagnation point pressure is predicted. In the corner region, the shock layer flow accelerates and an abrupt decrease in pressure occurs.

The axial force coefficient C_A for the OA.833 tension shell at angle of attack was calculated to be 1.80. The large positive pressure gradients found in the leeward plane suggest, that for the Martian entries, the flow may separate in leeward plane. Separation would eliminate the positive pressure gradients predicted by the inviscid flow model and would also significantly reduce the drag. However, the inviscid calculation provides an upper bound on the magnitude of the surface pressure that may exist during the highest Reynolds number phase of the trajectory. A low Reynolds number angle of attack shock layer calculation is beyond the present state of the art and is not possible at this time.

OA.65 tension shell: The OA.65 tension shell shock shape and surface pressure distribution is shown in Figure 4. The flow field is qualitatively similar to the OA.833 tension shell result and the same general descriptive discussion is applicable. The main difference between the two tension shell configurations is that the OA.65 is more blunt than the OA.833. As a result, the triple point and the high pressure region in the OA.833 case are positioned further aft and cover a smaller area than the OA.65 configuration. The OA.65 pressure level in the aft region of the tension shell is slightly lower than the OA.833 case, but the increased area over which the pressure acts, more than compensates, resulting in a higher drag coefficient ($C_D = 1.86$).

It is noted that the numerical grid space used in the OA.65 calculation is considerably larger than that in the OA.833 calculation. As a result, it was not possible to plot the sonic line associated with the thin high entropy layer near the body.

140° sphere-cone: The bow shock and the body pressure distribution for the 140° cone are shown in Figure 5. In contrast to the 120° cone case, the shock layer is completely subsonic and the sonic line is located in the base region. The pressure level on the body is considerably higher than the 120° cone case as is the drag coefficient ($C_D = 1.70$).

Spherical dish: The bow shock and surface pressure for the spherical dish are shown in Figure 6. The bow shock is nearly concentric with the body except in the region of the corner. At the corner position, the sonic line extends in a normal direction from the body and curves upstream to the bow shock.

For comparative purposes, the Newton-Busemann and modified Newtonian pressure distributions are also included in Figure 6. The Newton-Busemann model is a better approximation of the spherical dish pressure distribution than the modified Newtonian result. Both of these approximate models are in error, however, in the region of the corner where a local acceleration of the flow occurs.

Convective Heating Rate Distributions

The convective heating rate distributions at the free stream conditions corresponding to peak dynamic pressure (see Table I) have been determined for the 120° and 140° sphere-cone, the OA.65 and OA.833 tension shell, and the spherical dish capsule configurations.

Analytical methods. - The convective heat transfer calculations are complicated by the effects of low Reynolds numbers, significant quantities of CO₂ in the boundary layer, and dissociation of the boundary layer gases. A survey of applicable theoretical and experimental low Reynolds number shock layer studies indicates a wide variation in the method of solution, the gas models, and the assumed free stream conditions with a corresponding larger variation in the predicted magnitude of "rarefied regime effects". At present one of the most general and yet definitive studies of rarefied gas regimes is that given by Goldberg (Ref. 10). In this study, nonsimilar hypersonic continuum flow field spherical cap solutions were obtained for a flow model which is applicable through the incipient merged layer regime (Ref. 11). An examination of the results of References 10 and 12 indicates that for the shock layer Reynolds numbers of interest in this study, viscous and conduction effects due to velocity and temperature gradients at the shock and in the inviscid shock layer can be neglected.

Thus, Rankine-Hugoniot shock relations and inviscid shock layer equations can be used to calculate the flow field. It also is assumed that the vehicle wall is cold; thus, the boundary layer displacement thickness is small, and the inviscid shock shape and body pressure distribution are not affected appreciably by the boundary layer.

For the flight conditions associated with Martian entries, the low Reynolds number results of Reference 10 predict greater convective heat transfer rates than are obtained from the classical discontinuous shock, inviscid shock layer, thin boundary layer theory. This increase in heat transfer is primarily due to the shock layer vorticity induced by the curved bow shock. The effect of vorticity can be incorporated in conventional boundary layer theory, however, as long as the proper boundary layer edge velocity conditions are used (Ref. 12).

In the region of the stagnation point the vorticity interaction effects have been calculated by using the method presented in Reference 12 and by utilizing the low Reynolds number spherical cap solutions given in Reference 10. The method of Reference 12 yields a solution of the boundary layer equations in which the slope of the boundary layer velocity profile is matched with the slope of the inviscid velocity profile for equal mass flow rates. The input parameters required to obtain a solution are the

stagnation-point Reynolds number $Re_s = \left[\rho_s R_N \partial \bar{u} / \partial (s/R_N) \right] / \mu_s$, and the normal velocity gradient $\partial(\bar{u}/v_\infty) / \partial(z/R_N)$. These parameters are given by the inviscid flow field solution. It was found that this method and that of Reference 10 both give essentially the same results, but that some care must be taken when using the latter results. The low Reynolds number results of Reference 10 are presented as a ratio of the low Reynolds number heating to the classical boundary layer heating and are correlated in terms of shock density ratio and Reynolds number. The results of the correlation are shown in Figure 7. The classical boundary layer solution used to make the low Reynolds number heat transfer results nondimensional is based on modified Newtonian boundary layer edge properties. High density ratio (ρ_s/ρ_∞) inviscid shock layer property results can differ considerably from modified Newtonian results. Thus, the deviation of the low Reynolds number heat transfer from the so-called classical boundary layer result given in Figure 7 includes not only low Reynolds number effects, but also inviscid property effects.

In addition to low Reynolds number effects, the effect of significant concentrations of CO_2 in the ambient gas must be considered in the convective heat transfer calculations. Numerous theoretical and experimental studies of stagnation point convective heat transfer in N_2 - CO_2 gas mixtures of interest in planetary entry have been made. The general result is that convective heat transfer increases as the percentage of CO_2 is increased. Predictions of the magnitude of the increase vary considerably, however. In this study, the results of Hoshizaki (Ref. 13) have been used to account for ambient CO_2 gas composition. Hoshizaki's results indicate that a pure CO_2 environment increases the convective heating approximately 10 percent over an equivalent air case. The theory of Scala and Gilbert (Ref. 14) which was used in Reference 2 predicts a 35 percent increase in convective heat transfer for 100 percent CO_2 atmosphere, but there is no experimental data to substantiate this large increase.

The correlation results of Hoshizaki have also been utilized to include the effects of dissociation on the stagnation point convective heat transfer. The theory is applicable to either frozen or equilibrium chemistry boundary layers for the velocity range of interest in this study, and the results are correlated in terms of shock properties and the inviscid flow stagnation point velocity gradient. The results correlate closely to the mid-range of existing experimental data. The blunt body wall has been assumed to be perfectly catalytic, and for the flight velocities of interest in this study, the convective heat transfer is insensitive to the degree of nonequilibrium in the dissociated boundary layer (Ref. 15). The correlation formula in terms of stagnation point velocity gradient is

$$q_s (\text{Btu}/\text{ft}^2 \text{sec}) = 2.81 \left[d(\bar{u}/v_\infty) / d(s/R_N) \right]_s \cdot^5 (p_s/R_N) \cdot^5 (v_\infty/10^4)^{2.19}$$

In this correlation, the stagnation-point pressure, p_s , and nose radius, R_N , have units of lb/ft^2 and ft respectively, and the free stream velocity, V_∞ is measured in ft/sec .

The heat transfer distribution around the body can be calculated by conventional boundary layer theory, as long as the appropriate boundary layer edge conditions are used (Ref. 12). For the flight conditions given in this study, the shock layer Reynolds number based on the nose cap radius is approximately 80,000. At Reynolds numbers in this range, the boundary layer thickness in the nose region is approximately 4 percent of the shock layer thickness. Since the boundary layer is a significant percentage of the shock layer thickness, the proper boundary layer edge conditions differ considerably from those given by inviscid flow body properties. The magnitude of the velocity at the edge of the boundary layer is increased due to the shock curvature induced vorticity and can produce a significant increase in the convective heat transfer. The viscous and conduction effects due to velocity and temperature gradients in the shock layer, however, have a small effect on convective heat transfer at the wall and can be neglected. It should also be noted that the vehicle wall has been assumed to be cold, and the boundary layer displacement thickness and its interaction with the inviscid flow field is negligible.

The laminar heat transfer distributions have been calculated by Lees' local similarity solution (Ref. 16). The Lees' method gives the ratio of the local heat transfer at a body station to the stagnation point value as a function of the local density-viscosity product and velocity at the edge of the boundary layer. For the shock layer Reynolds numbers associated with the major portion of the Martian entry convective heat pulse, the spherical body results of Cheng (Ref. 17) and Ferri (Ref. 12) indicate that the effect of vorticity on the laminar heat transfer distribution is approximately constant over the entire sphere cap. Thus, the inviscid body properties on the spherical cap can be used in the method of Lees, and the vorticity correction is obtained implicitly when the nondimensional heat transfer distribution is multiplied by the low Reynolds number stagnation point heat transfer result.

Lees' analysis is also used to calculate the heat transfer distribution aft of the spherical cap, but the inviscid properties at the edge of the boundary layer, rather than the vehicle wall, are used in the calculation. For the 120° sphere-cone and the tension shell cases, the edge of the boundary layer properties aft of the spherical cap differ considerably from the inviscid body properties since the boundary layer edge extends a significant distance into the shock layer.

Ideally, the boundary layer edge properties could be obtained by coupling the boundary layer solution of Reference 12 with the detailed inviscid flow field results obtained in this study. Such a calculation requires considerable formulation and computer programming, however, and a simplified method that is estimated to deviate less than 5 percent from the more exact analysis has been used. The boundary layer thickness over the entire body surface is assumed to be the same percentage of the shock layer thickness as on the nose cap, namely 4 percent.

A momentum Reynolds number of 250 is used for a criteria of transition to turbulent flow. Turbulent flow heat rates are calculated by the method of Rose, Probstein and Adams (Ref. 18). No correction for gas composition effects is included and it is assumed that the basic air correlation is applicable to the given Martian atmospheric composition.

Results. - The results of the convective heat transfer analysis are given in Figures 8 and 9. These calculations were made assuming the free stream conditions and correspond to the peak dynamic pressure trajectory point given in Table I. This trajectory point is in the latter portion of the convective heat pulse and the shock layer Reynolds number is considerably higher than it is at peak laminar heating. Low Reynolds number effects in the stagnation point region were found to be negligible. It should be noted, however, that low Reynolds number effects at the peak convective heating trajectory point will increase the stagnation point heating above the classical boundary layer result by approximately 10 percent. The increase will be even larger for earlier portions of the entry trajectory.

The laminar boundary layer thickness, as calculated by the method of Reference 12, was found to be approximately 4 percent of the shock layer thickness. The boundary layer thickness, although small, entrains the majority of the entropy layer originating in the normal bow shock region. Thus, the inviscid streamline at the edge of the boundary layer emanates from an oblique shock. In regions of supersonic shock layer flow, the boundary layer edge velocity is significantly larger than the inviscid body result, which implicitly contains the normal shock entropy condition, and, hence, the laminar convective heating is also larger.

For the given trajectory point, the momentum Reynolds number transition criteria of 250 ($\rho_{\infty} V_{\infty} R_N / \mu_s \approx 400,000$) was exceeded on each vehicle. Since the criteria for transition is uncertain for these blunt vehicles, both the laminar and turbulent heat transfer distributions are shown. The laminar distribution will be applicable for the cones and the spherical dish over the major portion of the heat pulse. Low Reynolds number effects, which occur predominantly in subsonic flow regions, must be included at higher altitudes, however.

In the case of the tension shell vehicles, the transition Reynolds number occurred in the vicinity of the triple point. The convective heating distributions shown in Figure 9 are assumed to be representative of the entire trajectory. It is assumed that pressure pulse created by the viscous interaction of the triple-point imbedded shock and the boundary layer produces transition at all higher altitudes. Since a turbulent boundary is probably required to assure an attached inviscid shock layer in the triple-point region, the assumption of a turbulent boundary layer in the regions of large positive gradient is consistent with inviscid flow solution presented previously.

120° and 140° sphere-cones and the spherical dish: The convective heat flux versus distance along the body for the 120° and 140° sphere-cones and the spherical dish is shown in Figure 8. One of the major points to be noted is that the 140° sphere-cone laminar convective heat flux is considerably lower

than the 120° cone result. Although the nose radius of both cone configurations is the same, the 140° cone stagnation-point velocity gradient is considerably smaller than the 120° cone result. The spherical dish laminar heat transfer flux is lower than both cones and approaches the 140° cone result in the aft region of the body surface.

OA.65 and OA.833 tension shells: The OA.65 and OA.833 tension shell convective heat transfer distributions are shown in Figure 9. The OA.65 stagnation point heating is slightly larger than the OA.833 result because the OA.65 nose radius is slightly smaller. The extent of the turbulent heating is larger on the OA.65 than the OA.833 because the shock layer triple point and, hence, transition occurs earlier on the blunter OA.655 configuration.

AEROSHELL STRUCTURAL SYNTHESIS

Analytical Methods

In order to design efficient entry capsules it is necessary to develop a systematic weight optimization procedure. Even with the best analytical tools, a trial and error optimization approach has little chance of success because of the great number of structural variables present.

Design-analysis iteration procedure.- A practical design optimization procedure was developed for sandwich and ring-stiffened capsules. In this procedure, the design of the aeroshell is coupled iteratively with an elastic stability analysis of the design. Thus, structural weight is minimized with respect to buckling failure of the capsule, as opposed to a stress failure. This is in accordance with the fact that, in general, for lightly loaded entry capsules the critical mode of failure is buckling.

The iteration procedure is illustrated schematically in Figure 10. In this chart, dashed arrows represent return paths of iteration loops. Boxes bordered with heavy lines represent steps using computer programs. The group of boxes lying within the broken dot-dash border represents the design of the shell interior (i.e., exclusive of the payload and base ring). As shown, this group applies only to ring-stiffened construction.* For sandwich cones it is replaced by a manual design step. The shell design step for both constructions is discussed further below.

* As discussed later, steps indicated by boxes labeled C and D were performed only in the design of the tension shell capsules.

In order to keep the size of the task within reason, it was necessary to limit the number of basic variables considered. Hence, only one base diameter and two ballistic coefficients were considered. Also, for each structural temperature, consideration was, for the most part, limited to two basic structural materials, aluminum and titanium. The properties assumed for these materials are given below.

	E (10 ⁶ psi)		ν	ρ (lb/in. ³)
	300 ^o F	550 ^o F		
Al	9.35	6.1	.32	.100
Ti	16.5	15.5	.32	.158

On the other hand, the aeroshell weight correlations, derived in part from the designs obtained, allow the evaluation of the effect on aeroshell weight of other materials, as well as variations in base diameter and dynamic pressure (cf. p.29).

Aeroshell loads.- Pressure distributions for both windward and leeward meridians were provided by the flow field analyses discussed earlier. These distributions are conservatively based on peak dynamic pressure conditions associated with an uncontrolled tumbling entry into a VM-8 model atmosphere from a Martian orbit. As shown in Reference 2, the angle of attack amplitudes at peak dynamic pressure are 9° and 12° for the 120° cone and OA.833 tension shell, respectively. The aeroshell pressure distributions are therefore based on these values of angle of attack.

For the purposes of design an axisymmetric pressure loading with meridionally varying magnitude, locally equal to the maximum of the windward and leeward pressures, was used. Finalized designs were then subjected to stress analysis based on the assumption that at peak loading the circumferential distribution of pressure contains only axisymmetric and first harmonic components. In all cases, the pressure distributions were equilibrated by the distributed inertial loads of the capsule. For this purpose, the total mass of each capsule was computed from its design ballistic coefficient and its drag coefficient. The difference between the total mass and the mass of the shell structure, base ring, and heat shield was assigned to the payload and assumed to be concentrated in the payload ring.

It should be noted that the pressure distributions used are based on entry conditions associated with values of ballistic coefficient below 0.32 slug/ft². In using these distributions it is assumed that their shapes are insensitive to ballistic coefficient variation, but that their magnitudes vary proportionally with ballistic coefficient. In the following discussion, the term "design load" (or "design pressure") refers to the above-mentioned axisymmetric pressure distribution (so modified for ballistic

coefficient) times the buckling factor of safety. In all cases, the desired buckling factor of safety is $\lambda_{SF} = 2.25$. In order to limit the number of design iterations, variations of ± 0.25 from this value were considered acceptable.

The effect of thermal loads on structural stability and stress was neglected. However, as noted previously, the temperature dependence of material properties is accounted for.

Conical capsules: The pressure distribution used for the conical capsules was taken from Reference 2 and is reproduced here in Figure 11. This distribution is based on a ballistic coefficient of 0.2 slug/ft^2 , and therefore the equivalent pressures for 0.32 and 0.64 slug/ft^2 capsules are larger by the factors 1.6 and 3.2 , respectively. C_D was taken to be 1.51 , which as shown in Figure 51 of Reference 2 agrees well with experiment.

Tension shell capsules: The pressure distribution presented in Figure 3 was used for the tension shell capsules. In this case the pressure is presented in units of the stagnation pressure, given as 1.83 psi in Table II. However, this value is based on a ballistic coefficient of 0.182 slug/ft^2 . Therefore the equivalent stagnation pressures for the 0.32 and 0.64 slug/ft^2 capsules are taken to be larger by the factors 1.76 and 3.52 , respectively.

Base ring and payload ring design.— Previous studies (Refs. 19 and 20) have shown that the function of edge rings for shells of revolution is to suppress inextensional buckling, for which $N = 2$ is the critical harmonic. The following additional results, demonstrated in Reference 20 for blunt conical shells, have been found, during the course of this study, to be valid for more general shells of revolution. (Cf. Ref. 21.) There exists a critical harmonic $N_C > 2$ for which the critical load attains a relative minimum. In this buckling mode there is relatively little deformation at the shell edges. Therefore, the corresponding critical load is insensitive to the stiffness of edge rings. On the other hand, for edge rings of insufficient stiffness the critical load attains an absolute minimum for $N = 2$, this mode being essentially inextensional.

Let us now restrict our attention to blunt truncated aeroshells, for which a payload ring is attached at the small end and a base ring is attached at the large end. Then, in the $N = 2$ mode of buckling large buckling deformations occur at the base ring. Therefore, the corresponding critical load is directly related to the base ring stiffness. In fact, for tubular base rings, which were assumed for this study, this critical load is approximately proportional to the flexural rigidity of the base ring. Its extensional rigidity has little effect since there is negligible extension in this buckling mode.

In contrast to this, for practical payload rings, the payload ring stiffness has negligible effect on the buckling load. Since, typically, this ring is in a state of hoop tension, its design is based primarily

on stress and fabrication considerations. Additionally, the payload ring designs presented include consideration of local wall instability due to the axial inertia of the payload mass. As the payload stiffness affects the stresses in the vicinity of the payload ring, it is apparent that the payload ring design cannot be finalized until the payload is defined. However, being at a small radius, the payload ring makes a relatively minor contribution to capsule structural weight.

In light of these results, one can visualize the buckling response as the flexural rigidity (EI) of the base ring is varied. For low EI , the shell buckles at low load into the $N = 2$ mode. As EI is increased, the mode shape remains essentially unaltered, but the buckling load increases in the same proportion until the critical load for the $N = 2$ mode equals the critical load for the $N = N_c$ mode. Further increases in EI are ineffectual since henceforth the shell buckles in the $N = N_c$ mode, which is unaffected by the base ring. This behavior suggests that the base ring flexural rigidity should be chosen so that the critical loads corresponding to $N = 2$ and $N = N_c$ are equal. As indicated by Box F of Figure 10, this criterion is incorporated into the optimum design procedure.

In order to achieve a minimum weight tube it is desirable to have as large a ratio of tube radius to thickness as possible. This ratio is limited by either

- 1) local instability of the tube wall (for moderately load rings),
- 2) local distortion of the tube cross section at the shell interface (for lightly loaded rings), or
- 3) minimum gage.

Initially, the tube R/t was determined so that at the design load the tube becomes locally unstable. For this calculation, the maximum combined hoop compressive stress in the tube was assumed to be uniformly distributed, and the axial stress buckling criterion for moderately long cylindrical shells of Reference 22 was applied. However, if this computed value is too large, one can expect that the tube will cease to behave in accordance with ring theory, which treats the cross section as a rigid element. If this occurs, the ring flexural rigidity required to suppress the $N = 2$ buckling mode will not be achieved. In order to avoid this possibility, a limit of $R/t = 125$ was imposed. An additional constraint on R/t is provided by the requirement of minimum gage for the tube wall, taken to be 0.032 in., and the required moment of inertia I of the tube section.

Shell design.- As was demonstrated in Reference 2, the payload ring essentially decouples the portion of the aeroshell aft of the payload

ring from the nose section forward of this ring. The nose section, being at a smaller radius, is generally much stiffer than the aft portion of the aeroshell. Furthermore, in practice, part of the payload itself may be in contact with the forward section, giving it added but unknown stiffness. For these reasons, and also because it contributes a relatively small amount of weight to the capsule, the design-analysis procedure was applied only to the truncated aeroshell excluding the nose section. After an optimized design was obtained, the extra mass of the nose section was estimated by assuming it to have the same average surface density as the aft aeroshell. Henceforth, the term "aeroshell" shall refer to the truncated aeroshell exclusive of the nose section.

As noted earlier, the payload and base ring have negligible effect on the critical load of the aeroshell for $N = N_c > 2$. On the other hand, for a given shell structure, the $N = 2$ critical load is effectively controlled by the base ring. These facts allow the decoupling of the design of the aeroshell, excluding the end rings, from the design of the rings themselves. The procedure then is to design the shell interior so that its critical load for $N = N_c$ is the design load. After this design is achieved, the base ring is designed in accordance with the principles stated earlier.

Sandwich cone: The design step for the sandwich cone consists of a determination of the core depth t_c and face sheet thickness t_f of a symmetrical sandwich wall. The following two conditions, the second of which may be overridden by the minimum gage constraint $t_f \geq 0.016$ in., are imposed on these variables:

- 1) Critical pressure level for general instability equals the design pressure, and
- 2) Equal weights of material in core and face sheets.

Condition (1) is based on a general instability correlation obtained for a combined loading of a uniform hydrostatic pressure and an axial tension equal to the resultant of the hydrostatic pressure acting on the capsule base. For this correlation, the following linear interaction formula, based on the results of Reference 23, was used.

$$p/p_o - .625 P/P_o = 1 \quad (1)$$

Substitution of the critical hydrostatic pressure and critical axial load for a sandwich cone, viz.

$$p_o = 4.2 E t_f t_c^{1.5} / L \bar{R}_2^{1.5}$$

$$P_o = 13.2 E t_f t_c \cos^2 \alpha$$

and the relation $P = \pi r_B^2 p$ into Eq. (1) gives the result

$$p = (4.2 E/L\bar{R}_2^{1.5}) t_f t_c^{1.5} / (1 - \kappa t_c^{.5}) \quad (2)$$

where

$$\kappa = .625 r_B^2 / L\bar{R}_2^{1.5} \cos^2 \alpha$$

For the specified cone geometry, $\kappa = 0.195$ for dimensions in inches.

For the purpose of treating the variable pressure loading, Eq. (2) was modified to

$$\lambda = CE t_f t_c^{1.5} / (1 - .195 t_c^{.5}) \quad (3)$$

Here, λ is simply a design load factor which multiplies the pressure distribution.

Condition (2) is based on a slight modification of an elementary minimization of the shell surface density, $2t_f \rho_f + t_c \rho_c$, subject to the buckling constraint for hydrostatic pressure, $t_f t_c^{1.5} = \text{constant}$. This results in an optimum core weight to face sheet weight ratio of 1.5. Condition (2) is a more practical design condition in that it results in thicker face sheets, lower stresses and in designs that are less affected by transverse shear deformations. The theoretical weight penalty incurred by using Condition (2) is only 2%.

By assuming a core density of 0.003 lb/in.³ (only aluminum cores were considered), for a given face sheet material the ratio ρ_c / ρ_f is known. Thus, Condition (2) translates into a known ratio, say τ , of face sheet thickness to core depth. Then Eq. (3) may be rearranged to the form

$$t_c = (\lambda / CE\tau)^{.4} (1 - .195 t_c^{.5})^{.4} \quad (4)$$

For a given correlation factor C (estimated initially from the results of Reference 2), Eq. (4) was solved numerically for t_c , and hence t_f . If, however, t_f turned out to be less than 0.016 in., then t_f was set equal to 0.016 in. and t_c recomputed from Eq. (3).

Ring-stiffened cone: Whereas the design step for the interior aero-shell for the sandwich cone is relatively simple and performed manually, the corresponding step for the ring-stiffened monocoque cone is sufficiently complex to require development of a new computer program. This program is represented by the box labeled A in Figure 10. Details of the method underlying this program are presented in Reference 24. In this section the essential features of this program are discussed so that the reader can understand what it accomplishes.

The design variables considered by the program are:

- 1) Shell wall thickness (assumed uniform),
- 2) Ring locations,
- 3) Ring cross-sectional lengths (assuming uniform thickness Z-section interior rings with a nominal web-to-flange width ratio of 2.5*), and
- 4) Ring cross-sectional thicknesses.

Thus a total of $3M + 1$ variables are considered where M is the number of rings required. The following conditions are imposed on these variables:

- 1) Critical pressure for general instability equals the design pressure,
- 2) Critical pressure for instability of shell bays between rings equals design pressure,
- 3) Critical pressure for local instability of each interior ring equals design pressure, and
- 4) Relative increase (due to stiffening) in the local hoop flexural rigidity of the composite shell wall is proportional to the normal deflection of the general instability mode.

Conditions(1) through (3) represent for this problem the usual optimum design condition of simultaneous occurrence of failure modes. Condition (1) is based on a slightly modified form of the general instability correlation for ring-stiffened conical shells presented in Reference 26. Condition (4) represents a new design approach and is motivated by the desire to place the ring material where it will do the most good.

In addition to these conditions, in order to ensure fabrication feasibility, the following manufacturing constraints are built into the program:

- 1) Minimum shell gage,
- 2) Minimum ring gage,
- 3) Minimum rivet diameter, and
- 4) Riveted ring flange constraints, $4d_r \leq f_R \leq d/2$.

In practice, the design program obtains successively optimized ring size and spacing distributions for several shell thicknesses. The initial shell thickness and a thickness increment are input quantities, along with shell geometrical data, shell and ring material properties, pressure level,

* This is very nearly the optimum ratio for local stability of a ring (cf. Reference 25).

minimum ring gage, minimum rivet diameter, general instability correlation factor, and an estimate of the normal deflection function of the general instability mode. For each shell thickness the total structural weight, including shell skin, interior rings, and an estimate for rivet weight, is computed. The process is terminated after the total structural weight attains a relative minimum with respect to shell thickness.

Ring and stringer-stiffened tension shell: The design step for the tension shell necessitated the generalization of the cone program to more general shells of revolution. As a result of new problems encountered in the design of the tension shells, several features, in addition to the treatment of a more general shape, were added to the program, as well as to the iteration procedure itself. The improvements in the procedure are represented by boxes C and D of Figure 10. These relate to a more precise method for achieving local stability for all rings and bays, and are discussed further below.

As was shown in Reference 2, rings alone are not sufficient to stiffen a tension shell capsule. Stringers are required to suppress excessive prebuckling deformations in the base region. Since such stringers typically respond to entry loads by developing longitudinal tension, they have no local stability problems. For this reason, and also because a relatively small weight of stringers suffices, stringer properties are not optimized but rather treated as known data by the design program.

The design pressure distribution on the conical aeroshell is reasonably flat and was treated as constant in the design step. In contrast, the tension shell pressure distribution (cf. Figure 3), although relatively flat in the forward region, has rapid variation in the base region, where a pressure spike occurs on the leeward meridian. It was found that basing the design on a mean pressure, as was done for the cones, results in a local instability problem in the region of the pressure spike. In order not to incur a significant structural weight penalty, the variable design pressure distribution was used in the design step for the tension shell capsules.

Since no general instability correlation has as yet been developed for tension shells, as an expedient, the correlation used for cones, with suitable definitions for average radius of curvature and average pressure, was employed (see Reference 24 for additional details). It is emphasized that the correlation so obtained cannot account properly for the double curvature of the tension shell and, furthermore, includes no effect of stringers. However, as shown in Figure 10, each design obtained is analyzed for general instability, and the correlation factor is changed until agreement is reached between design and analysis critical loads.

As in the cone program, the local shell meridional and hoop forces, as well as the ring hoop forces, are determined from membrane theory. However, in this case, the effect of meridional curvature, stringers, and variable pressure are included. In the membrane analysis, normal force equilibrium is written on a finite shell element (of width d) centered at a ring. It is assumed that variables in the membrane equations apply at the center of the

element, i.e., at the ring. Variables required (shell geometry, pressure, and ring and stringer properties) for the bay buckling criterion are taken as mean values over the bay. These assumptions are valid only if these variables are slowly varying over each bay. Otherwise, a design will be obtained which may be locally unstable in certain regions. If this occurs, a fictitious pressure distribution with the pressure locally increased in the unstable regions (and possibly decreased in regions with a large stability margin) is input to the design program in the next design step.

Shell analysis.- The shell design procedures, discussed in the preceding sections, are based on certain approximations, which require verification and, if necessary, modification by more precise analytical methods. With regard to the sandwich cones, this involves a straightforward calculation of the prebuckling state and corresponding critical load, as shown in the boxes labeled B and E in Figure 10. The methods of the computer programs represented by boxes B, E, and F have been presented in References 27 and 28.

In contrast, for ring-stiffened designs, because of the relatively large number of rings required and limited computer core space available, it was convenient to analyze modified designs, rather than the actual designs obtained. This modification consists of the replacement of the actual discrete ring distribution by a modified discrete ring distribution at a set of modified ring locations. The set of modified ring locations is sufficiently dense so that, insofar as the actual design has sufficiently many rings to be analyzed on a "smeared-out" ring stiffness basis, with respect to general instability the modified design and the actual design are equivalent.

On the other hand, with respect to bay and local ring instability, the modified design clearly does not model the actual design. Therefore, to check these modes of buckling, it was necessary to employ an additional program represented by box C in Figure 10.* This program uses as input the prebuckling stress resultants computed for the modified design (in step B of Figure 10), and is based on the assumption that the total circumferential (including rings) and meridional (including stringers) stress resultants are approximately the same for both modified and actual designs. Employing strain compatibility between shell, rings, and stringers (neglecting their eccentricities), it computes the shell and ring stress resultants at the design load. These are compared to buckling allowables for all shell bays and interior rings.

Initially, for the cone designs, the prebuckling state was computed according to nonlinear moderate rotation theory using a fourth computer program which extends the axisymmetric solution of Reference 27 by means of Newton's method. However, it was found that the nonlinear effect is unimportant for the 120° cones, and so the cone designs were carried

* As noted previously, this step was performed only for the tension shell capsules, for which the approximations of the design program lose accuracy.

out using linearized prebuckling states. On the other hand, the analysis of tension shell designs is based exclusively on nonlinear prebuckling states (although with the full-length stringers used, this may also be unnecessary).

Heatshield weights.- Heatshield weights were determined using data supplied by NASA for the superlight (14.7 lb/ft³) ablator, SLA 561 (Reference 29). This data is based on an entry trajectory in a VM-7 Mars model atmosphere with an entry velocity of 16 000 fps and an entry angle of -14°. Additionally, this data accounts for capsule bluntness ratio, ballistic coefficient, and heat capacity of the primary structure. The data was prepared using a computer program (Reference 30) which calculates the temperature distribution through the ablator thickness as a function of time. By trial and error the heatshield thickness was found which yields a backface temperature equal to the design value at 25 sec after the occurrence of maximum dynamic pressure.*

The heat transfer distributions used with this data are presented in Figures 8 and 9 for the cone and tension shell capsules, respectively. In accordance with the related discussion, the laminar distributions are assumed for the cones, whereas for the tension shells it is assumed that transition to turbulent flow occurs as indicated in Figure 9.

Since the calculation of the heat shield thickness distribution requires an estimate of the heat capacity of the primary structure, it can be done only after a structural design is obtained. As implied in Figure 10, the mass and stiffness effect of a crudely estimated heat shield layer was included in the structural analysis. After a finalized design was obtained, the heat shield weights were then recomputed.

Results

Point designs.- In this section, essential features of the designs obtained are presented. Prebuckling, buckling, and stress response characteristics are presented for only the lightest cone and tension shell designs for each ballistic coefficient. These represent typical responses for each configuration, and the remaining designs have essentially similar response characteristics. All of the point designs have a 19 foot base diameter. All cone designs have a payload attachment

* After the occurrence of maximum dynamic pressure, the structural temperature continues to rise. In order to decouple heatshield design from primary structure design, as a compromise, the structural temperature used with the maximum dynamic pressure loads is that attained 25 sec later.

radius of 34.2 in. and a bluntness ratio (R_N/r_B) of 0.25. The tension shell designs have a payload attachment radius of 31.2 in. and a bluntness ratio of 0.42.

The base rings for the sandwich cones are moderately loaded relative to those for the ring-stiffened cones, which are lightly loaded, and to those for the tension shells, which are heavily loaded. Thus, whereas all of the tension shell base rings and none of the ring-stiffened cone base rings are local stability critical, one of the sandwich cone base rings (0.64 slug/ft², 300°F) is stability critical. Typically, for these designs the local stresses in the vicinity of the payload ring are high. Since the payload interface is as yet undefined, the local modifications required to reduce these stresses to allowable levels were not determined, and no allowance for this is included in the structural weights presented.

Sandwich cones: In Table III are presented the essential elements of the sandwich cone designs. Except as noted, the elements of these designs are of aluminum. The reduction in allowable stress of aluminum at 550°F to approximately 20% of its room temperature value necessitates the use of titanium at this temperature for the shell face sheets and payload ring. Typically, the critical harmonic ($N_c > 2$) for 120° sandwich (and ring-stiffened) cone designs is 5 or 6, as given in the parentheses after the corresponding safety factor in Table III. It is noted that for $\beta = 0.32$ slug/ft², the sandwich face sheets are minimum gage.

The prebuckling state, buckling modes, and stress response of the (0.64, 300) sandwich design are shown in Figures 12 through 16. In these figures, meridional distance is measured from the spherical nose, and the curves start at the payload ring and terminate at the base ring. As is typical for conical shells, the $N = 2$ inextensional mode is approximately linear. The shell stresses (Figs. 15 and 16) are within safe limits for aluminum, everywhere except in the vicinity of the payload ring.* Simultaneously, high local transverse shear stresses are developed in the sandwich bond near the payload ring. Therefore, local modifications of the shell near the payload ring may be required.

Ring-stiffened cones: In Table IV are presented the essential features of the ring-stiffened cone designs. In Table IV the number of interior rings required is given in parentheses following interior ring weight. Note that two designs are presented for each ballistic coefficient at 550°F, one with aluminum interior rings and the other with titanium interior rings. For $\beta = 0.32$, the aluminum rings produce a lighter design, whereas for $\beta = 0.64$, the titanium rings are superior. In

* Note that in Figures 15 and 16, the magnitudes shown are for a safety factor of 0.3125. If a stress safety factor of 1.5 is required, the stresses shown should be increased by the factor 4.8.

contrast to the sandwich cone designs, the base rings for the ring-stiffened cones are very lightly loaded. However, comparison of Tables III and IV shows that the base ring flexural rigidity necessary to suppress the $N = 2$ mode of buckling is essentially the same for both types of construction.*

Figures 17 through 20 show the response characteristics of the modified (0.32, 300) ring-stiffened cone design.** The rapid oscillations shown in Figures 17, 19, and 20 are a manifestation of the discrete interior rings. In Figure 18 the normalized mass distribution (surface density) of the interior rings is superimposed on the normal deflection shape of the buckling mode. In practice, the average distribution of the normal deflections of several buckling modes are input to the cone design program. This is done in order to avoid weakening the shell with respect to one mode while stiffening it with respect to another. As may be seen by comparison with the results of Reference 20 (in which a uniformly ring-stiffened cone was compared to a sandwich cone of equal weight), considerable benefit is derived from the design freedom of nonuniform stiffening (see also Ref. 24).

As noted previously, the beneficial effect of meridional tension in the bay buckling criteria was neglected in obtaining these results. An additional weight reduction can be achieved by including this effect.

Tension shells: In Table V are shown the essential features of the tension shell designs. As has been noted, stringers are required, in addition to rings, to suppress large prebuckling deformations in the base region. Since the shell would be sensitive to off-design loading with stringers confined to the base region, full length stringers are used. The weight penalty incurred by so doing, if any, is small. The 300°F designs are all aluminum. Since the titanium interior rings compare favorably with the aluminum rings for the 550°F ring-stiffened cone designs and because the tension shell base rings are heavily loaded, the 550°F designs are all titanium.

Comparison of Table V with Table IV reveals the following essential differences between the ring-stiffened cone and tension shell designs.

- 1) The critical harmonic for tension shells is much greater, being in the range 15 - 20.
- 2) For the cones, the weights of the shell skin and interior rings are relatively balanced. For the tension shells, the interior ring weight is considerably less. Correspondingly, fewer rings are necessary.

* In analyzing the sandwich cones, the relatively small contribution of a closing channel ring was included in the base ring rigidities.

** The $N = 2$ buckling mode shape, being essentially the same as for the sandwich cone, is not shown.

- 3) Not only are the tension shell base rings heavily loaded, but a much greater ring flexural rigidity is required to suppress the $N = 2$ buckling mode. As a result, the distribution of weight between composite shell and base ring has shifted for the tension shells to lighter shells but heavier base rings. In other words, in choosing a tension shell over a cone, one is buying a lighter shell for heavier base ring.
- 4) Because of the probability of transition to turbulent flow, and the resulting higher heat transfer rates on the aft region of the tension shell capsules, they require heavier heat shields.
- 5) Considerable greater total entry weights are predicted for the tension shell capsules because of their higher computed drag coefficients.

Figures 21 through 25 show the response characteristics of the modified (0.32, 300) tension shell design, and Figures 26 through 29 show the response characteristics of the modified (0.64, 300) design. For the latter case, the $N = 2$ buckling mode, being essentially the same as for the prior case, has been omitted. Figures 22 and 27 show that for tension shells the buckling mode is confined to the rather shallow base region, where the hoop compressive stress resultant is greatest (cf. Fig. 21). Superimposed on these curves are the ring mass distributions obtained. As is seen, in neither case does the distribution of ring mass follow the mode shape as well as it does for the ring-stiffened cone (cf. Fig. 18). This deviation is caused by the imposition of riveted flange constraints on the interior ring design by the design program. Essentially the deviation occurs over the shallow base region where high hoop compressive stress forces the rings to be very close together in order to suppress bay buckling. If, because of the flange constraint, adjacent rings need to be separated, and consequently "beefed up" to unload the bay, the noted deviation may occur. Since the shell is much thicker for the (0.64, 300) design, this phenomenon does not occur over as large a portion of the shell, and as a result the ring mass deviation is limited to a smaller region.

Configuration comparison.— Summarized in the table below are the total structure plus heat shield (nonusable) weights, excerpted from Tables III, IV, and V, for each design obtained.

β	T	Sand. cone	R.S. cone	Tension shell
.32	300	585(.133)	559(.127), -	605(.116)
	550	647(.147)	628(.143), 640(.145)	728(.140)
.64	300	703(.080)	760(.086), -	790(.076)
	550	781(.089)	890(.101), 866(.098)	929(.089)

Given in parentheses are the fractional parts of the total entry weight which these weights represent. The first column under the heading R.S. cone corresponds to the ring-stiffened cone designs with aluminum interior rings, whereas the second column corresponds to titanium interior rings.

The first conclusion to be drawn from this comparison is that in all cases the 550°F designs are heavier than the 300°F designs. For the lightweight heat shield material (SLA-561) considered, the reduction in heat shield weight to be gained by going to higher structural temperatures does not compensate for the required increase in structural weight. With respect to the cone designs, it is seen that ring-stiffened construction is lighter than sandwich construction at $\beta = 0.32$ slug/ft², whereas the reverse is true at $\beta = 0.64$. The poor showing of the sandwich cones at low ballistic coefficient results primarily from minimum face sheet gage and adhesive weight limitations on their design for low loading. If one assumes, for each wall construction, a linear variation of nonusable weight with the ballistic coefficient in the range $0.32 \leq \beta \leq 0.64$, it follows that for $\beta < 0.42$ slug/ft², ring-stiffened construction is lighter than sandwich construction. For $\beta > 0.42$, ring-stiffened construction may still be desirable because of ease of fabrication, inspection, making design changes, and high reliability relative to sandwich construction.

Although the total nonusable weight required in the tension shell designs is greater than for the cones, because of its much greater total entry weight, the corresponding weight fractions are lower. These results, therefore, bear out the potential usefulness of the tension shell concept. However, it should be noted that, for a given ballistic coefficient, the total entry weight is directly proportional to the average drag coefficient. The structural weight, on the other hand, is affected to a much lesser degree by drag coefficient. If flow separation occurs on the tension shell capsules, the computed drag coefficient is too large. In effect, the drag coefficient used ($C_D = 1.78$), and consequently the total entry weights shown in Table V, having been computed neglecting the effect of flow separation, represent only upper bound values.

Aeroshell weight correlation.- In order to reveal the effects of capsule size, maximum dynamic pressure, and material, it is desirable to fit the aeroshell weights obtained with an algebraic correlation. For this purpose, the weights associated with the low temperature sandwich cone designs were chosen as being typical of optimized Mars capsules.

In Reference 24, least-square weight correlations are derived for both minimum gage and unconstrained base rings and shells from the results of optimizing 120° truncated sandwich cones for two base diameters and three uniform pressure loadings. These shell correlations have been modified to account for adhesive bond and nose section weight. Also, the constants of these correlations have been adjusted to fit the low temperature results

shown in Table III. The base ring correlations were thereby made to reflect the additional weights of sandwich closure and base ring tube support.† Additionally, the buckling pressure p was converted to peak dynamic pressure q_d by use of the approximate relation

$$p = 3.85 q_d$$

which includes a factor of safety of 2.25. The resulting correlations are the following:

$$\text{Base Ring: } W/\pi \rho r_B^3 = 21.0(q_d/E) \cdot 75 \quad (5)$$

$$= 8.35[(q_d/E)(t^*/r_B)^2] \cdot 333 \quad (6)$$

where t^* is the tube minimum gage and the larger of the two formulas applies.

$$\text{Shell: } W/S \text{ (lb/in}^2\text{)} = .00139 + 4\tau \rho t_c \quad (7)$$

$$= .00139 + 2\rho/\tau t_c^* + t_f^* \quad (8)$$

where

$$S = 3.63 r_B^2 - .26 r_P^2$$

$$t_c = .98 x(1 - 1.58 x \cdot 5)r_B$$

$$x = [(q_d/E\tau)(1 - r_P/r_B)] \cdot 4 (1 + r_P/r_B) \cdot 6$$

$$t_c^* = .993 y(1 - 2.57 v \cdot 5)r_B$$

$$y = [(q_d/E)(1 - r_P/r_B)(r_B/t_f^*)] \cdot 667 (1 + r_P/r_B)$$

Equation (7) applies if $t_c \geq t_f^*/\tau$; otherwise, Equation (8) applies.

For completeness, a simple correlation for the payload ring weight is $W/\pi \rho r_P = 1.5 \text{ in.}^2$. Adding the three correlations gives an estimate of the total aeroshell structural weight.

Effect of size and dynamic pressure: The base radius r_B and maximum dynamic pressure q_d are explicit variables in Eqs. (5) through (8). Consequently, these formulas are valid for any entry trajectory. In Figure 30, Eqs. (5) through (8) are displayed graphically for all-aluminum designs with a payload to base radius ratio of 0.3. In Figure 30, the 19 foot base diameter point designs for $\beta = 0.32$ and 0.64 slug/ft^2 are represented by the two small circles on each plot. On the base ring

† The estimated weight of shell splices for the low temperature designs is negligible.

and shell weight plots the minimum gage boundary is shown. To the left of this boundary, the designs are constrained by minimum gage. Thus as the maximum dynamic pressure increases, the minimum capsule size which is not limited by minimum gage is reduced.

Effect of material: From Eqs. (5) through (8) one can extract the relevant material parameters. These are given in the table below.

	<u>Unconstrained</u>	<u>Minimum gage</u>
Base ring	$\rho/E \cdot 75$	$\rho(t^*2/E) \cdot 333$
Shell ^a	$\rho/E \cdot 4$	$\rho[t_f^*/r_B + .0114(q_d r_B/E t_f^*) \cdot 667]$

In selecting a material, these parameters should be used with care since for a given capsule size and maximum dynamic pressure, one material may be constrained by minimum gage whereas another may not. If two materials are both constrained or both unconstrained, then the one that has the least value of the corresponding parameter is best.

For typical values of base diameter and maximum dynamic pressure, Eqs. (5) through (8) were used to obtain base ring and shell weights for several materials. The results, along with the assumed material properties, are presented in Table VI. Since boron and graphite filaments are at present very expensive, estimates of the current prices for composites made with these filaments are shown. As the table shows, the graphite filament composite would be an attractive material if it were not so expensive.

DESIGN EVALUATION

Fabrication Feasibility

Manufacturing processes and facilities. - A study of fabrication techniques and facilities has been made to support the preliminary designs obtained. The primary objective of this study is to verify a capability for fabricating the large thin gage shells of the several structural concepts. The study encompasses material availability, forming of structural elements, joining and attaching techniques, and fabrication of large shell structures. The geometric configurations investigated are illustrated in Figure 31. Ring-stiffened and honeycomb sandwich structures are considered for the blunt cone, and ring-stiffened structures are considered for the tension shell.

^aThe shell parameters ignore the material dependence of adhesive weight. The constant 0.0114 shown in the minimum gage parameter is based on the assumption that $1 - 2.57 y \cdot 5 = .75$.

Material availability: The materials of primary concern are sheets of titanium and aluminum alloys. Parameters of interest are minimum gage and maximum sheet width. The use of relatively thin gage material is necessary for the face sheets of the honeycomb sandwich shell and the stiffening rings of the ring-stiffened shell. Maximum sheet width is desirable in both configurations to minimize the number of joints in the shell which would influence cost and possibly weight. A minimum material thickness of 0.016 in. was used for the aluminum alloy facings of the honeycomb sandwich (cf. Table III). This is a standard commercial gage which is available in all of the common structural alloys. Sheet width, however, is somewhat more restrictive. For aluminum the maximum width available commercially in thicknesses under 0.025 in. is 36 in. With sheets of this width, each facing of the honeycomb shell would require 20 "pie-shaped" sections. With a special mill run, which requires a minimum order of 4000 lb, sheets of 0.016 stock 55 inches wide can be provided. Shells of 0.016 in. stock would then require only 13 sections. In thicknesses over 0.020 in., widths of 62 in. can be provided. In gages over 0.020, sheet width is limited by the length of the mill rolls. Below 0.020 in., sheet width is governed by the malleability of the alloy. The less malleable alloys tend to form edge imperfections which have to be trimmed off, thus reducing the effective width available from a given roll length.

Sheet thickness in the titanium alloys present no availability problem since the minimum gage used is 0.016 in. (cf. Table III), and the minimum gage available commercially is 0.010 in. Sheet width availability, however, is more limited. The maximum sheet width available in gages of 0.020 in. and less, is 42 in., and the availability in this width is contingent upon the mill being permitted to coil the sheet. Uncoiled flat sheets are available only in 36 inch widths. Sheet width, as it may relate to a weight penalty of joining, is not critical in the titanium shells, however, since the shell sections can be welded with essentially no weight penalty.

Forming of structural elements: No forming operations need be performed on conical shell sections of thicknesses less than approximately 0.025 in. Such thin sections, sheared to the proper shape in a flat pattern merely need to be placed in a layup mold or assembly fixture, where they will conform to the shape of the mold or fixture by elastic flexing. Thicker sections assembled in this manner may retain excessive initial stresses. If the nature of the structural assembly permits, these stresses can be relieved by a normalizing heat treatment. If the assembly will not tolerate such heat treatment, i.e., bonded structures, the shell sections must be preformed before assembly. In conical shells, these sections can be formed by rolling. Sections of the tension cone, because of their double curvature, would have to be formed by a drawing or stretching operation.

The Z-section rings of the ring-stiffened configurations will be formed into straight sections by the rolling of strip stock. For small radius rings, these sections will subsequently be formed into rings by roll bending. Rings of larger radius can be elastically formed into the

assembly fixture if the resulting initial stresses can be tolerated structurally. The base rings will be fabricated by first rolling strip stock into a straight tubular section and butt welding the seam. This tube, approximately 65 ft long, will be plugged at each end and pressurized with water or filled with sand. The filled tube will then be formed into a ring of approximately 226 in. diameter by roll bending. After the ring is formed, the filler material will be removed and the ends trimmed. The resulting joint will be welded or spliced mechanically on assembly.

Joining and attaching techniques: A study was made of basic joining and attaching techniques to determine their applicability to the capsule structure. Welding, resin bonding and mechanical fastening are the principal techniques studied. Of principal interest in welding are the weldability of thin sheets of aluminum and titanium alloys and the availability of electron beam welding chambers which would accommodate the capsule structure. Adhesive bonding has its greatest application in the honeycomb sandwich shells where bond thickness has a strong influence on shell weight and where strength at elevated temperatures varies with bond thickness. Special purpose mechanical fasteners are of interest in the honeycomb sandwich shells. In these structures fastener inserts are required for the attachment of structural members, and sandwich core depth places some restriction on fastener application.

Minimum gages for reliable welding by conventional shielded arc processes would be approximately 0.020 in. for titanium alloys and approximately 0.025 in. for aluminum alloys. These estimates are based upon the size of structures involved, the relatively long seams that may be required and the necessity to minimize distortion. Thinner gages can be welded satisfactorily by the electron beam technique. Facilities for electron beam welding of large forms as those under consideration are very limited, however. As a result, at least for the near future, the cost of this process as applied to the aeroshell is likely to be high, and the availability of such facilities is likely to present scheduling problems. Aluminum alloy 7039 or titanium alloy Ti-6Al-6V-2Sn are recommended for welded structures.

Resin bonding finds its greatest application in the honeycomb sandwich structures wherein the facing sheets are bonded to each side of the honeycomb core. Other structural components may also be assembled by bonding. However, the weight contribution of these secondary applications is small compared to the face sheet adhesive weight. Parameters of primary interest are the bond strength at 300°F and 550°F and the bond surface density. Conventional bonds, such as Narmco's Metal Bond 302HP, have demonstrated reliable performance in many aerospace structures subjected to temperature environments up to the 550°F. Another material that has been qualified on fiberglass structures at 500°F for fifteen minutes is Epon 901/B3. This material is covered by specification MIL-A-5020, Type II. These materials are applied in varying amounts depending upon the temperature to which they are to be subjected. Weights of the bonded joint may vary from 0.05 lb/ft² per face sheet for 300°F service to as much as 0.20 lb/ft² for 500°F service. In order to minimize structural weight

it is desirable that the lightest bond consistent with adequate strength be specified. Manufacturers suggest bond weights of 0.1 lb/ft² per face sheet for 300°F service and 0.135 lb/ft² for service at 500°F. The higher density bond forms larger fillets between the face sheet and the core facing. These larger fillets provide a larger bonded area on the honeycomb cell. This increased bond area compensates for the reduction in nominal bond strength at elevated temperatures.

Rivets are used to attach the rings (and stringers) to the shell skin of the ring-stiffened designs. The weights of standard rivets can be expressed by simple equations since rivet geometry is usually based upon rivet diameter. The following equation, expressing the weight of a single brazier head rivet in terms of rivet diameter and shell thickness, is used in the design programs to estimate rivet weight.

$$W = \pi \rho d_r^2 (.816 d_r + t/4)$$

Blind rivets are necessary in several locations to assemble the base ring to the aeroshell. Such fasteners are required since the base ring is a closed section, permitting access to only one end of the fastener. These are standard fasteners which are covered by government specifications. They are available from several sources in a variety of materials including aluminum alloys, monel and stainless steel. Grip lengths on the smaller sizes, typically 1/8 to 3/16 diam, are too short to reach through the honeycomb sandwich. Therefore, it is necessary to provide cup-shaped metal inserts in the sandwich in some locations to permit the attachment of the base ring with these fasteners.

Fabrication of large shell structures: The basic technique of assembling and bonding the sandwich aeroshell is common to numerous aircraft and aerospace structures. The processing of such large shells, however, requires heavy industrial facilities to produce the required tooling and to cure the assembled structure. It is anticipated that the structural layup would be cured at a temperature of between 300°F and 350°F at an autoclave pressure of approximately 50 psi. Vendors are available in the Southern California area, as well as in other sections of the country, with shop facilities capable of producing tooling for the capsule structures. In many instances, these same vendors have facilities for assembling and curing the structural shell.

A cursory study was made of explosive forming techniques as they might apply to the ring-stiffened configurations. Although it appears that conventional airframe manufacturing processes will be satisfactory, some cost and structural advantages might be realized with explosive forming. Tooling may consist of a steel-reinforced concrete die whose internal surface is smoothed and sized with a resin layer. It is likely that the thin shells would have to be formed between initially flat plates of mild steel or aluminum. Each plate would be perhaps one inch thick. Appropriate restraints would be required at the edge of the die, and a grid of the forming charge would be suspended over the plates at the proper standoff distance. This assembly would be submerged in a natural body of water to a depth of 30 feet to 40 feet and the charge ignited.

Alternate section for aeroshell base ring. - The structural designs which have evolved from this study are based upon the use of base rings of thin wall circular cross section. Although the feasibility of this cross section has been established with tubing fabricators, a cross section which is more amenable to fabrication and assembly could be developed. Such an alternate section should provide the required flexural rigidity without incurring a significant weight penalty.

One alternate base ring section is illustrated in Figure 32. For comparison, an equivalent circular section is also shown. The moment of inertia (about a centroidal axis parallel to the cone generator) of the alternate section is approximately equal to that of the circular section. The weight of the resulting section is greater than that of the circular section by a few percent. However, this weight penalty may be compensated by the fact that tube support is not required with the alternate section.

Detail Drawings of Optimized Designs

Design layout drawings were prepared to illustrate typical mechanical details of the various structural concepts as they applied to the two aeroshell geometries. Although materials, material gages, and shell dimensions vary with ballistic coefficient and structural temperature, the basic structural configuration does not change. Therefore, design layouts are presented for only one set of conditions, $\beta = 0.32$ slug/ft² and $T = 300^{\circ}\text{F}$.

Honeycomb sandwich cone. - Figure 33 shows a preliminary design layout for a 120° cone of sandwich construction. The basic structural components in this concept are the shell assembly, the base ring and the payload mounting ring. It is anticipated that the shell will be assembled in two principal stages. The nose section including the payload mounting ring would be layed up on a male mold, bagged, and cured. This subassembly would then be incorporated into the rear shell structure in a second lay-up operation on a conical male mold. The base ring would subsequently be assembled to this shell assembly with conventional structural fasteners. The base ring is attached to the shell with attach doublers and tube supports. These members are disposed in a manner which will most effectively react the tension loads of the shell.

The principal materials in this assembly are 7075-T6 aluminum alloy for the sandwich face sheets, payload mounting ring and base ring; 5052 aluminum alloy bonded core with a density of 5.2 lb/ft³, and adhesive HT424 (Bloomingdale Rubber Company) sandwich bond.

Ring-stiffened cone. - Figure 34 illustrates the conical configuration as designed for ring-stiffened construction. In this design current state-of-the-art airframe construction techniques are used. Shell segments of 7039 alloy are joined by shielded arc welding into a continuous flat development of the conical shell. This flat development is elastically formed to the conical shape over stiffening rings which are located in an assembly fixture. The rings are riveted to the shell and the shell joint is spliced and riveted. The spherical nose, which is formed by spinning, is attached to the conical shell section by a riveted splice joint. As in the sandwich design, the base ring is attached to the shell with the ring attach doublers and support members. Lacking the edge stiffness of the sandwich design, the outer edge of the ring-stiffened design is reinforced with a minimum-gage angle ring. The payload mounting ring is a flanged angle section which is machined from a ring forging of 7075 aluminum alloy and riveted to the conical shell. In this design self-locking spline nuts have been provided in the web of the angle section to permit attachment of the payload. This interface would, of course, have to be tailored to the payload structure when that system is defined.

Principal materials employed in this design are 7039 aluminum alloy for the shell and base ring and 7075-T6 aluminum alloy for the payload mounting ring and stiffening rings. Dimensions and locations of the stiffening rings for a ballistic coefficient of 0.32 slug/ft² and a temperature of 300°F are tabulated in Table VII. Similar data for a ballistic coefficient of 0.64 slug/ft² are presented in Table VIII.

OA.833 tension shell. - Figure 35 shows a ring-stiffened design for the OA.833 tension shell. The structural concept here is very similar to the ring-stiffened cone, the main difference being the addition of radial stiffeners (stringers) every 4° around the inside of the shell. The tension shell shape does not extend forward of the payload ring. Shell sections could be die-formed and welded together to form the complete shell. Roll formed rings and stringers would be located in an assembly fixture and the welded shell assembly would be riveted to these stiffeners. As in the previous designs, the base ring is attached to the shell assembly with a series of doublers and supports. Where the stringer depth permits, they are notched to fit over the stiffening rings. Where the depth of the rings approaches the depth of the stringers, the stringers are discontinuous over the ring. Materials for this capsule are 7039 aluminum alloy for the shell and base ring, and 7075 alloy for the stiffeners and payload mounting ring. Dimensions and locations of the stiffening rings for a ballistic coefficient of 0.32 slug/ft² and a temperature of 300°F are tabulated in Table IX. Similar data for a ballistic coefficient of 0.64 slug/ft² are presented in Table X.

CONCLUDING REMARKS

For each configuration (120° sandwich cone, 120° ring-stiffened cone, and OA.833 tension shell) and for each ballistic coefficient (0.32 and 0.64 slug/ft²) considered, the 300°F designs have significantly smaller nonusable (total structure plus heatshield) weights than the 550°F designs. Since for most materials there is very little stiffness or strength degradation up to 300°F, this temperature is probably very close to the optimum structural temperature.

As a result of the extra design freedom of variable ring size and spacing, ring-stiffened construction is lighter than sandwich construction at the lower ballistic coefficient. This result is reinforced by several practical disadvantages of sandwich construction. As noted in Reference 1, these are related to ease of fabrication, inspection, making local design changes, and the unknown effect of sterilization and the long vacuum soak of interplanetary transit on the adhesive bond.

In choosing a ring-stiffened tension shell over a ring-stiffened cone, one is buying a lighter composite shell (due to less interior ring weight) for a heavier base ring and heatshield. The result is a somewhat greater nonusable weight. The attractiveness of the tension shell configuration is, therefore, due primarily to its higher computed drag coefficient, which for a given ballistic coefficient allows a significantly greater total entry weight. However, because there are extensive regions of positive pressure gradient in the shock layer, it is probable that, due to flow separation, the high drag result will be degraded over major portion of the entry trajectory. Because of this uncertainty, the total entry weights presented for the tension shell capsules should be viewed only as upper bound values. One may therefore conclude that, at the present state of knowledge, the ring-stiffened conical aeroshell offers the greatest benefit for Mars applications.

It should be noted that in order to achieve lightweight base rings with the required flexural rigidity, thin wall tubular base rings have been employed. Although weight allowances are made for additional tube support, it is not known how thin a tube can be before the cross section distorts locally at the shell interface. If this occurs, the ring no longer provides the necessary support, and the design may fail in an $N = 2$ buckling mode. Therefore, additional studies of the effectiveness of thin wall tubular base rings are recommended.

APPENDIX

COMPARISON OF THEORETICAL FLOW FIELD RESULTS WITH EXPERIMENT

A transient finite different computer program has been used in this study to calculate aerodynamic loads. Until recently, there has been very little experimental pressure data for capsule shapes of interest for Martian entry, with which the accuracy of the computer program could be evaluated. The purpose of this section is to compare zero and a simplified finite angle of attack transient computer program calculations with the 120° sphere-cone experiments presented in Reference 6.

Two-Dimensional Flow

The zero angle of attack program utilized in this study has been described briefly in this report and in more detail in Reference 5. A comparison of theoretical and experimental shock shape and pressure distribution are given in Figures 36 and 37, respectively. The theoretical finite difference shock shape, as well as a first approximation integral relation result, is compared with experiment in Figure 36. The time dependent shock position result is almost identical with experiment. The integral relation shock position is also very accurate, although the shock stand-off distance is underestimated in the base corner regions. Also shown in Figure 36 is the finite difference grid spacing along the body. The grid spacing in the direction normal to the body was established by dividing the shock layer into five equidistant cells.

The theoretical pressure distribution is very close to the experiment over the majority of the body except in the region of the sphere-cone junction and the base corner. The inviscid pressure drop and recovery at the sphere-cone junction probably does not appear in the experiment because of viscous effects. The deviation between the theoretical and experimental pressure distribution in the base corner region may be due to low Reynolds number effects.

Angle of Attack Flow

The angle of attack computation is carried out by performing calculations similar to those in the two-dimensional program in both the windward and leeward planes of symmetry. A crossflow approximation is used to couple the two computational planes. The flow equations, the crossflow approximation and the comparison of theory and experiment are discussed in the following paragraphs.

The body is described in a cylindrical x, r, θ coordinate system with the x -axis along the axis of symmetry of the body. A plane of symmetry of the flow field is formed by the body axis and the freestream velocity vector.

The angular coordinate θ is measured from the leeward portion of this plane, $\theta = 0$, to the windward portion, $\theta = \pi$. Radial distances from the x-axis are measured by the r-coordinate. The fluid velocity components are respectively u, v, w in the x, r, θ directions.

The difference equations are based on the conservation laws for fluid flow written in the form

$$\rho_t + (\rho u)_x + (\rho v)_r + (\rho w/r)_\theta + \rho v/r = 0$$

$$(\rho u)_t + (\rho u^2 + p)_x + (\rho uv)_r + (\rho uw/r)_\theta + \rho uv/r = 0$$

$$(\rho v)_t + (\rho uv)_x + (\rho v^2 + p)_r + (\rho vw/r)_\theta + \rho(v^2 - w^2)/r = 0$$

$$(\rho w)_t + (\rho uw)_x + (\rho vw)_r + \left[(\rho w^2 + p)/r \right]_\theta + 2\rho vw/r = 0$$

$$(\rho E)_t + (\rho uH)_x + (\rho vH)_r + (\rho wH/r)_\theta + \rho vH/r = 0$$

where the subscripts t, x, r, θ denote partial differentiation t being time. Using the state equation for the internal energy in the form

$$e = e(p, \rho)$$

the total fluid energy E is defined as

$$E = e + \frac{1}{2}(u^2 + v^2 + w^2)$$

The remaining variable H is the stagnation enthalpy

$$H = E + p/\rho$$

In the program the ideal gas equation of state is employed

$$p = (\gamma - 1)\rho e$$

The system of equations is identical to the two-dimensional case except for additional terms involving the crossflow velocity w and θ -derivatives. By symmetry, the flow variables u, v, p, ρ and h are even functions of θ , whereas w is an odd function of θ . Cosine and sine polynomials respectively are used to relate points in similar locations of different planes, $\theta = \text{constant}$, through the shock layer. For a first approximation, the variations in θ are completely described by the values of the variables in the $\theta = 0, \pi$ planes. In these planes, the crossflow velocity, w, vanishes, and the four equations for the remaining variables u, v, p, ρ resemble the two-dimensional equations except for the nonzero θ -derivative terms. In this simplified program, the crossflow was determined from the requirement that the

stagnation enthalpy be constant in the $\theta = 0, \pi/2$ and π planes. The quantities approximated by trigonometric polynomials are $u, v, w, \rho, p,$ and h . Since u, v, ρ, p and h are even functions of θ , the simplest approximation is of the form

$$u(x, r, \theta) = u_0(x, r) + u_1(x, r) \cos \theta$$

The coefficients in this equation are evaluated in terms of the value of u at $\theta = 0, \pi$ and the result is

$$u_0 = \left(u^{(0)} + u^{(\pi)} \right) / 2$$

$$u_1 = \left(u^{(0)} - u^{(\pi)} \right) / 2$$

Here and in the following, a superscript in parenthesis indicates the value of θ at which the associated variable is evaluated. Similar expressions hold for $v, \rho, p,$ and h .

The crossflow velocity is an odd function of θ and is approximated by the polynomial

$$w(x, r, \theta) = w^{(\pi/2)}(x, r) \sin \theta$$

When the polynomial expressions for $u, v,$ and h in the $\theta = 0, \pi/2,$ and π planes are combined with the constant stagnation enthalpy condition, $H^{(0)} = H^{(\pi/2)} = H^{(\pi)}$, the following expression for $w^{(\pi/2)}$ is obtained:

$$w^{(\pi/2)} = - .50 \left\{ \left(u^{(0)} - u^{(\pi)} \right)^2 + \left(v^{(0)} - v^{(\pi)} \right)^2 \right\}^{1/2} \quad (A1)$$

The θ -derivative terms in the planes of symmetry are evaluated as follows:

$$\left[(\rho w / r)_{\theta} \right]^{(0)} = w^{(\pi/2)} \left[\rho / r \right]^{(0)}; \quad \left[(\rho w / r)_{\theta} \right]^{(\pi)} = -w^{(\pi/2)} \left[\rho / r \right]^{(\pi)}$$

$$\left[(\rho u w / r)_{\theta} \right]^{(0)} = w^{(\pi/2)} \left[\rho u / r \right]^{(0)}; \quad \left[(\rho u w / r)_{\theta} \right]^{(\pi)} = -w^{(\pi/2)} \left[\rho u / r \right]^{(\pi)}$$

$$\left[(\rho v w / r)_{\theta} \right]^{(0)} = w^{(\pi/2)} \left[\rho v / r \right]^{(0)}; \quad \left[(\rho v w / r)_{\theta} \right]^{(\pi)} = -w^{(\pi/2)} \left[\rho v / r \right]^{(\pi)}$$

$$\left[(\rho w h / r)_{\theta} \right]^{(0)} = w^{(\pi/2)} \left[\rho h / r \right]^{(0)}; \quad \left[(\rho w h / r)_{\theta} \right]^{(\pi)} = -w^{(\pi/2)} \left[\rho h / r \right]^{(\pi)}$$

In the computation scheme, these terms, which are functions only of $\theta = 0$ and π flow variables, are treated as inhomogeneous terms that are known from the last time step. Thus, in the simplified angle of attack program, the windward and leeward plane of symmetry calculations are coupled by a crossflow approximation that only involves flow variables in these planes at the previous time step.

An alternate higher order approximation, that is applicable for cones, has been suggested by P. Bobbitt of the Langley Research Center of NASA. The experimental results presented in Reference 6 indicate that the circumferential pressure distribution is quite flat in the region of the leeward plane.

The condition $(\partial^2 p / \partial \theta^2)^{(\pi)} = 0$, is therefore applicable and the trigonometric polynomial describing the circumferential pressure distribution is

$$p = .25 (p^{(0)} + 3p^{(\pi)}) + .5 (p^{(0)} - p^{(\pi)}) \cos \theta + .25 (p^{(0)} - p^{(\pi)}) \cos^2 \theta$$

If the distributions for u , v , and w are assumed to be similar to the pressure, the expression for the crossflow term becomes

$$w^{(\pi/2)} = - .433 \left\{ (u^{(0)} - u^{(\pi)})^2 + (v^{(0)} - v^{(\pi)})^2 \right\}^{1/2} \quad (A2)$$

A comparison of the two crossflow models presented in Equations (A1) and (A2) shows that the flatter property profile in the leeward plane reduces the coupling influence of the crossflow.

Numerical solutions utilizing the two crossflow models were compared with the 10° angle of attack experiments of Reference 6. A comparison of the theoretical and experimental pressure distribution in the windward and leeward planes of symmetry is shown in Figure 38. The 0.433 crossflow model closely approximates the experimental results except in the region of the sphere-cone junction. The decrease in pressure predicted in this region is probably not present in the experiment because of viscous effects. The 0.50 crossflow result is similar to the 0.433 result, except that the windward pressures are slightly underestimated and the leeward pressures are slightly overestimated.

A 20° angle of attack solution was also attempted for a 120° sphere-cone. The 20° angle of attack experiment indicated that the stagnation point is located on the conical portion of the body, whereas the theory indicated that the stagnation point is on the sphere-cap. The pressure levels calculated in the windward plane are substantially below the experimental values. It is concluded that for the given vehicle geometry and flow conditions, $\alpha = 20^\circ$ exceeds the limit of application of the simplified angle of attack computer program.

REFERENCES

1. Guy, L.D.: Structural Design Options for Planetary Entry. Paper presented at the AIAA/ASME 9th Structures, Structural Dynamics and Materials Conference (Palm Springs, California), April 1968.
2. Cohen, G.A.; Foster, R.M.; and Schafer, E.M.: Analysis of Conceptual Designs for the Voyager Entry Capsule. NASA CR No. 66580, 1968.
3. von Neumann, J.; and Richtmyer, R.: A Method of the Numerical Calculation of Hydrodynamic Shocks. J. Appl. Phys., vol. 21, 1950, p. 232.
4. Godunov, S.K.: Finite Difference Method for Numerical Computation of Discontinuous Solutions of the Equations of Fluid Dynamics. Mat. Sbornik, vol. 47, no. 3, 1959, p. 89 (Translated by I. Bohachevsky).
5. Masson, B.S.; Taylor, T.D.; and Foster, R.M.: Application of Godunov's Method to Blunt Body Calculations. AIAA J., vol. 7, no. 4, April 1969.
6. Stallings, R. L.; and Tudor, D. H.: Experimental Pressure Distributions on a 120° cone at Mach Numbers from 2.96 to 4.63 and Angles of Attack from 0° to 20° . NASA TN D-5054, 1969.
7. Camac, M.: CO_2 Relaxation Process in Shock Waves. AVCO Everett Res. Rep. 194, October 1964.
8. Wray, K.L.; and Freeman, T.S.: Shock Front Structure in O_2 at High Mach Numbers. J. Chem. Phys., vol. 40, no. 10, May 1964, p. 2785.
9. Jones, R.A.; Bushnell, D.M.; and Hunt, J.L.: Experimental Flow Field and Heat Transfer Investigation of Several Tension Shell Configurations at a Mach Number of Eight. NASA TN D-3800, 1967.
10. Goldberg, L.: The Structure of the Viscous Hypersonic Shock Layer. G. E. Document R65SD50, December 1965.
11. Hayes, W.D.; and Probstein, R.F.: Hypersonic Flow Theory. Academic Press (New York), 1959.
12. Ferri, A.; Zakkay, V.; and Ting, L.: Blunt-Body Heat Transfer at Hypersonic Speed and Low Reynolds Numbers. J. Aerospace Sci., vol. 28, December 1961, p. 962.
13. Hoshizaki, H.: Heat Transfer in Planetary Atmospheres at Super-satellite Speeds. ARS J., vol. 32, 1962, pp. 1544-1551.

14. Scala, S.M.; and Gilbert, L.M.: Theory of Hypersonic Laminar Stagnation Region Heat Transfer in Dissociating Gases. G. E. Document R63SD40, April 1963.
15. Fay, J.A.; and Riddell, F.R.: Theory of Stagnation Point Heat Transfer in Dissociated Air. J. Aeron. Sci., vol. 25, 1958, pp. 73-85.
16. Lees, L.: Laminar Heat Transfer over Blunt-Nosed Bodies at Hypersonic Speeds. Jet Propulsion, vol. 26, no. 4, April 1956, pp. 259-269.
17. Cheng, H.K.: The Blunt-Body Problem in Hypersonic Flow at Low Reynolds Numbers. Cornell Aero. Lab. Rep. AF1285-A, 1963.
18. Rose, R.H.; Probst, R.F.; and Adams, M.C.: Turbulent Heat Transfer Through a Highly Cooled Partially Dissociated Boundary Layer. AVCO Res. Rep. 14, January 1958.
19. Cohen, G.A.: Buckling of Axially Compressed Cylindrical Shells with Ring-Stiffened Edges. AIAA J., vol 4, no. 10, October 1966, pp. 1859-1862.
20. Cohen, G.A.: The Effect of Edge Constraint on the Buckling of Sandwich and Ring-Stiffened 120 Degree Conical Shells Subjected to External Pressure. NASA CR-795, 1967.
21. Cohen, G.A.: Evaluation of Configuration Changes on Optimum Structural Designs for a Mars Entry Capsule. NASA CR-1414, 1969.
22. Anon.: NASA Space Vehicle Design Criteria - Buckling of Thin-Walled Circular Cylinders. NASA SP-8007, 1965.
23. Seide, P.: The Stability of Thin Conical Frustums Subjected to Axial Compression and Internal or External Uniform Hydrostatic Pressure. AFBMD-TR-61-37, March 1961.
24. Cohen, G.A.: Structural Optimization of Sandwich and Ring-Stiffened 120 Degree Conical Shells Subjected to External Pressure. NASA CR-1424, 1969.
25. Steinbacher, F.R.; and Gerard, G.: Aircraft Structural Mechanics. Pitman Publ. Corp., 1952, p. 271.
26. Baruch, M.; and Singer, J.: General Instability of Stiffened Circular Conical Shells under Hydrostatic Pressure. Aeron. Quart., vol. 16, May 1965, pp. 187-204.

27. Cohen, G.A.: Computer Analysis of Asymmetrical Deformation of Orthotropic Shells of Revolution. AIAA J., vol. 2, no. 5, May 1964, pp. 932-934.
28. Cohen, G.A.: Computer Analysis of Asymmetric Buckling of Ring-Stiffened Orthotropic Shells of Revolution. AIAA J., vol. 6, no. 1, January 1968, pp. 141-149.
29. Strauss, E.L.: Superlight Ablative Systems for Mars Lander Thermal Protection. J. Spacecraft Rockets, vol. 4, no. 10, October 1967, pp. 1304-1309.
30. Swann, R.T.; Pittman, C.M.; and Smith, J.C.: One-Dimensional Numerical Analysis of the Transient Response of Thermal Protection Systems. NASA TN **D-2996**, 1965.

TABLE I

FLIGHT CONDITIONS AT PEAK DYNAMIC PRESSURE

Freestream Conditions

Altitude, ft	61 000
Velocity, V_{∞} , ft/sec	11 000
Density, ρ_{∞} , slug/ft ³	3.8×10^{-6}
Temperature, T_{∞} , °K	100
Pressure, p_{∞} , psf	0.773
X_{CO_2} , mole fraction	1.0
Dynamic pressure, q_d , psf	228
Angle of attack, α , deg	0

Shock Layer Stagnation Point Conditions

Pressure, p_s , psi	3.048
Temperature, T_s , °K	2713
Molecular weight	36.5
X_{CO} , mole fraction	0.311
X_{CO_2} , mole fraction	0.518
X_{O_2} , mole fraction	0.140
X_O , mole fraction	0.031

TABLE II

OA.833 TENSION SHELL FLIGHT CONDITIONS AT PEAK DYNAMIC PRESSURE,
NONZERO ANGLE OF ATTACK

[From Ref. 2]

Freestream Conditions

Altitude, ft	66 000
Velocity, V_∞ , ft/sec	9 550
Density, ρ_∞ , slug/ft ³	2.89×10^{-6}
Temperature, T_∞ , °K	100
Pressure, p_∞ , psf	0.585
X_{CO_2} , mole fraction	1.0
Dynamic pressure, q_d , psf	132
Angle of attack α_e , deg	12

Shock Layer Stagnation Point Conditions

Pressure, p_s , psi	1.83
Temperature, T_s , °K	2445
X_{CO} , mole fraction	0.185
X_{CO_2} , mole fraction	0.72
X_{O_2} , mole fraction	0.088
X_O , mole fraction	0.0092

TABLE III

SANDWICH CONE DESIGNS

	<u>(.32 slug/ft², 300^oF)</u>	<u>(.32, 550)</u>	<u>(.64, 300)</u>	<u>(.64, 550)</u>
(1) Stability Safety Factor				
$\lambda_{SF} = 2.22(2)$		2.25(2)	2.26(2)	2.29(2)
$\lambda_{SF} = 2.48(5)$		2.17(6)	2.16(5)	2.12(5)
(2) Shell Aft of Payload Ring ^a				
$t_c = 0.947$ in.		0.644	0.150	1.024
$t_f = 0.016$ in.		0.016(T1)	0.019	0.016(T1)
W = 320 lb		397	984	463
(3) Base Ring ^b				
t = 0.035 in.		0.039	0.042	0.048
R = 4.37 in.		4.85	5.15	5.99
W = 92 lb		110	128	159
(4) Payload Ring				
W = 16 lb		24(T1)	16	24(T1)
(5) Heat Shield				
W = 126 lb		79	138	93
(6) Nonusable Entry Weight ^c				
W = 585 lb		647	702	781
(7) Total Entry Weight				
W = 4400 lb		4400	8800	8800

^a Includes 0.1 and 0.135 lb/ft²/face sheet adhesive weight for 300^oF and 550^oF designs, respectively. Also includes weight allowance for splices.

^b Includes weight allowances for sandwich closure and tube support.

^c Includes allowance for nose section.

TABLE IV

RING-STIFFENED CONE DESIGNS

	<u>(.32 slug/ft², 300°F)</u>	<u>(.32, 550)</u>	<u>(.64, 300)</u>	<u>(.64, 550)</u>		
(1) Stability Safety Factor $\lambda_{SF} = 2.16(2)$ $= 2.16(5)$		2.25(2) 2.31(6)	2.25(2) 2.09(5)	2.03(2) 2.03(5)	2.19(2) 2.19(5)	2.25(2) 2.06(5)
(2) Unstiffened Shell Aft of Payload Ring t = 0.042 in. W = 180 lb		0.036(Ti) 244	0.036(Ti) 244	0.052 223	0.048(Ti) 325	0.046(Ti) 312
(3) Interior Rings ^a W = 140 lb(38)		162(42)	172(39 Ti)	248(34)	273(37)	254(35 Ti)
(4) Base Ring ^b t = 0.037 in. R = 4.59 in. W = 85 lb		0.041 5.14 106	0.040 5.05 101	0.043 5.37 115	0.048 5.96 142	0.048 6.01 143
(5) Payload Ring W = 7 lb		10(Ti)	10(Ti)	12	19(Ti)	19(Ti)
(6) Heat Shield W = 116 lb		67	73	117	73	83
(7) Nonusable Entry Weight ^c W = 559 lb		628	640	760	890	866
(8) Total Entry Weight W = 4400		4400	4400	8800	8800	8800

^a Includes allowance for rivet weight.

^b Includes weight allowance for tube support.

^c Includes allowance for nose section.

TABLE V

OA.833 TENSION SHELL DESIGNS

	<u>(.32 slug/ft², 300^oF)</u>	<u>(.32, 550)</u>	<u>(.64, 300)</u>	<u>(.64, 550)</u>
(1) Stability Safety Factor				
$\lambda_{SF} = 2.13(2)$		2.40(2)	2.14(2)	2.27(2)
= 2.23(20)		2.69(20)	2.04(15)	2.27(16)
(2) Unstiffened Shell Aft of Payload Ring ^a				
t = 0.044 in.		0.036	0.062	0.052
W = 202 lb		269	274	369
(3) Interior Rings ^b				
W = 64(29)		100(31)	72(23)	96(25)
(4) 90(.5 x .75 x .1 x .016 in.) Full Length Stringers ^b				
W = 25		40	25	40
(5) Base Ring ^c				
t = 0.048 in.		0.042	0.068	0.055
R = 5.20 in.		4.62	6.07	5.50
W = 127 lb		157	210	242
(6) Payload Ring				
W = 7 lb		10	13	15
(7) Heat Shield				
W = 159 lb		124	168	130
(8) Nonusable Entry Weight ^d				
W = 605		728	790	929
(9) Total Entry Weight				
W = 5200 lb		5200	10 400	10 400

^a Includes weight allowance for ring-stringer fasteners.

^b Includes allowance for rivet weight.

^c Includes weight allowance for tube support.

^d Includes allowance for nose section.

TABLE VI.- COMPARISON OF SEVERAL MATERIALS

120° SANDWICH CONE

$$q_d = 400 \text{ psf}$$

$$2r_B = 15 \text{ ft}$$

$$r_P/r_B = .3$$

$$\rho_c = .03\rho_f$$

$$\text{Adhesive wt.} = .1 \text{ lb/ft}^2/\text{face sheet}$$

<u>Material</u>	<u>ρ (lb/in.³)</u>	<u>E (psi)</u>	<u>Base Ring</u>		<u>Shell</u>	
			<u>t*(in.)</u>	<u>W(lb)</u>	<u>t_f*(in.)</u>	<u>W(lb)</u>
Mg	.065	6.5×10^6	.035	52	.010	165
Al	.100	10.4	.025	57	.010	203
Ti	.158	17.0	.020	62	.008	255
St	.283	29.0	.016	78§	.005	358
B-epoxy (\$100/lb)	.0744	9.5¶	.027	45	.027	200§
Gr-epoxy(\$200/lb)	.055	6.5¶	.012	44	.012	146
S-glass epoxy	.0738	3.5¶	.020	94	.020	216

¶ Isotropic weave

§ Constrained by minimum gage

TABLE VII RING LOCATIONS & DIMENSIONS, IN.
 RING STIFFENED CONE - $T = 300^{\circ}\text{F}$, $\beta = 0.32 \text{ Slug/Ft}^2$
 ALUMINUM ALLOY

RING NO.	r	Δ	z	h	NEXT LARGEST STANDARD GAUGE
1	36.67	.2765	1.006	.0158	.016
2	39.10	.2318	1.207	.0183	.020
3	41.54	.2000	1.350	.0200	.020
4	43.96	.1757	1.459	.0212	.025
5	46.36	.1562	1.547	.0222	
6	48.71	.1359	1.639	.0231	
7	51.05	.1097	1.756	.0244	
8	53.38	.0875	1.856	.0254	.032
9	55.68	.0685	1.942	.0263	
10	57.95	.0519	2.017	.0270	
11	60.20	.0372	2.089	.0277	
12	62.42	.0234	2.143	.0283	
13	64.61	.0088	2.210	.0289	
14	66.78	.00	2.270	.0295	
15	68.93		2.325	.0301	
16	71.06		2.375	.0306	
17	73.16		2.422	.0310	
18	75.24		2.465	.0315	
19	77.30		2.496	.0318	
20	79.33		2.523	.0321	.040
21	81.35		2.548	.0324	
22	83.33		2.566	.0326	
23	85.30		2.573	.0327	
24	87.24		2.579	.0328	
25	89.16		2.585	.0330	
26	91.05		2.574	.0330	
27	92.92		2.557	.0329	
28	94.76		2.541	.0328	
29	96.58		2.525	.0327	
30	98.37		2.484	.0325	
31	100.1		2.442	.0322	
32	101.9		2.400	.0319	.032
33	103.6		2.353	.0315	
34	105.3	.0069	2.219	.0304	
35	106.9	.0398	2.071	.0291	
36	108.5	.0763	1.907	.0275	
37	110.0	.1181	1.719	.0256	
38	111.5	.1690	1.489	.0231	.025

TABLE VIII RING LOCATIONS & DIMENSIONS, IN.
RING STIFFENED CONE, $T = 300^{\circ}\text{F}$, $\beta = 0.64 \text{ Slug/Ft}^2$
ALUMINUM ALLOY

RING NO.	r	Δ	ℓ	h	NEXT LARGEST STANDARD GAUGE
1	37.08	.1569	1.544	.0291	.032
2	39.92	.1205	1.848	.0332	.040
3	42.81	.1167	2.076	.0361	
4	45.68	.1104	2.241	.0380	
5	48.50	.1041	2.359	.0393	
6	51.25	.0978	2.451	.0402	.051
7	53.93	.0919	2.539	.0410	
8	56.54	.0873	2.601	.0416	
9	59.08	.0830	2.655	.0421	
10	61.56	.0792	2.708	.0426	
11	63.99	.0761	2.758	.0431	
12	66.38	.0727	2.812	.0436	
13	68.72	.0702	2.861	.0441	
14	71.02	.0675	2.905	.0446	
15	73.28	.0657	2.942	.0450	
16	75.51	.0645	2.971	.0453	
17	77.71	.0628	3.008	.0457	
18	79.87	.0611	3.048	.0462	
19	82.01	.0608	3.069	.0464	
20	84.11	.0608	3.086	.0467	
21	86.19	.0597	3.116	.0470	
22	88.24	.0605	3.125	.0472	
23	90.27	.0610	3.136	.0474	
24	92.27	.0608	3.158	.0477	
25	94.25	.0635	3.144	.0476	
26	96.20	.0661	3.126	.0476	
27	98.12	.0681	3.116	.0475	
28	100.0	.0711	3.093	.0474	
29	101.9	.0744	3.067	.0472	
30	103.7	.0779	3.036	.0470	
31	105.6	.0813	3.008	.0469	
32	107.4	.0844	2.982	.0467	
33	109.1	.0903	2.918	.0462	
34	110.9	.1060	2.698	.0441	

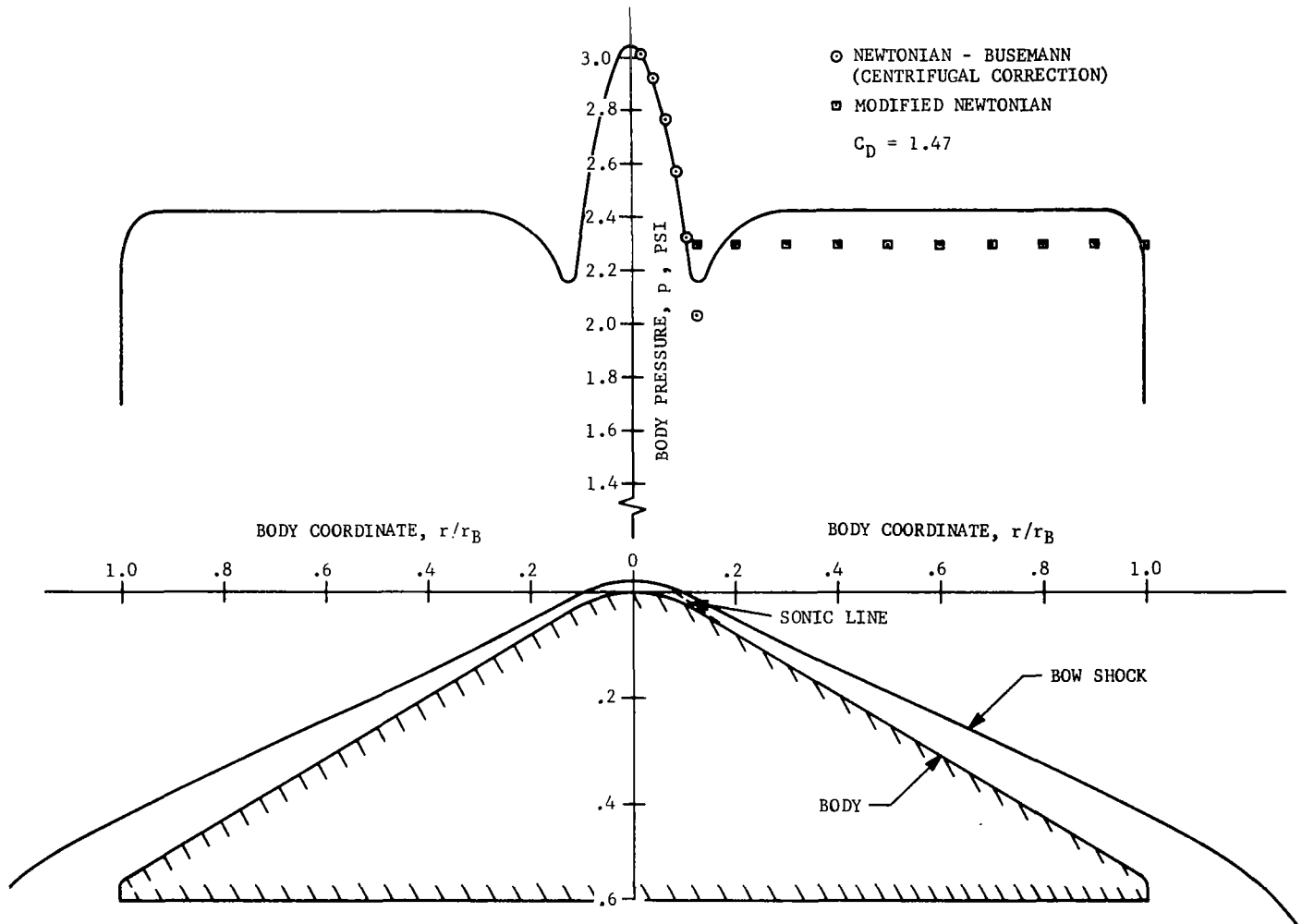
TABLE IX RING LOCATIONS & DIMENSIONS, IN.
 OA.833 Tension Shell, T = 300°F, $\beta = 0.32$ Slug/Ft²
 ALUMINUM ALLOY

RING NO.	r	Δ	ℓ	h	NEXT LARGEST STANDARD GAUGE
1	47.45	.1838	1.423	.0191	.020
2	56.49	.2000	1.350	.0178	
3	63.09	.2096	1.307	.0174	
4	68.41	.2180	1.269	.0172	
5	72.64	.2345	1.195	.0172	
6	76.03	.2515	1.118	.0170	
7	78.89	.2596	1.082	.0173	
8	81.42	.2634	1.065	.0177	
9	83.70	.2646	1.059	.0184	
10	85.77	.2646	1.059	.0191	
11	87.72	.2618	1.072	.0195	
12	89.63	.2563	1.097	.0199	
13	91.51	.2525	1.114	.0203	.025
14	93.36	.2517	1.117	.0205	
15	95.14	.2562	1.097	.0207	
16	96.83	.2644	1.060	.0207	
17	98.41	.2757	1.010	.0205	
18	99.89	.2883	.953	.0201	
19	101.3	.3013	.894	.0197	.020
20	102.6	.3148	.833	.0192	
21	103.8	.3239	.792	.0192	
22	105.0	.3284	.772	.0195	
23	106.0	.3317	.757	.0198	
24	107.1	.3323	.755	.0199	
25	108.1	.3330	.751	.0201	.025
26	109.1	.3367	.735	.0202	
27	110.1	.2777	1.000	.0258	.032
28	111.1	.2969	.914	.0245	.025
29	112.1	.2532	1.111	.0283	.032

TABLE X RING LOCATIONS & DIMENSIONS, IN.
 OA.833 Tension Shell, T = 300°F, $\beta = 0.64$ Slug/Ft²
 ALUMINUM ALLOY

RING NO.	r	Δ	l	h	NEXT LARGEST STANDARD GAUGE
1	58.21	.0043	2.302	.0323	.040
2	71.83	.0491	2.029	.0310	.032
3	76.05	.1657	1.504	.0253	
4	79.07	.1890	1.400	.0260	
5	81.48	.2025	1.339	.0272	
6	83.56	.2091	1.309	.0286	
7	85.42	.2135	1.289	.0300	
8	87.12	.2137	1.288	.0301	
9	88.91	.2001	1.349	.0297	
10	90.84	.1899	1.396	.0305	
11	92.71	.1910	1.391	.0310	
12	94.53	.1942	1.376	.0309	
13	96.57	.2090	1.378	.0322	.040
14	98.48	.2189	1.306	.0318	.032
15	100.3	.2300	1.215	.0311	
16	101.9	.2514	1.119	.0303	
17	103.4	.2707	1.032	.0295	
18	104.8	.2721	1.026	.0299	
19	106.2	.2734	1.020	.0306	
20	107.5	.2764	1.006	.0312	
21	108.7	.2909	.978	.0318	
22	109.9	.3050	.938	.0321	.040
23	111.0	.3233	.889	.0326	

FIGURE 1. BODY PRESSURE DISTRIBUTION AND BOW SHOCK POSITION FOR A
 120° CONE ($R_N/r_B = .25$)



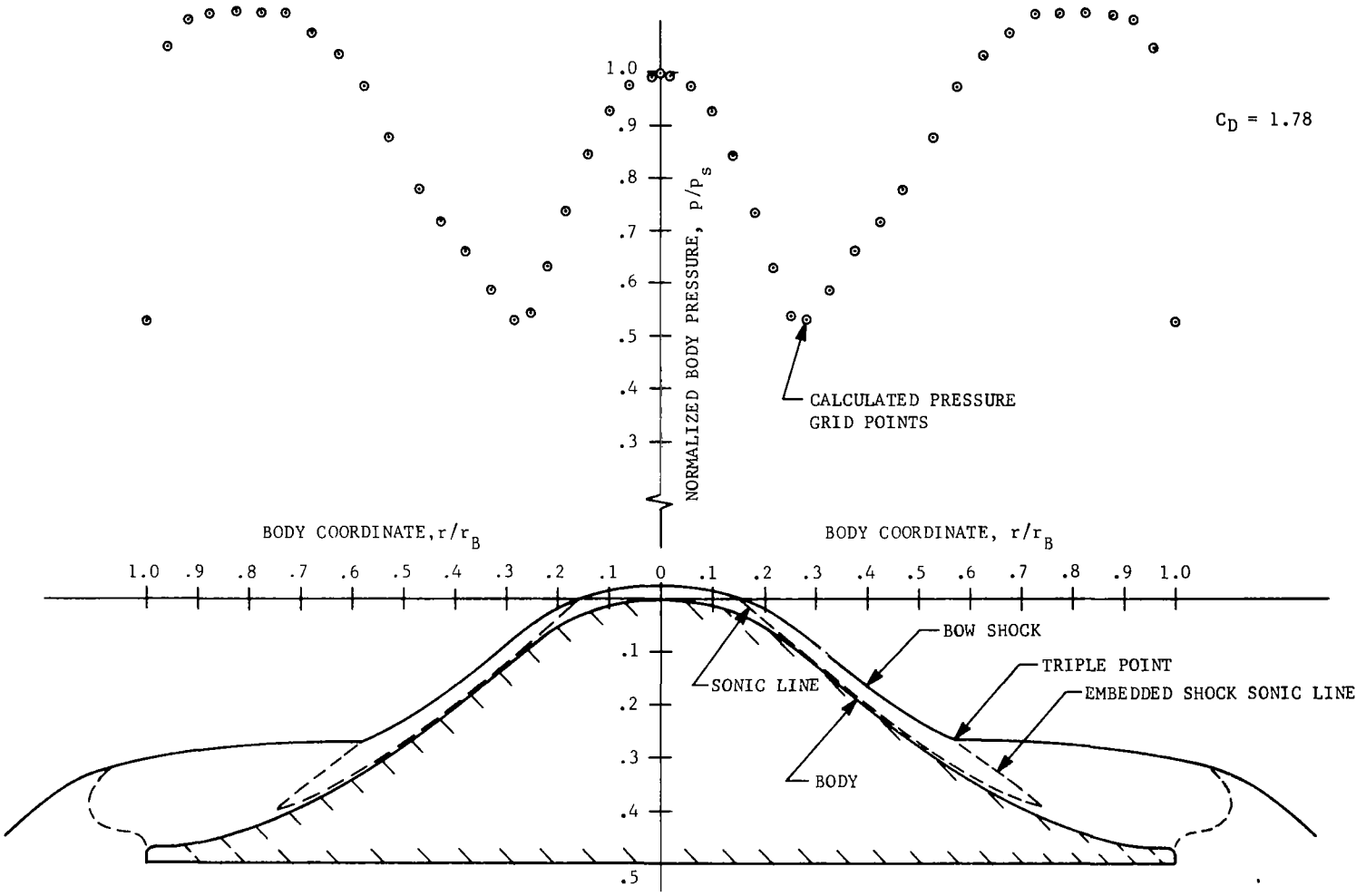


FIGURE 2. BODY PRESSURE DISTRIBUTION AND BOW SHOCK POSITION FOR THE 0A.833 TENSION SHELL ($R_N/r_B = .4$)

FIGURE 3. BODY PRESSURE DISTRIBUTION AND BOW SHOCK POSITION FOR THE OA.833 TENSION SHELL ($R_N/r_B = .4$) AT 12 DEGREES ANGLE OF ATTACK.

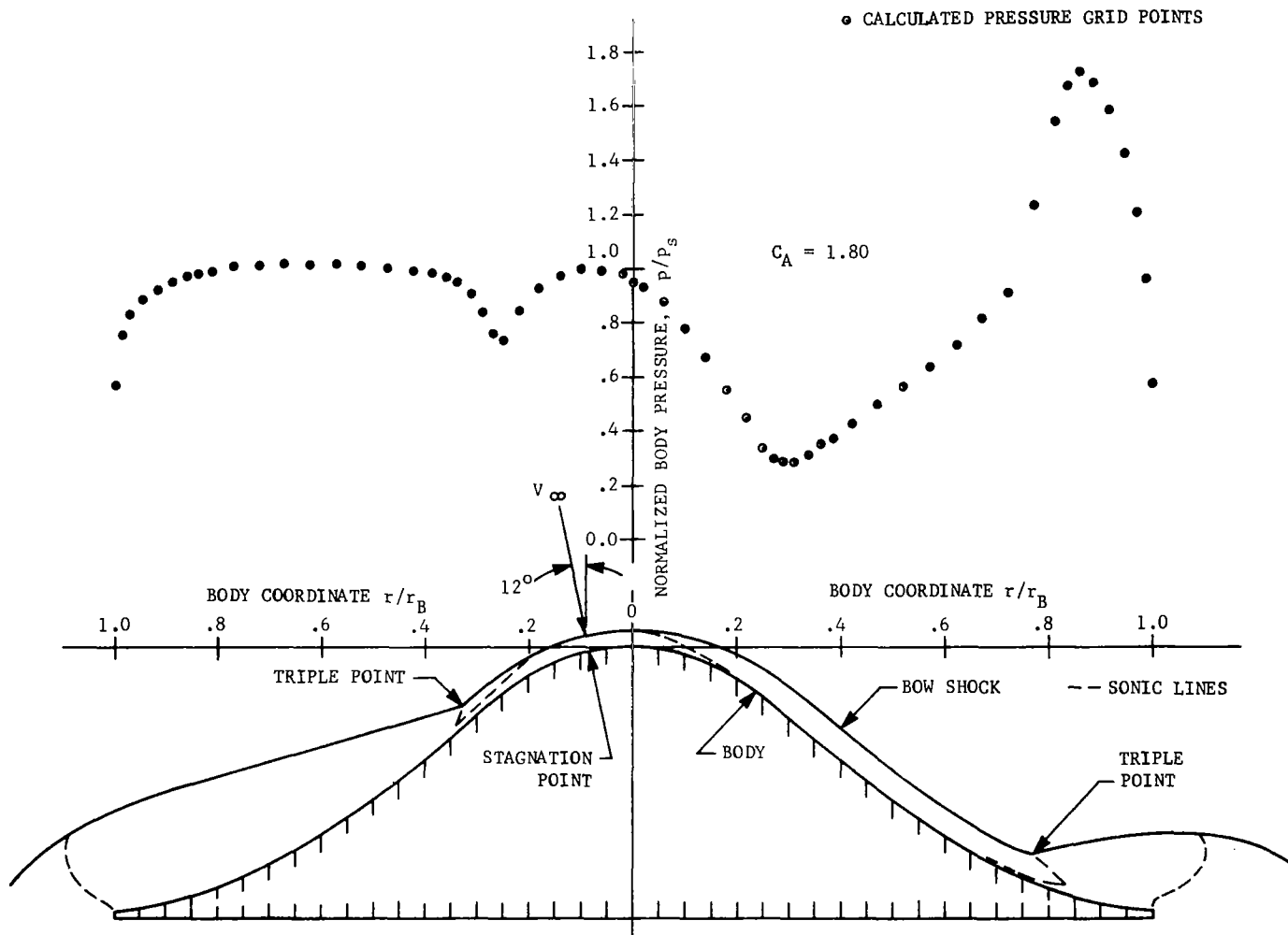


FIGURE 4. BODY PRESSURE DISTRIBUTION AND BOW SHOCK POSITION FOR THE OA.65 TENSION SHELL ($R_N/r_B = .3$)

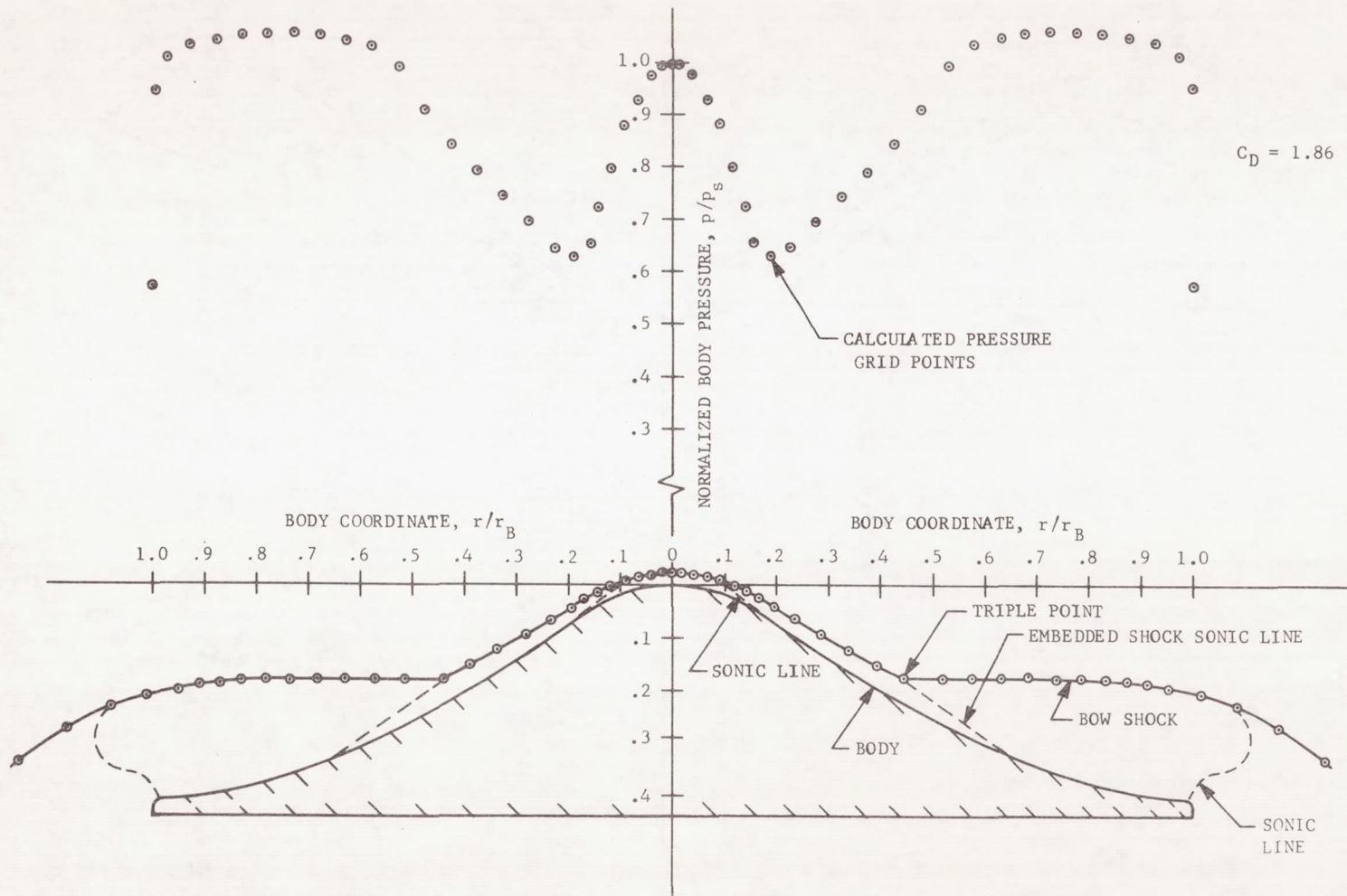


FIGURE 4. BODY PRESSURE DISTRIBUTION AND BOW SHOCK POSITION FOR THE OA.65 TENSION SHELL ($R_N/r_B = .3$)

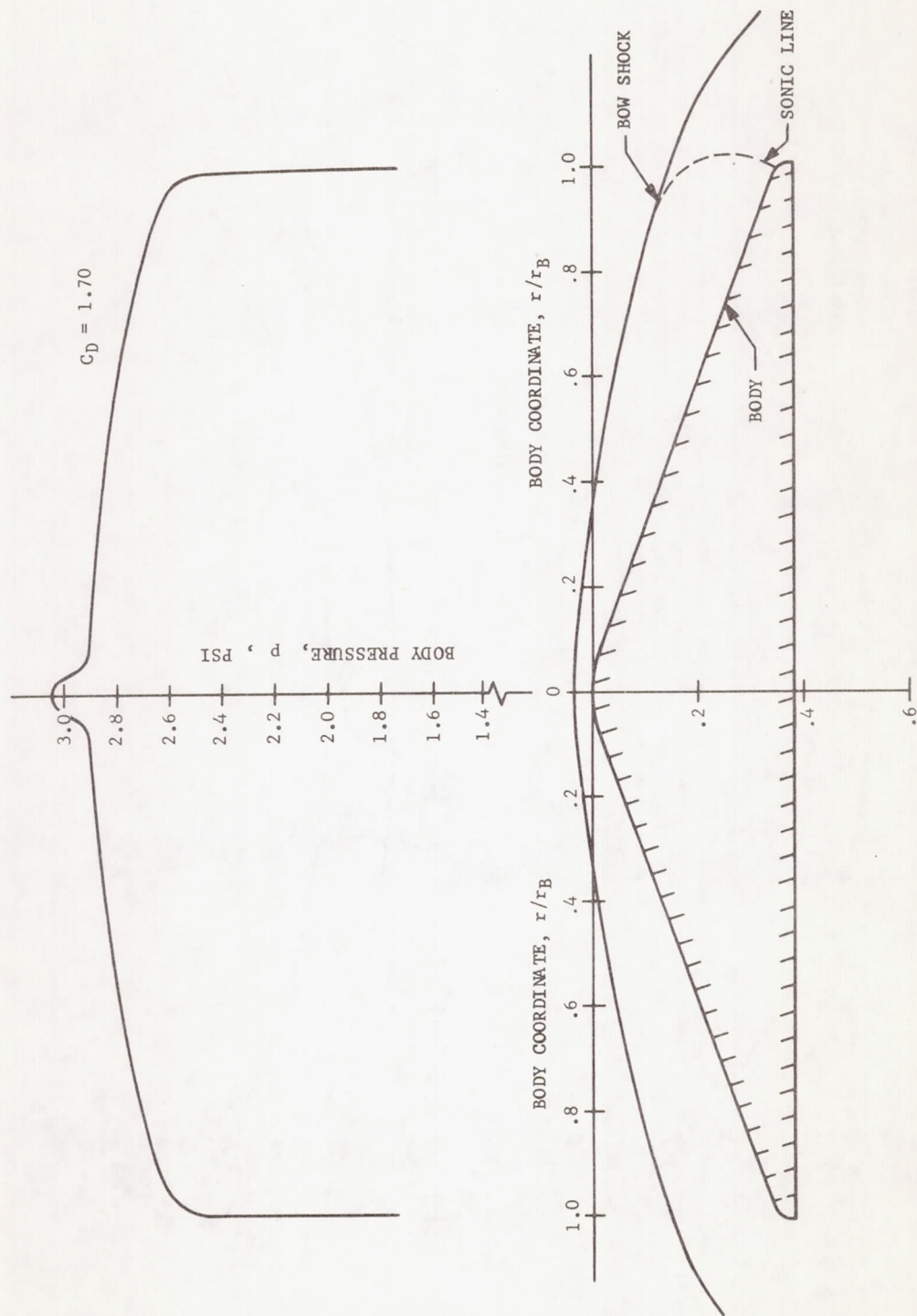
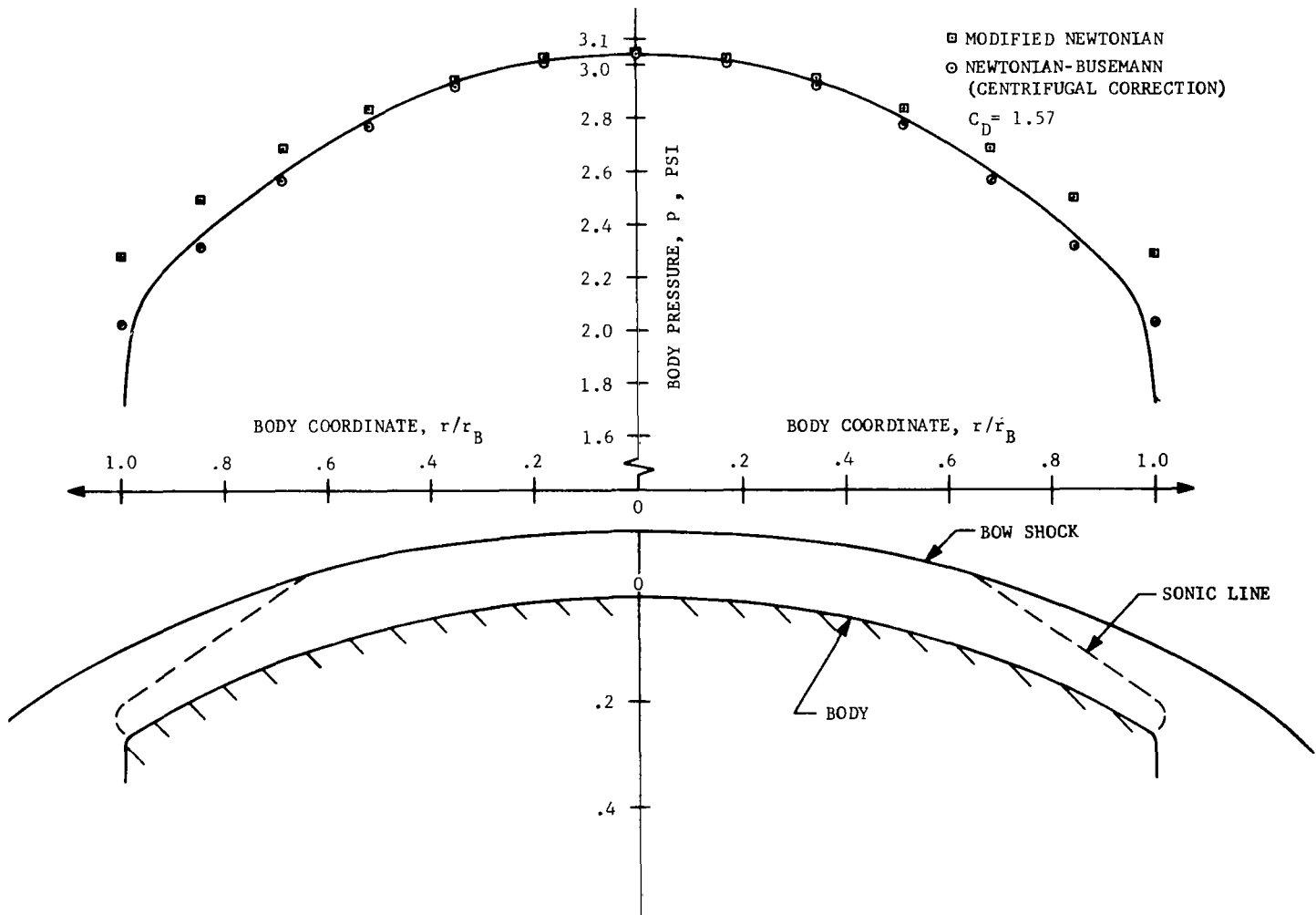


FIGURE 5. BODY PRESSURE DISTRIBUTION AND BOW SHOCK POSITION FOR A 140° CONE ($R_N/r_B = .25$)

FIGURE 6. BODY PRESSURE DISTRIBUTION AND BOW SHOCK POSITION FOR A SPHERICAL DISH ($R_N/r_B = 2.0$)



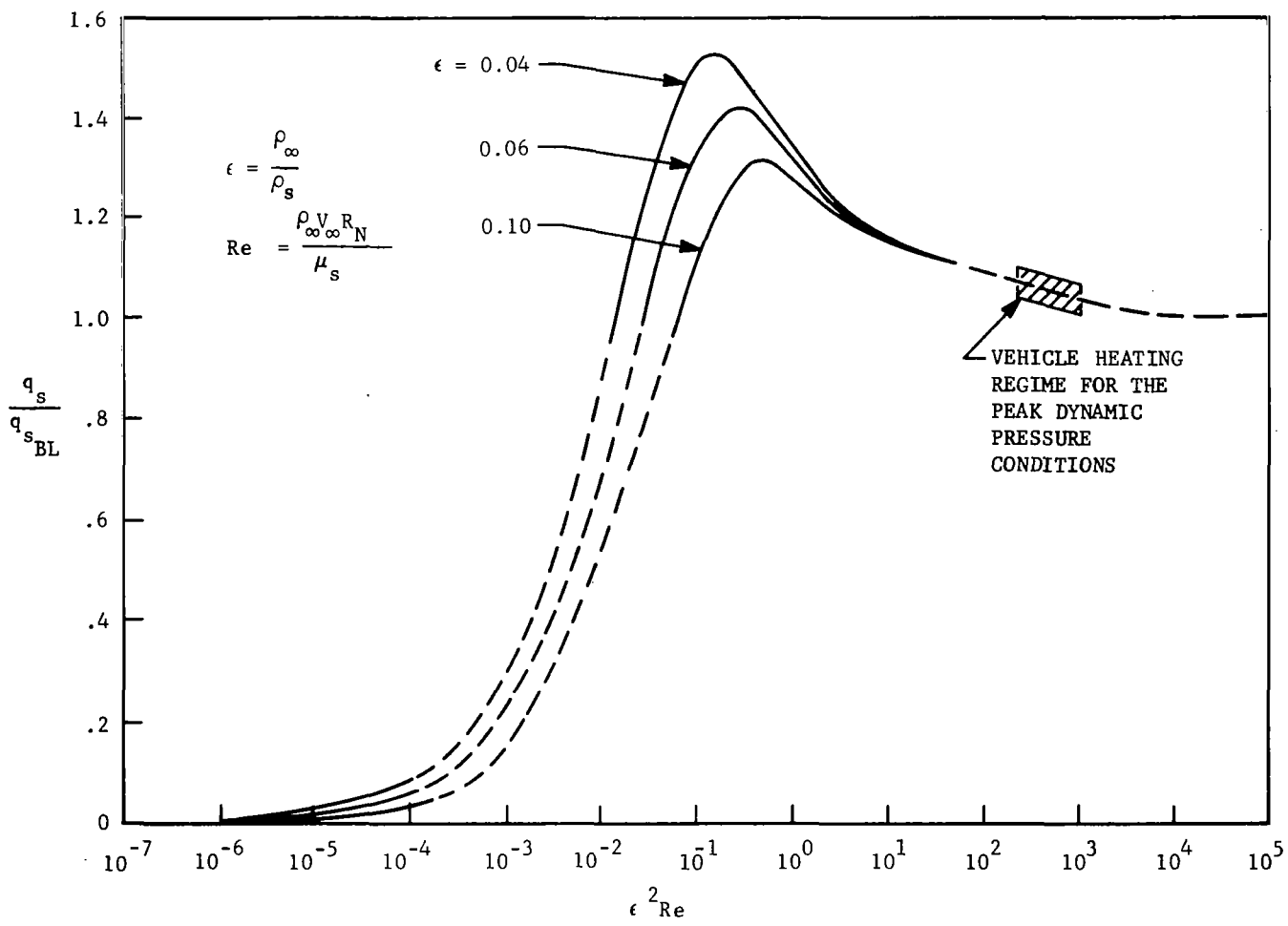


FIGURE 7. COMPARISON OF LOW REYNOLDS NUMBER AND CLASSICAL BOUNDARY LAYER THEORY STAGNATION POINT HEAT TRANSFER (REF. 10)

FIGURE 8. CONVECTIVE HEAT TRANSFER DISTRIBUTION FOR THE 120° AND 140° SPHERE-CONE AND THE SPHERICAL DISH CAPSULE CONFIGURATIONS

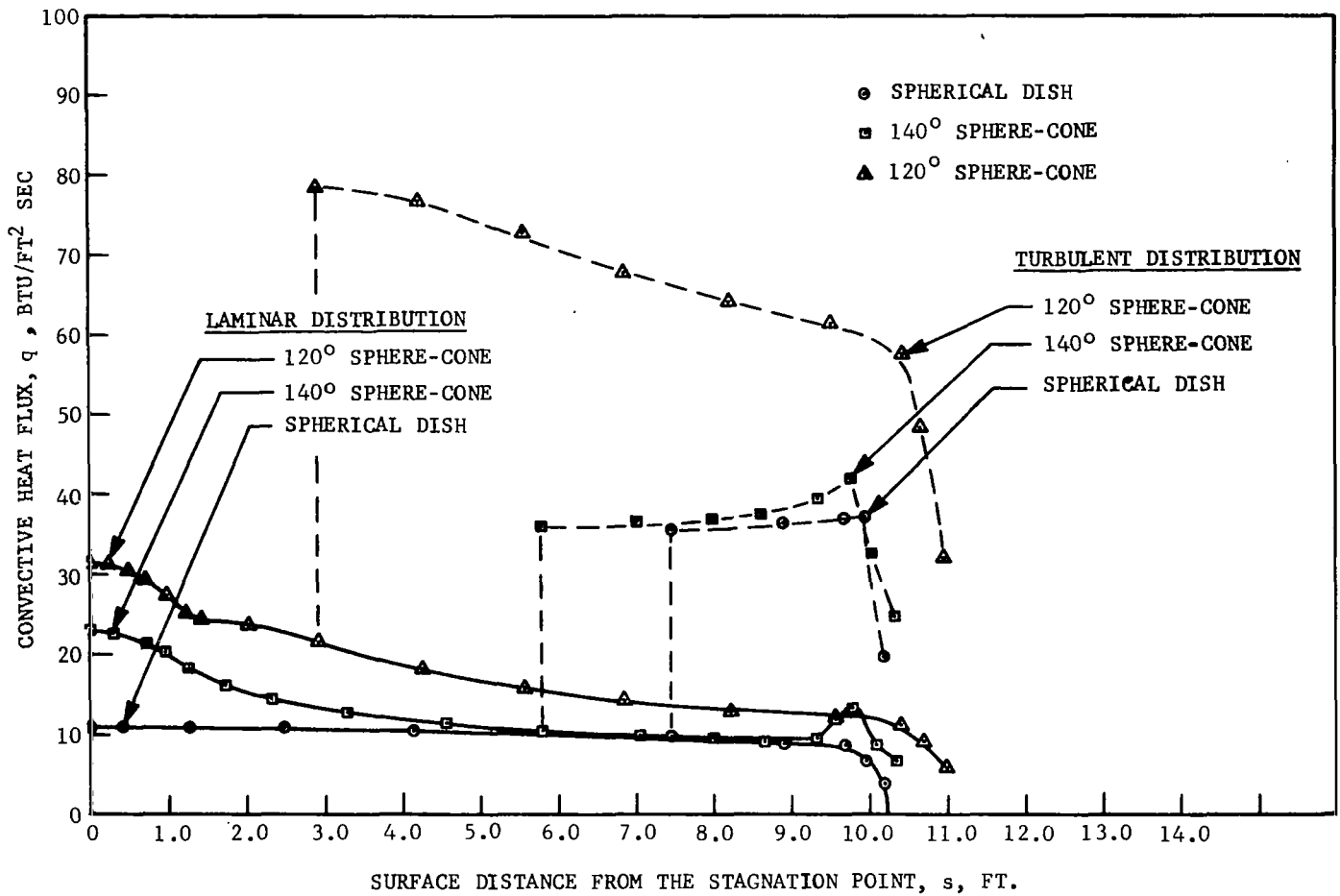


FIGURE 9. CONVECTIVE HEAT TRANSFER DISTRIBUTION FOR THE OA.65 AND OA.833 TENSION SHELL CAPSULE CONFIGURATIONS.

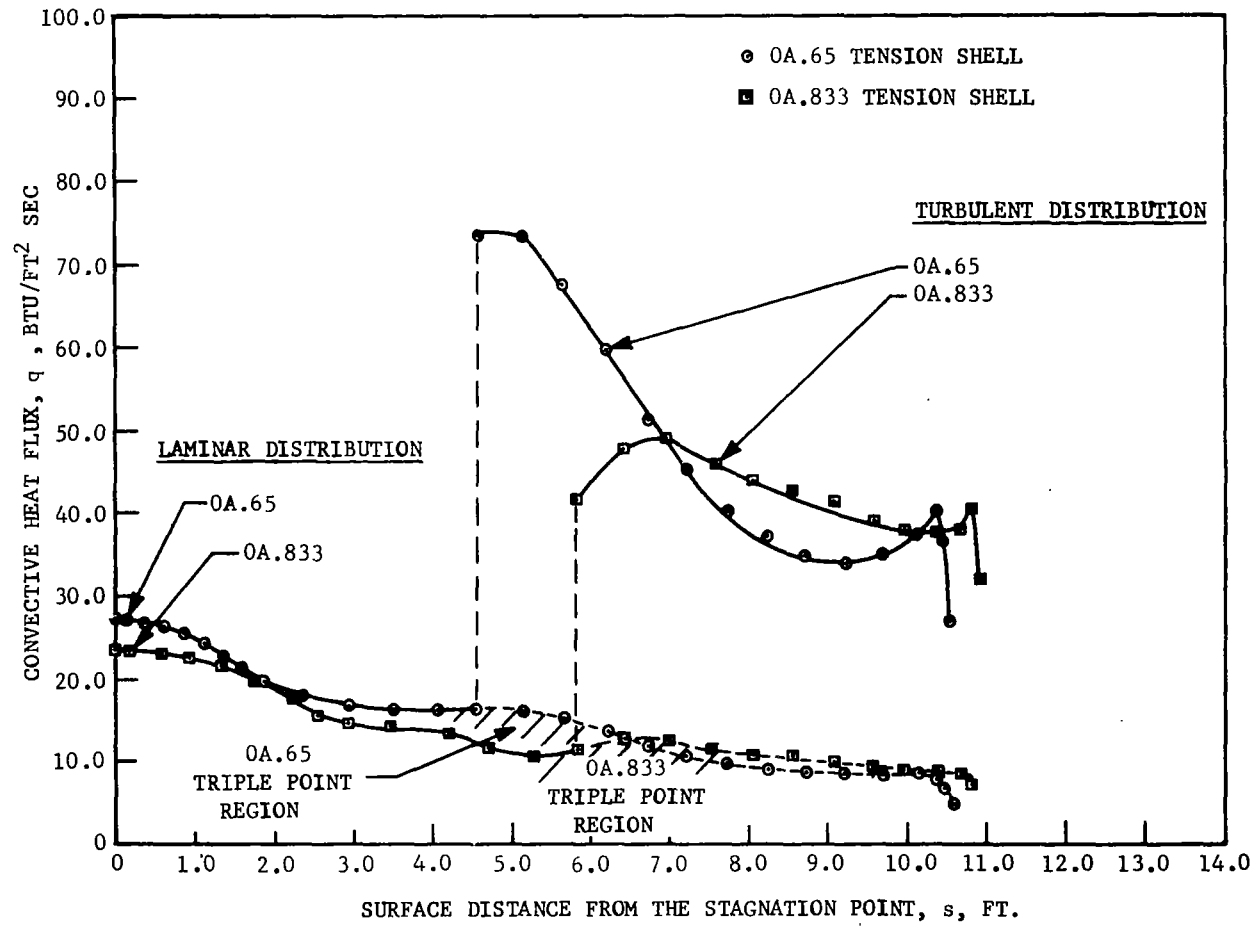


FIGURE 10. OPTIMUM DESIGN FLOW CHART

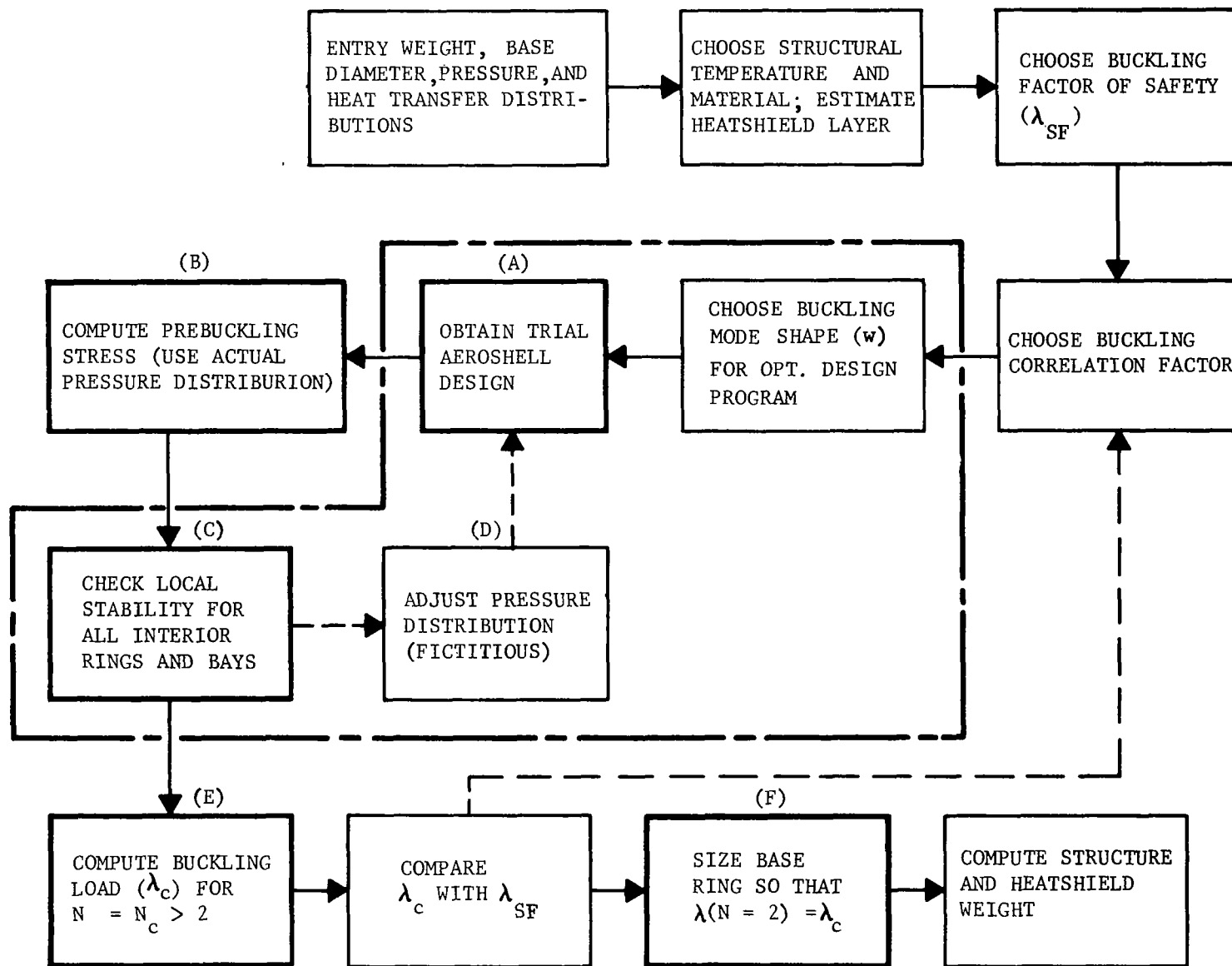
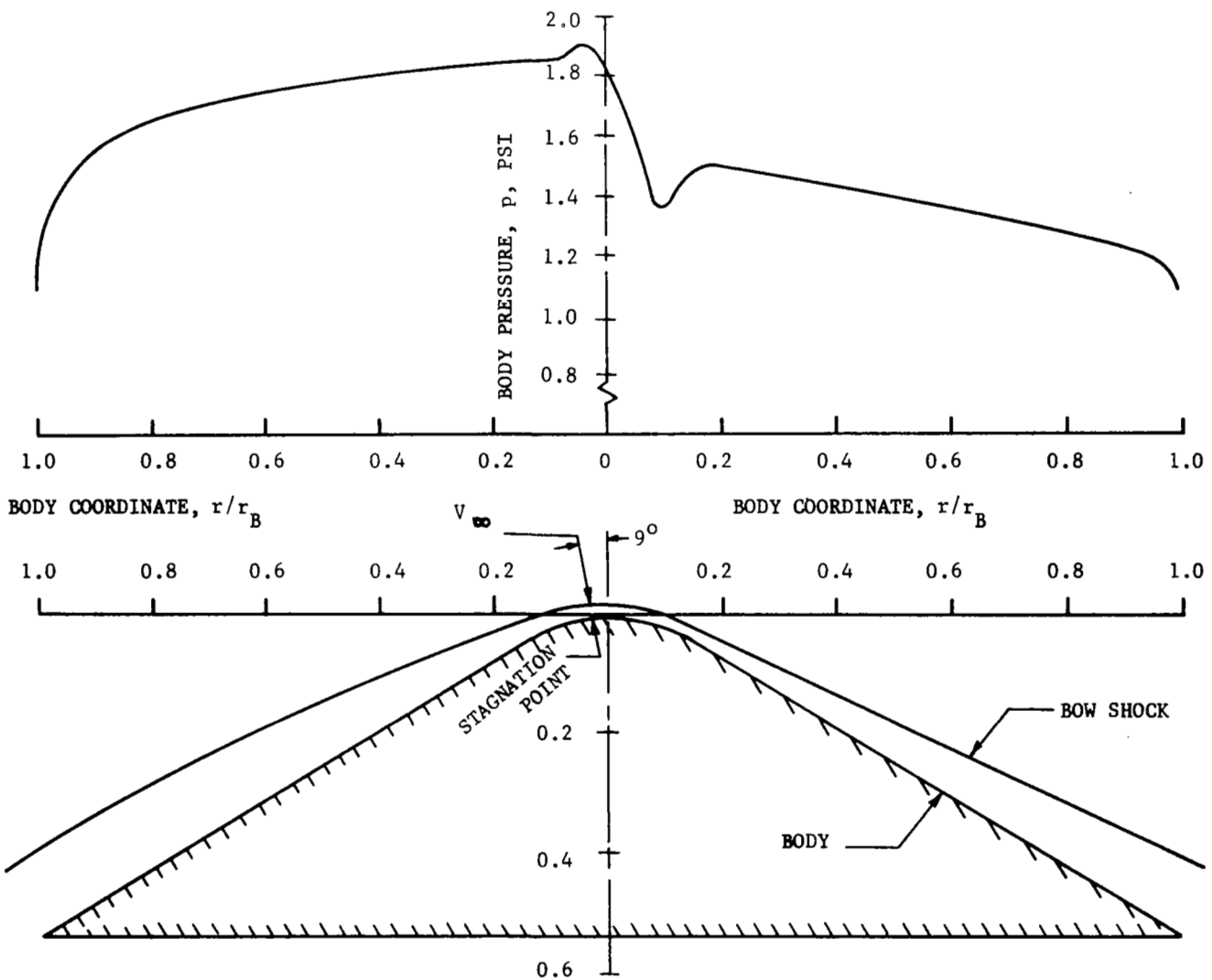


FIGURE 11. BODY PRESSURE DISTRIBUTION AND BOW SHOCK POSITION FOR A 120° CONE ($R_N/r_B = 0.25$) AT 9 DEGREES ANGLE OF ATTACK. [FROM REF. 2]



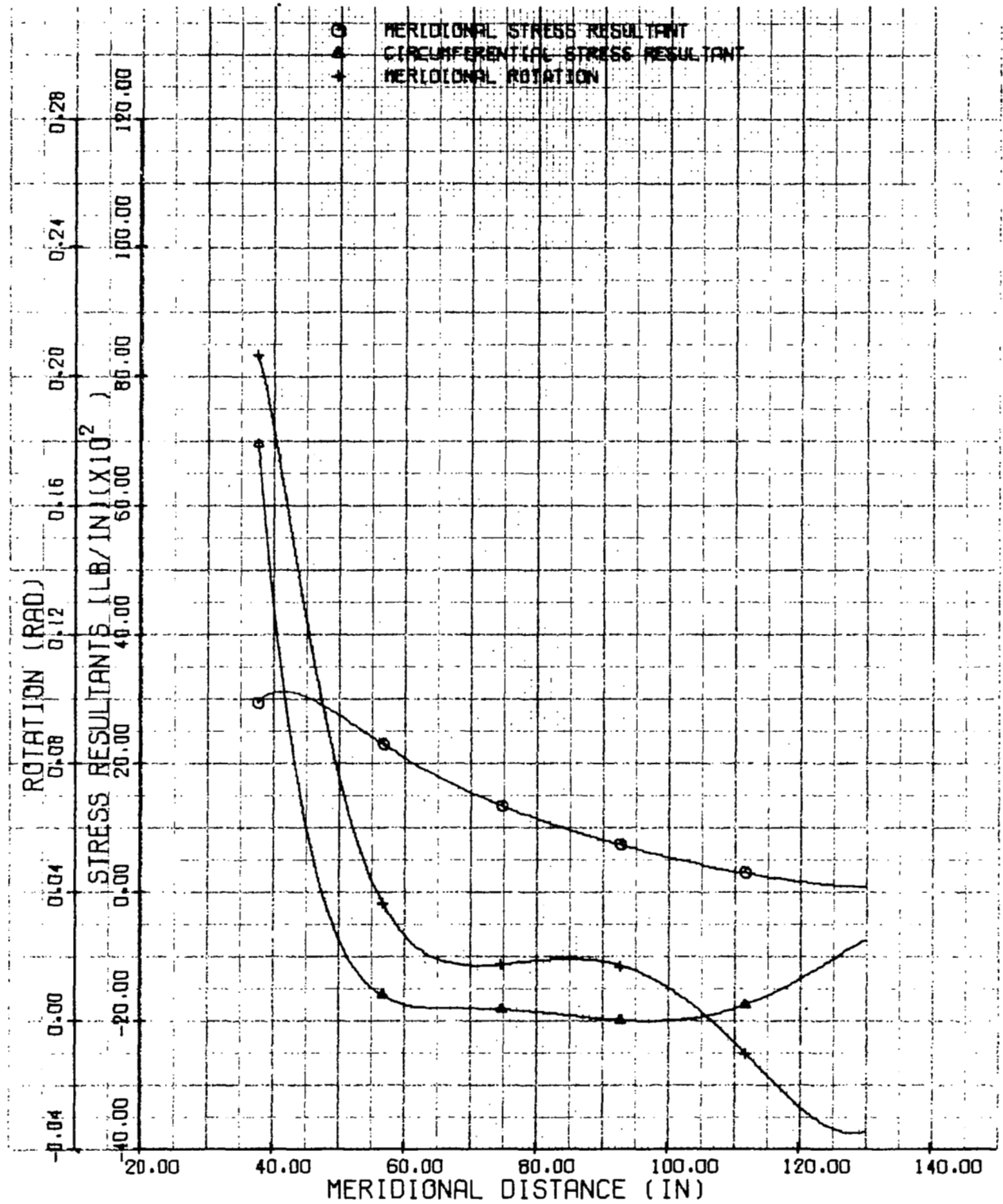


FIGURE 12. PREBUCKLING STRESS RESULTANTS AND ROTATION, 120° SANDWICH CONE (0.64 Slug/Ft², 300°F) S.F. = 2.25

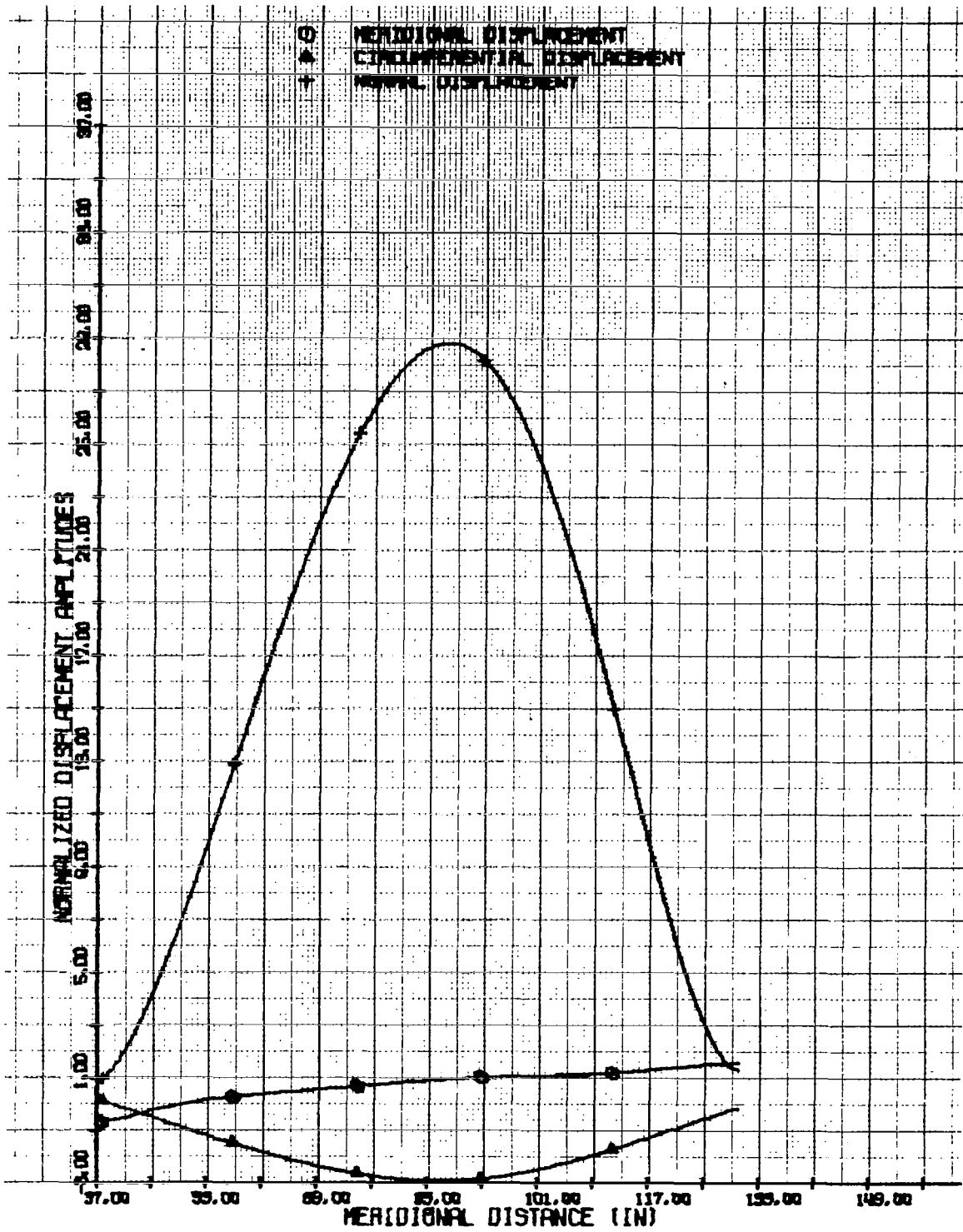


FIGURE 13. BUCKLING MODE DISPLACEMENTS, 120° SANDWICH CONE
 (0.64 Slug/Ft², 300°F) N = 5, S.F. = 2.10

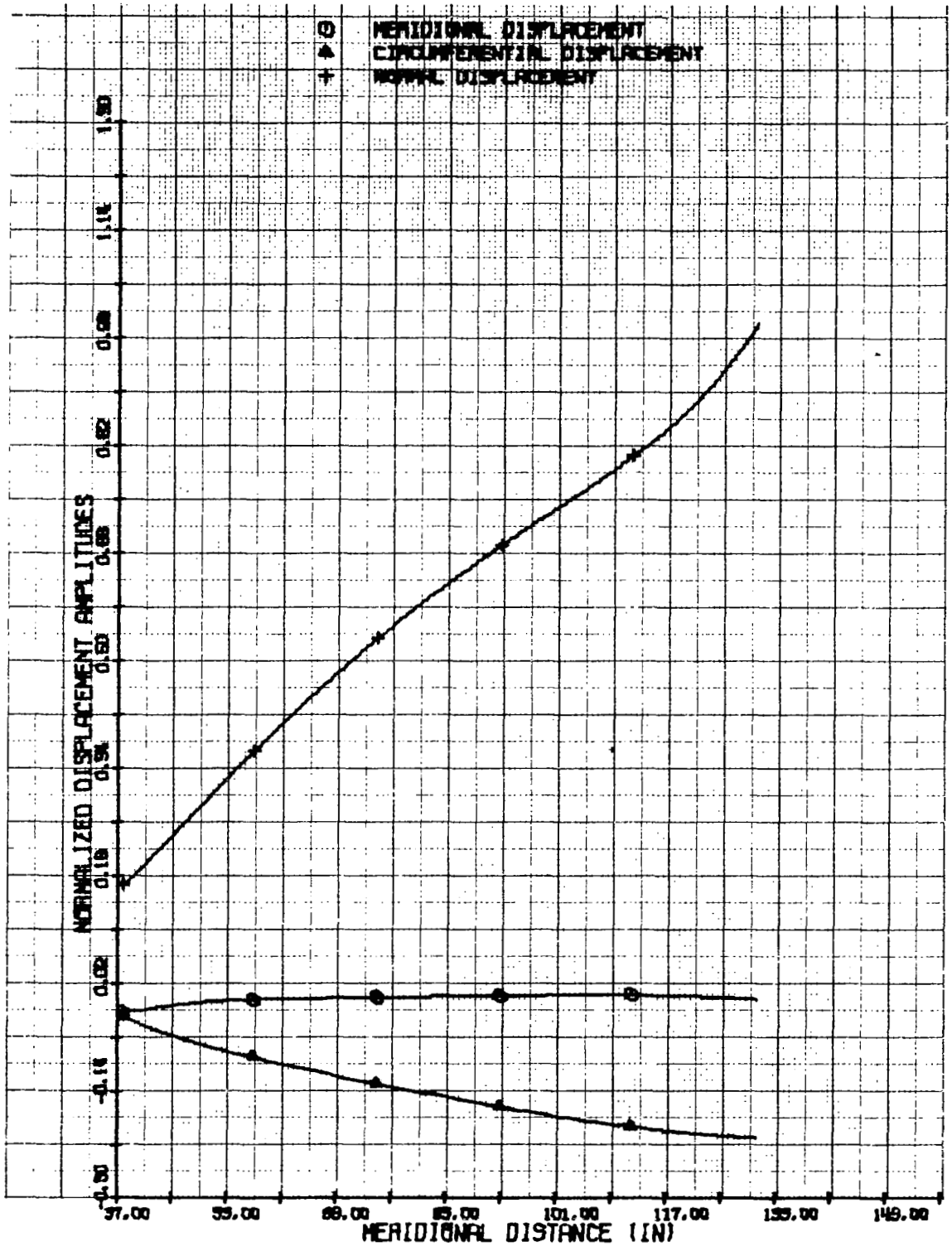


FIGURE 14. BUCKLING MODE DISPLACEMENTS, 120° SANDWICH CONE
 (0.64 Slug/Ft², 300°F) N = 2, S.F. = 2.06

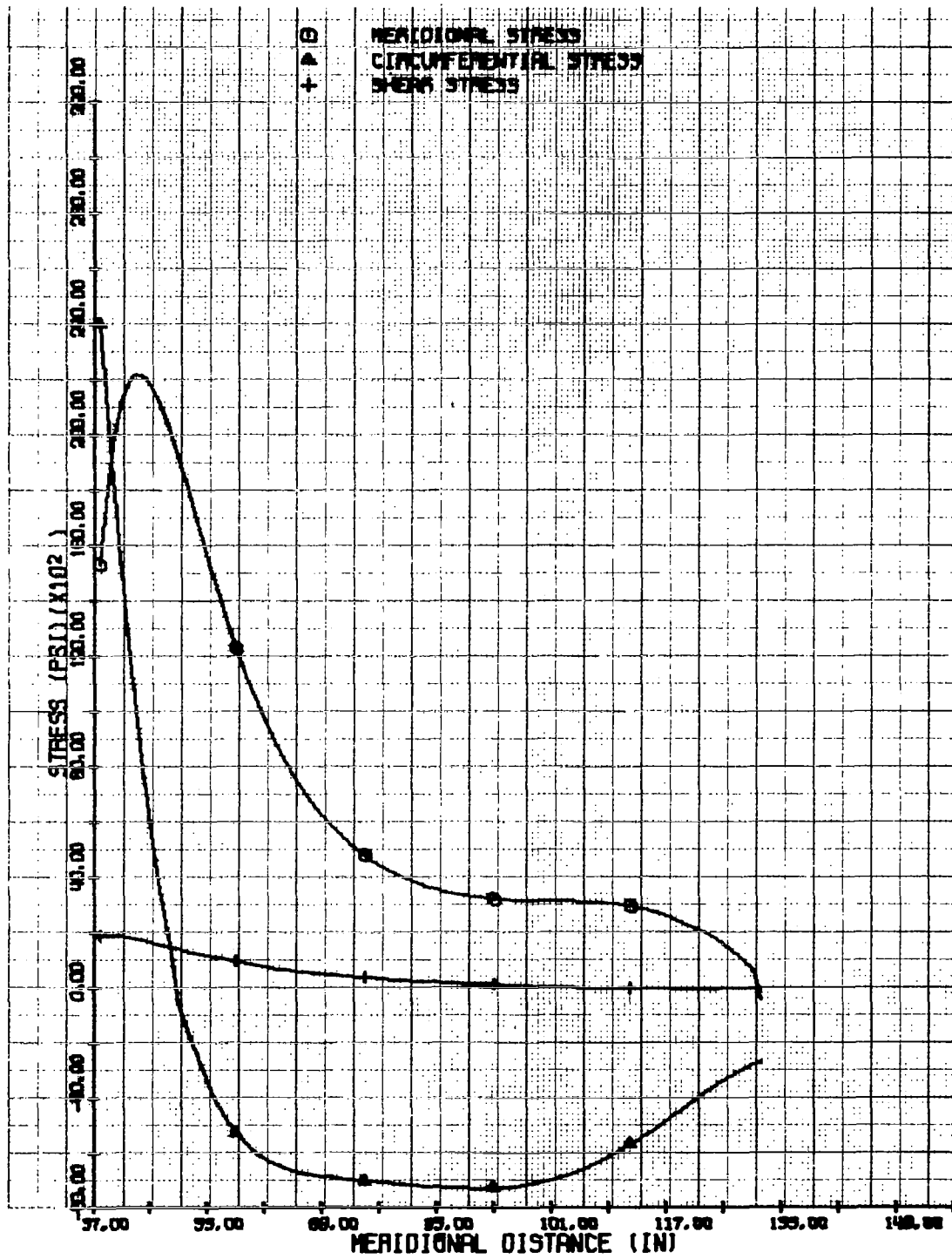


FIGURE 15. MAXIMUM SHELL STRESSES, 120° SANDWICH CONE (0.64 Slug/Ft², 300°F)
 LAYER NO. 1 (INNER FACE) S.F. = 0.3125

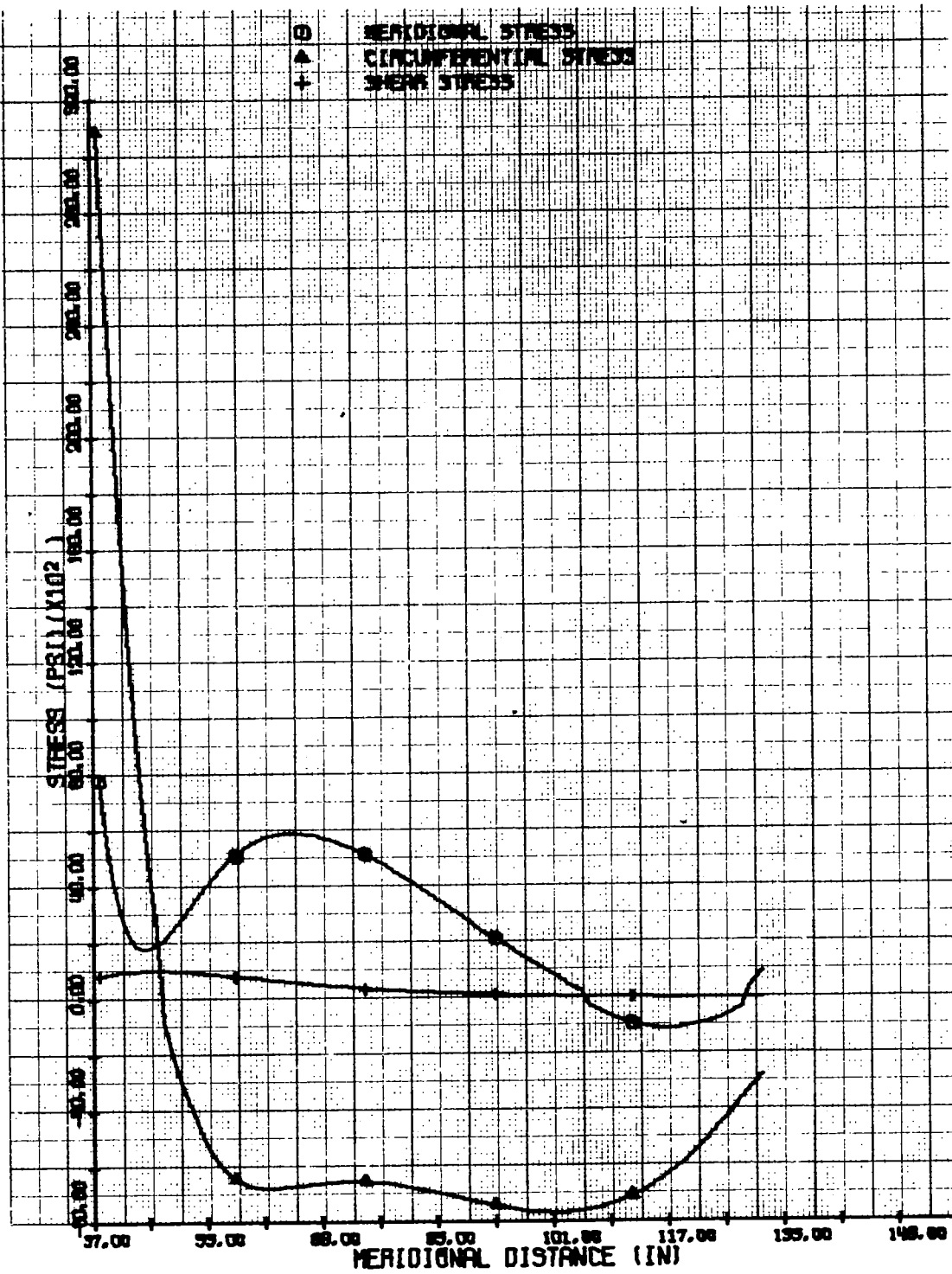


FIGURE 16. MAXIMUM SHELL STRESSES, 120° SANDWICH CONE (0.64 Slug/Ft², 300°F)
 LAYER NO. 3 (OUTER FACE) S.F. = 0.3125

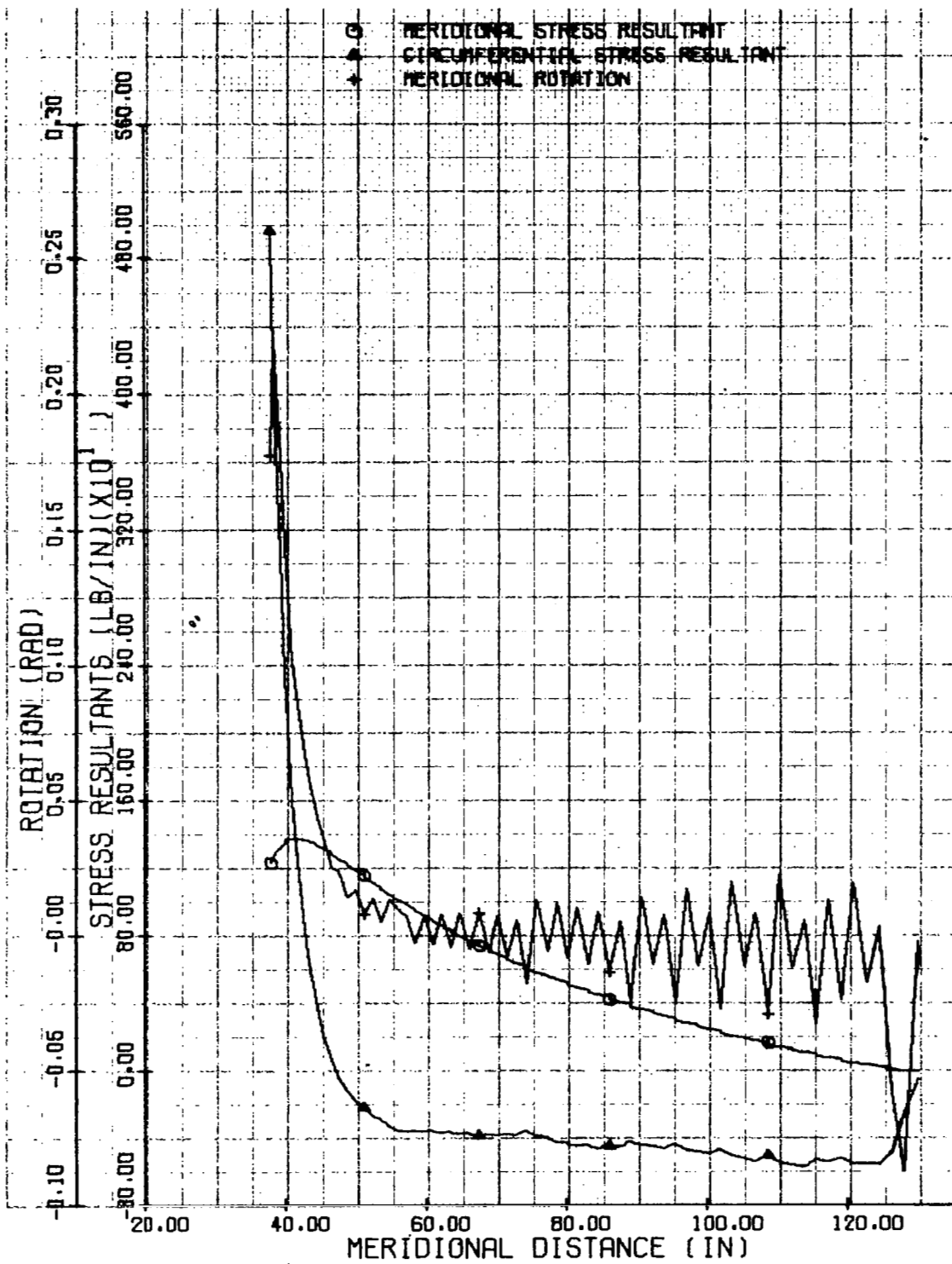


FIGURE 17. PREBUCKLING STRESS RESULTANTS AND ROTATION, 120° RING STIFFENED CONE (0.32 Slug/Ft², 300°F) S.F. = 2.25

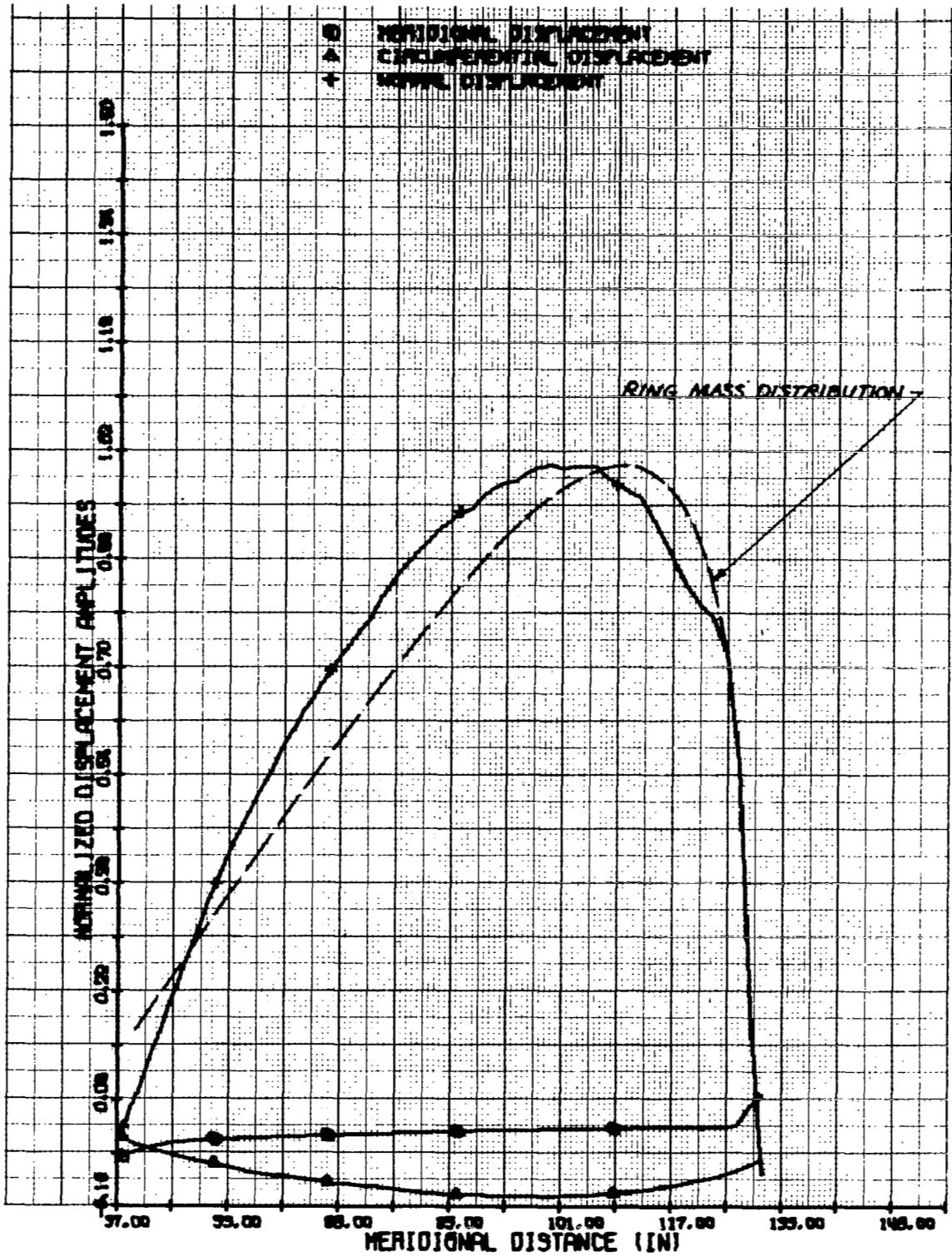


FIGURE 18. BUCKLING MODE DISPLACEMENTS, 120° RING STIFFENED CONE
 (0.32 Slug/Ft², 300°F) N = 5, S.F. = 2.16

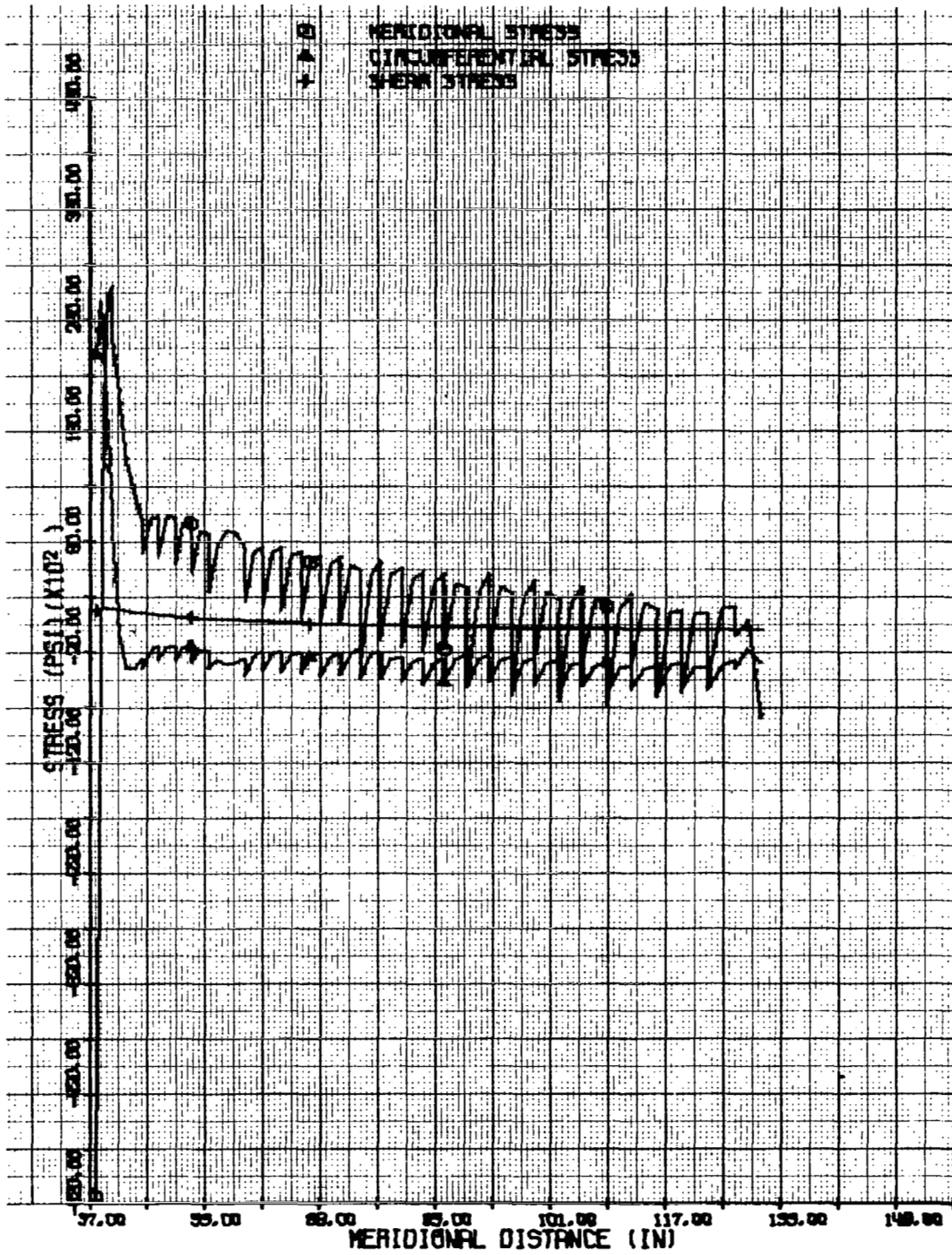


FIGURE 19. MAXIMUM SHELL STRESSES, 120° RING STIFFENED CONE
 (0.32 Slug/Ft², 300°F) LAYER NO. 1 (INNER FACE) S.F. = 0.625

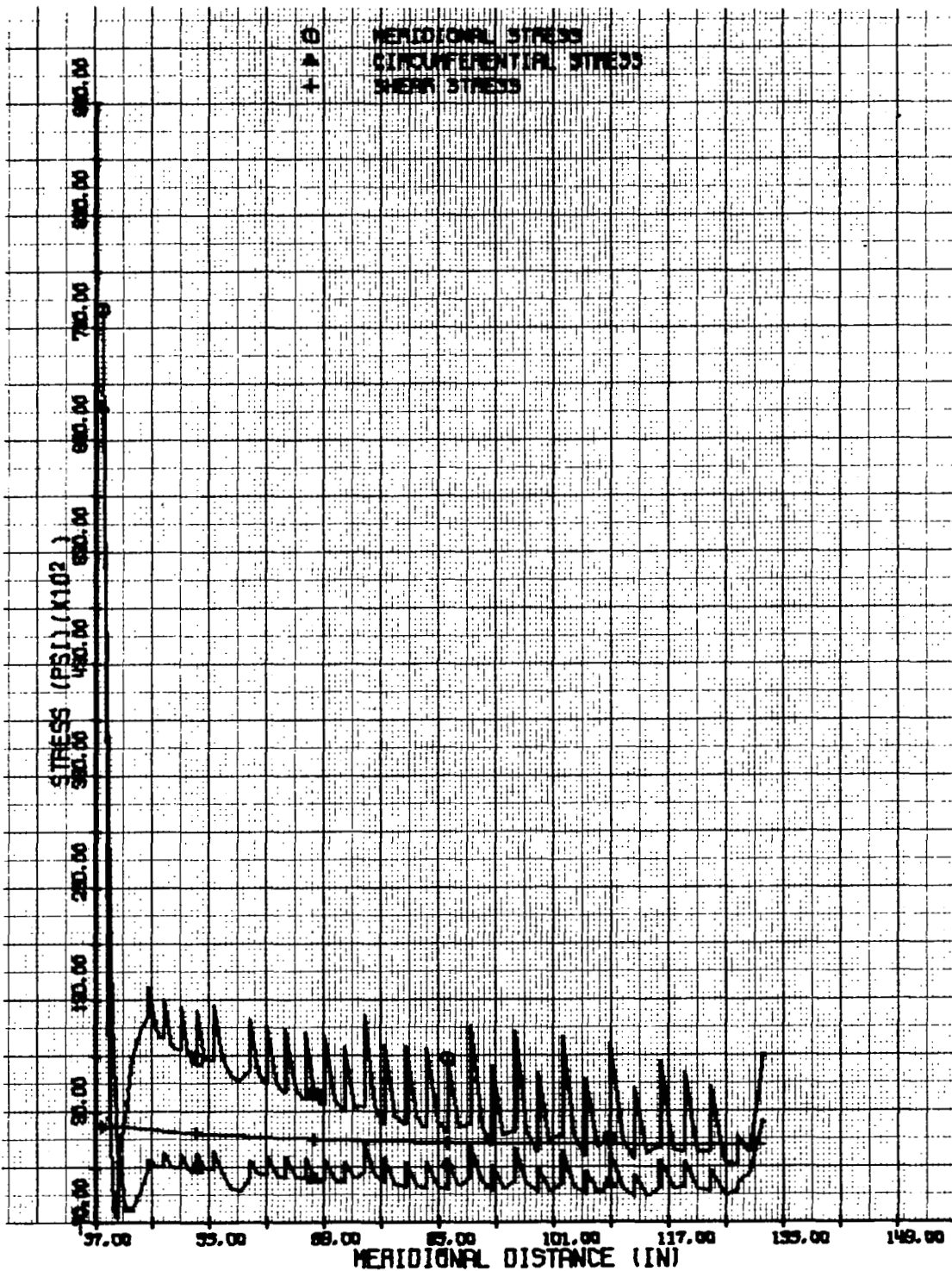


FIGURE 20. MAXIMUM SHELL STRESSES, 120° RING STIFFENED CONE
 (0.32 Slug/Ft², 300°F) LAYER NO. 1 (OUTER FACE) S.F. = 0.625

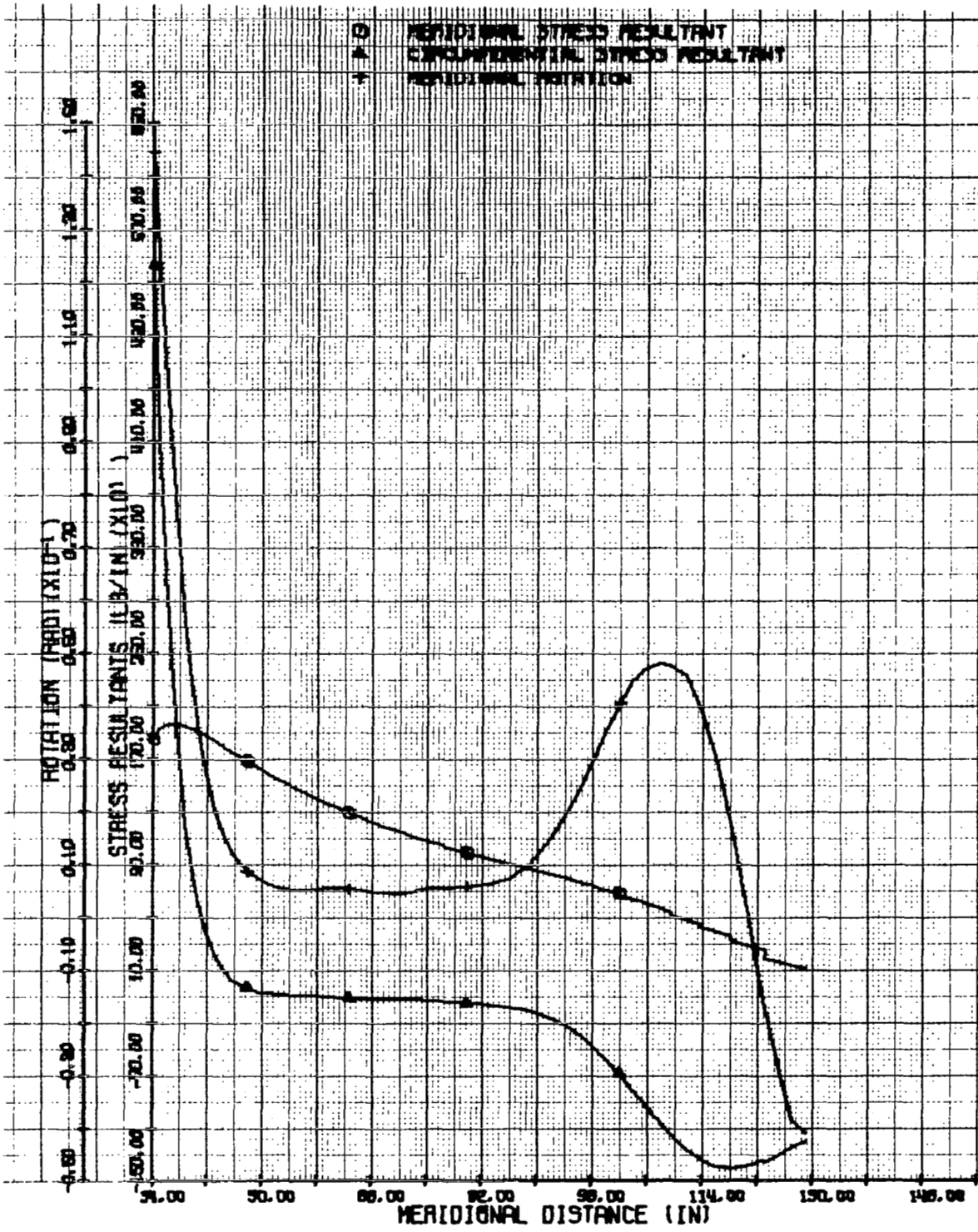


FIGURE 21. PREBUCKLING STRESS RESULTANTS AND ROTATION, OA.833 TENSION SHELL (0.32 Slug/Ft², 300°F) S.F. = 2.25

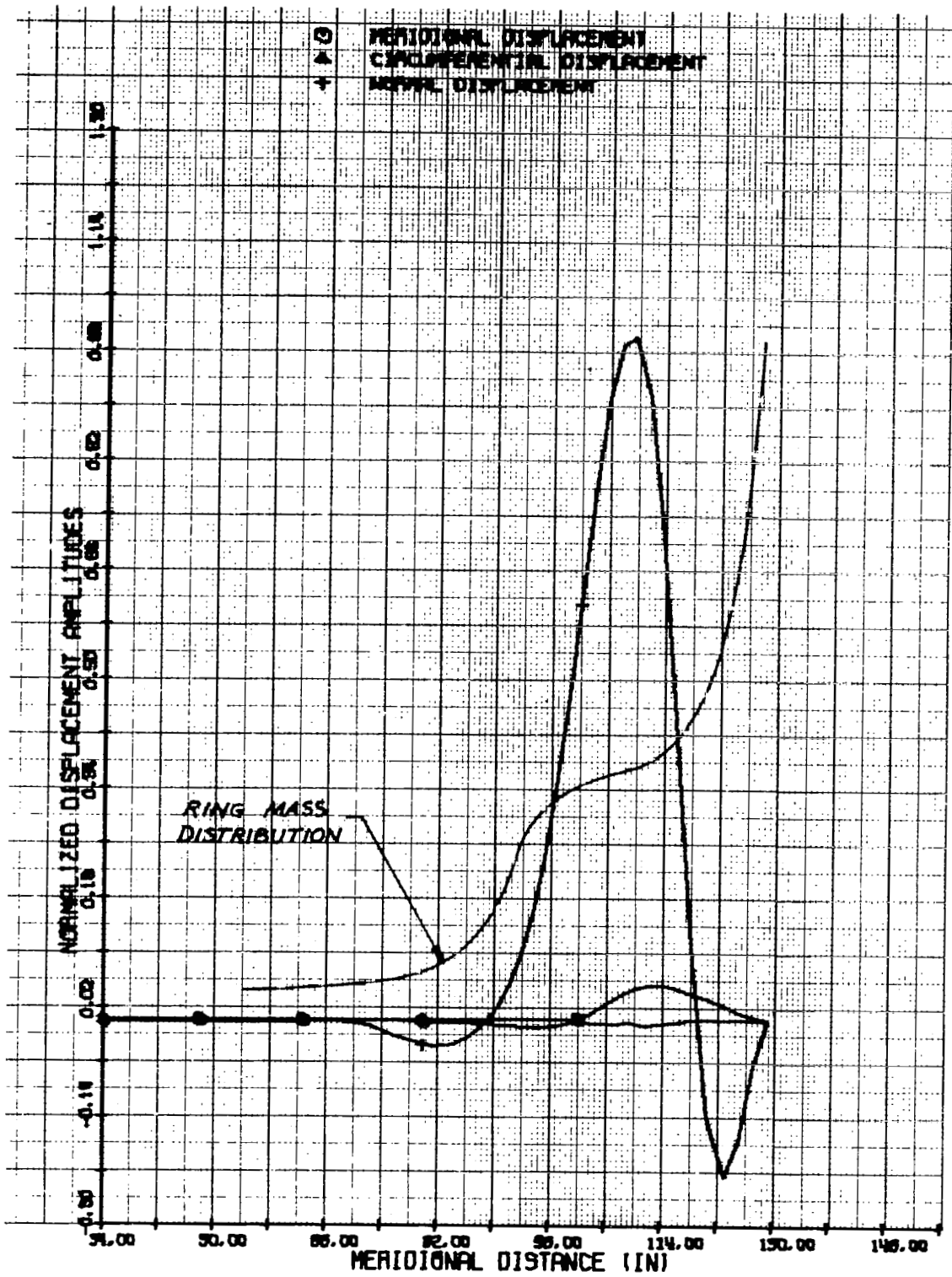


FIGURE 22. BUCKLING MODE DISPLACEMENTS, OA.833 TENSION SHELL
 (0.32 Slug/Ft², 300°F) N = 20, S.F. = 2.23

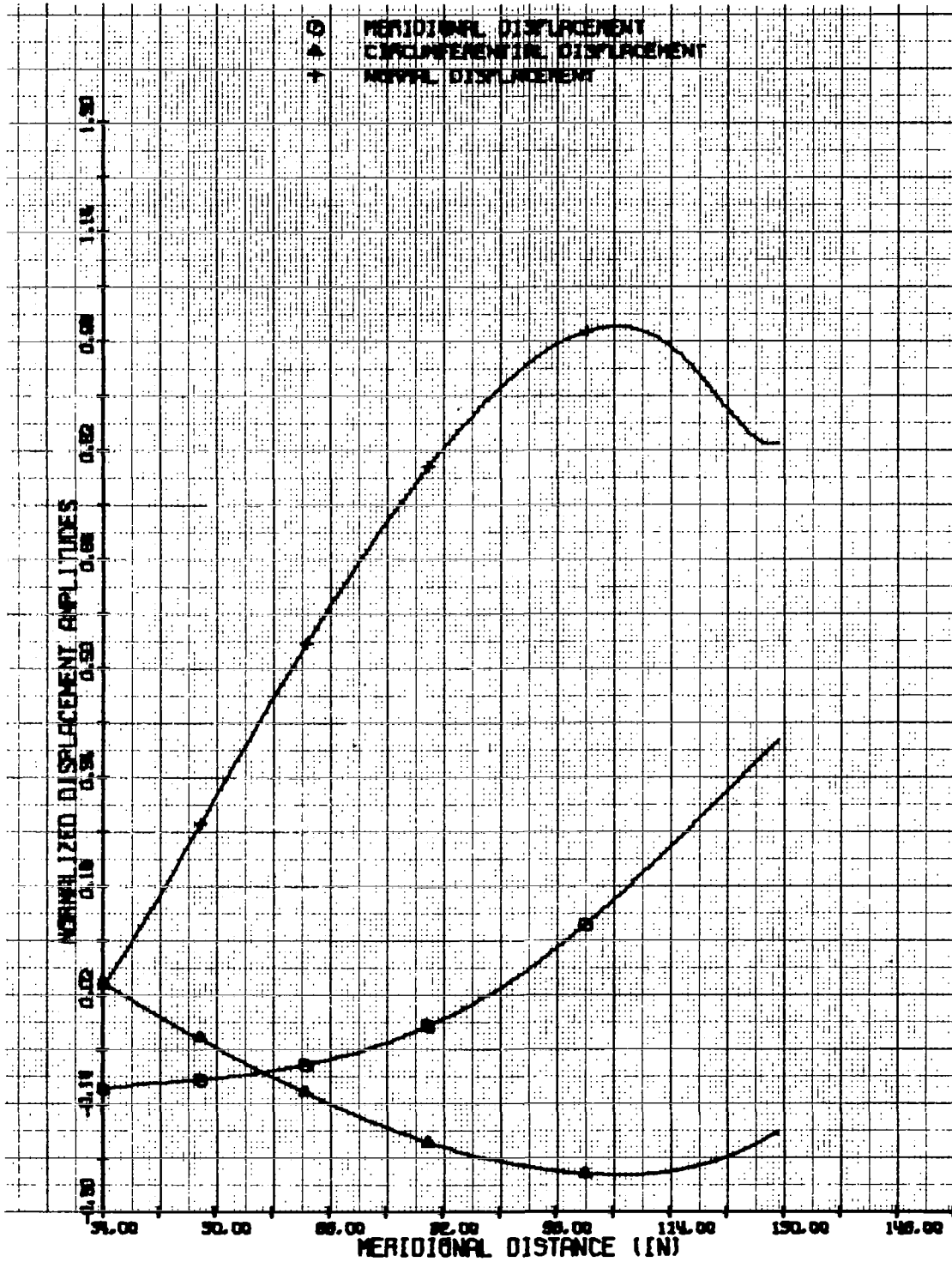


FIGURE 23. BUCKLING MODE DISPLACEMENTS, OA.833 TENSION SHELL
 (0.32 Slug/Ft², 300°F) N = 2, S.F. = 2.13

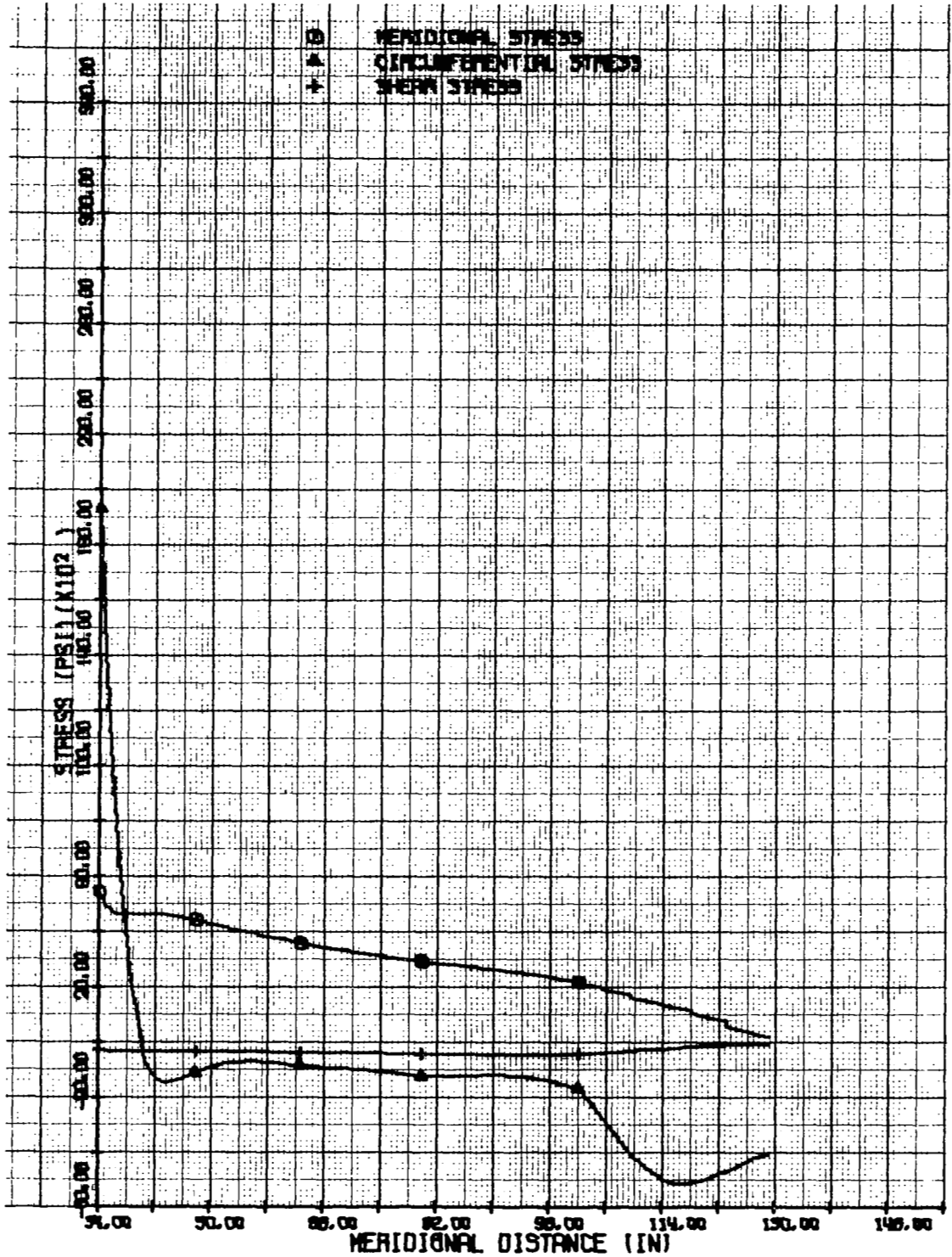


FIGURE 24. MAXIMUM SHELL STRESSES, OA.833 TENSION SHELL
 (0.32 Slug/Ft², 300°F) LAYER NO. 1 (INNER FACE) S.F. = 0.311

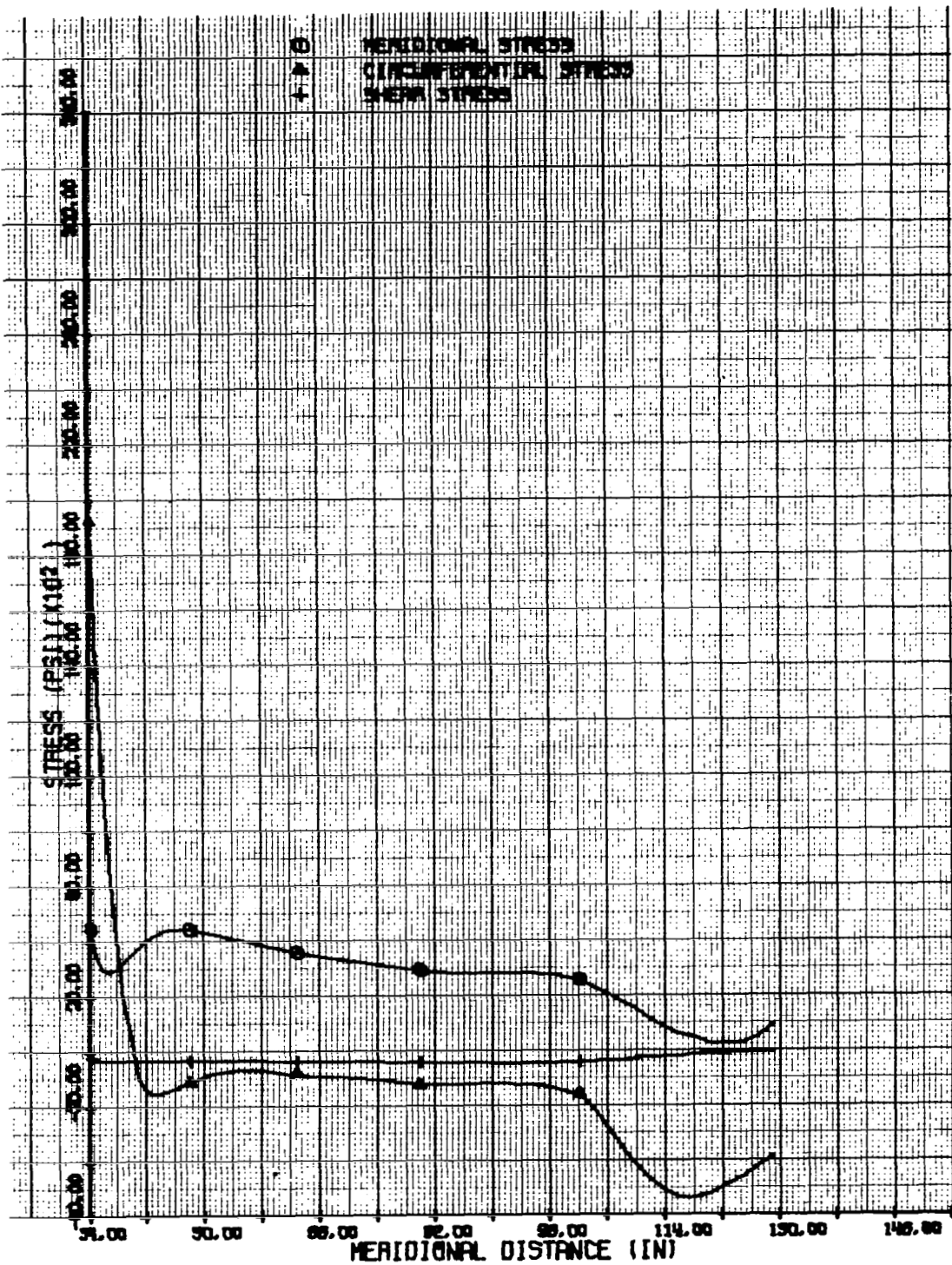


FIGURE 25. MAXIMUM SHELL STRESSES, OA.833 TENSION SHELL
 (0.32 slug/Ft², 300°F) LAYER NO. 1 (OUTER FACE) S.F. = 0.311

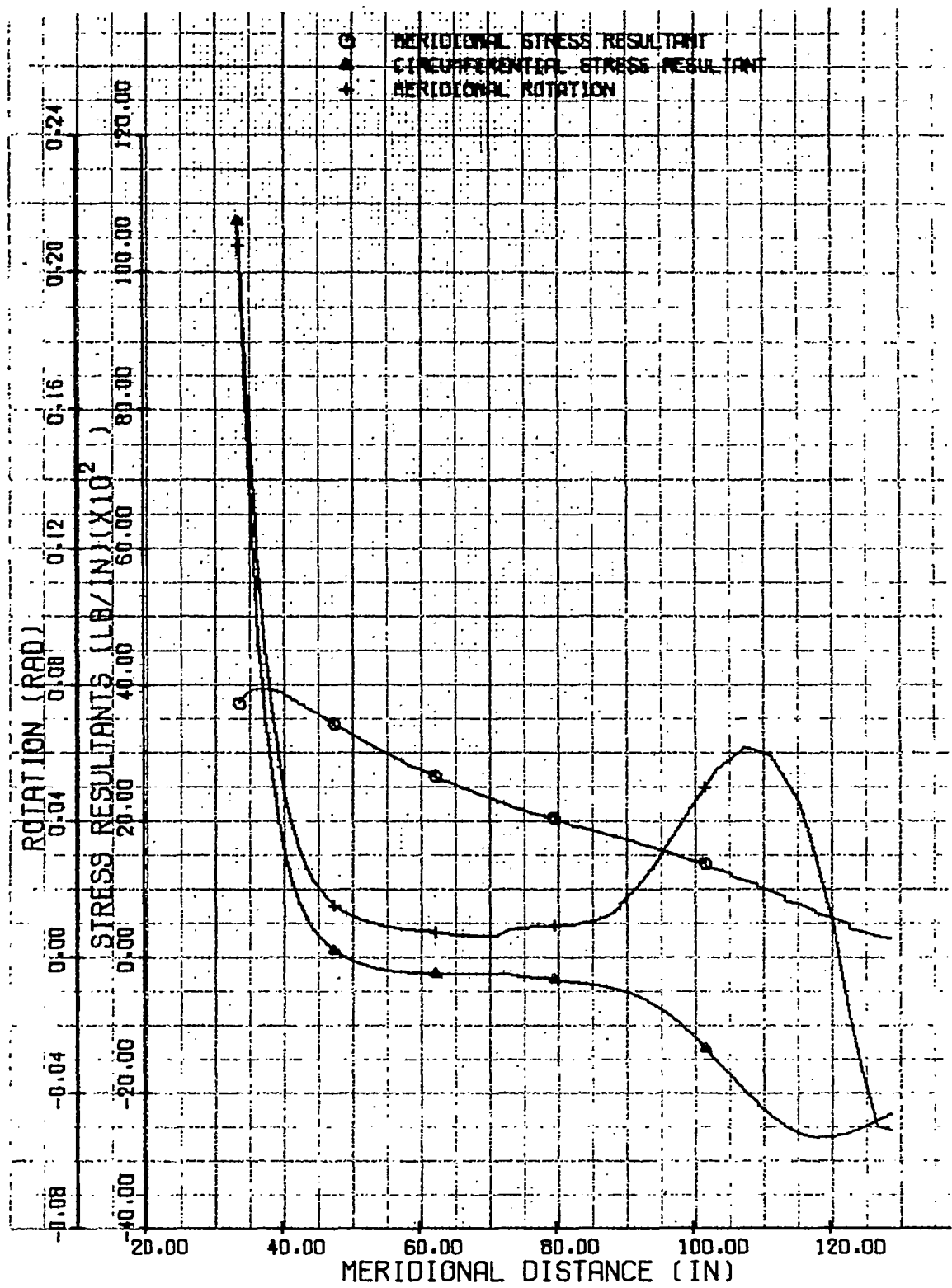


FIGURE 26. PREBUCKLING STRESS RESULTANTS AND ROTATION, OA.833
 TENSION SHELL (0.64 Slug/Ft², 300°F) S.F. = 2.25

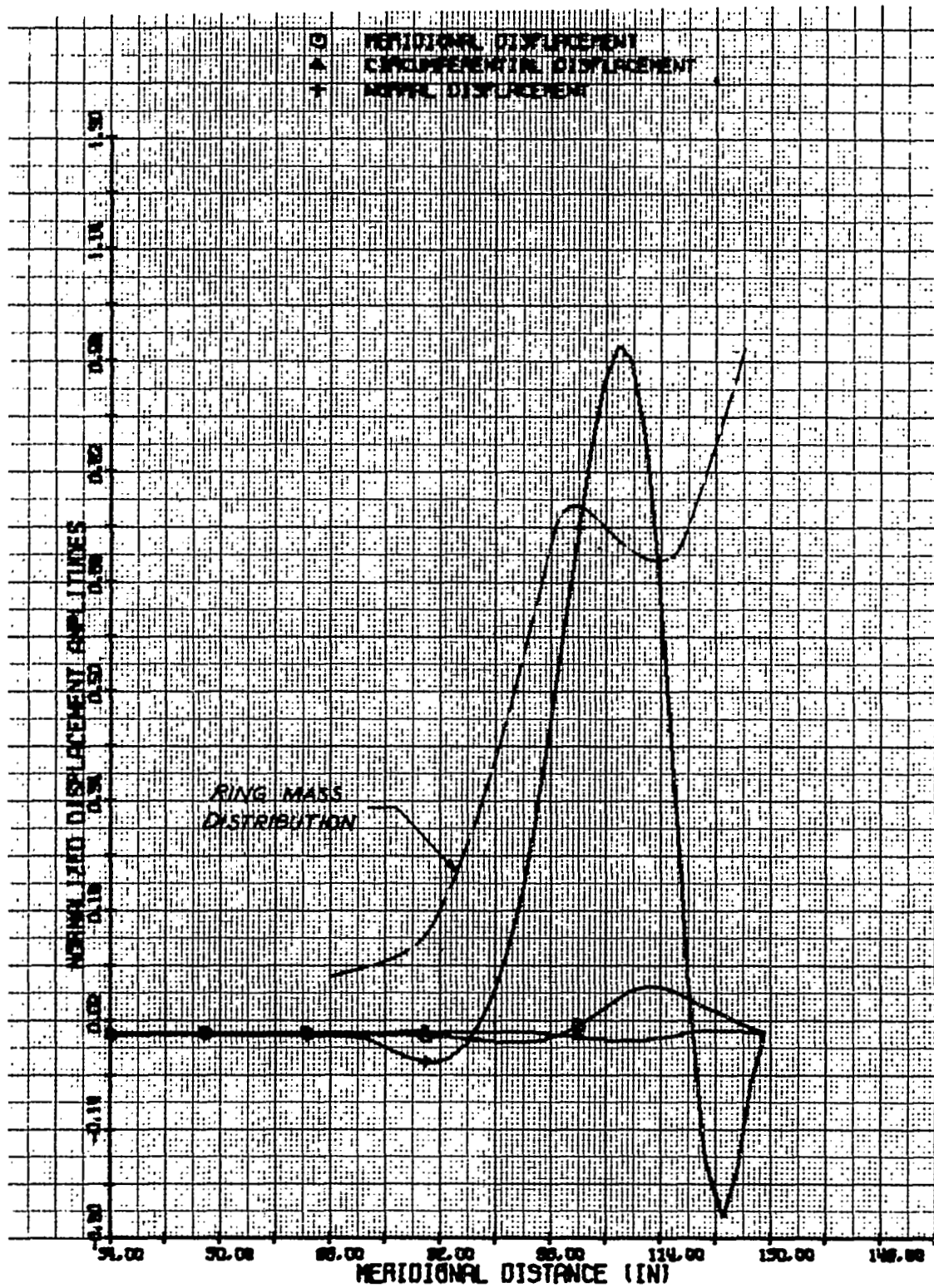


FIGURE 27. BUCKLING MODE DISPLACEMENTS, OA.833 TENSION SHELL
 (0.64 Slug/Ft², 300°F) N = 15, S.F. = 2.04

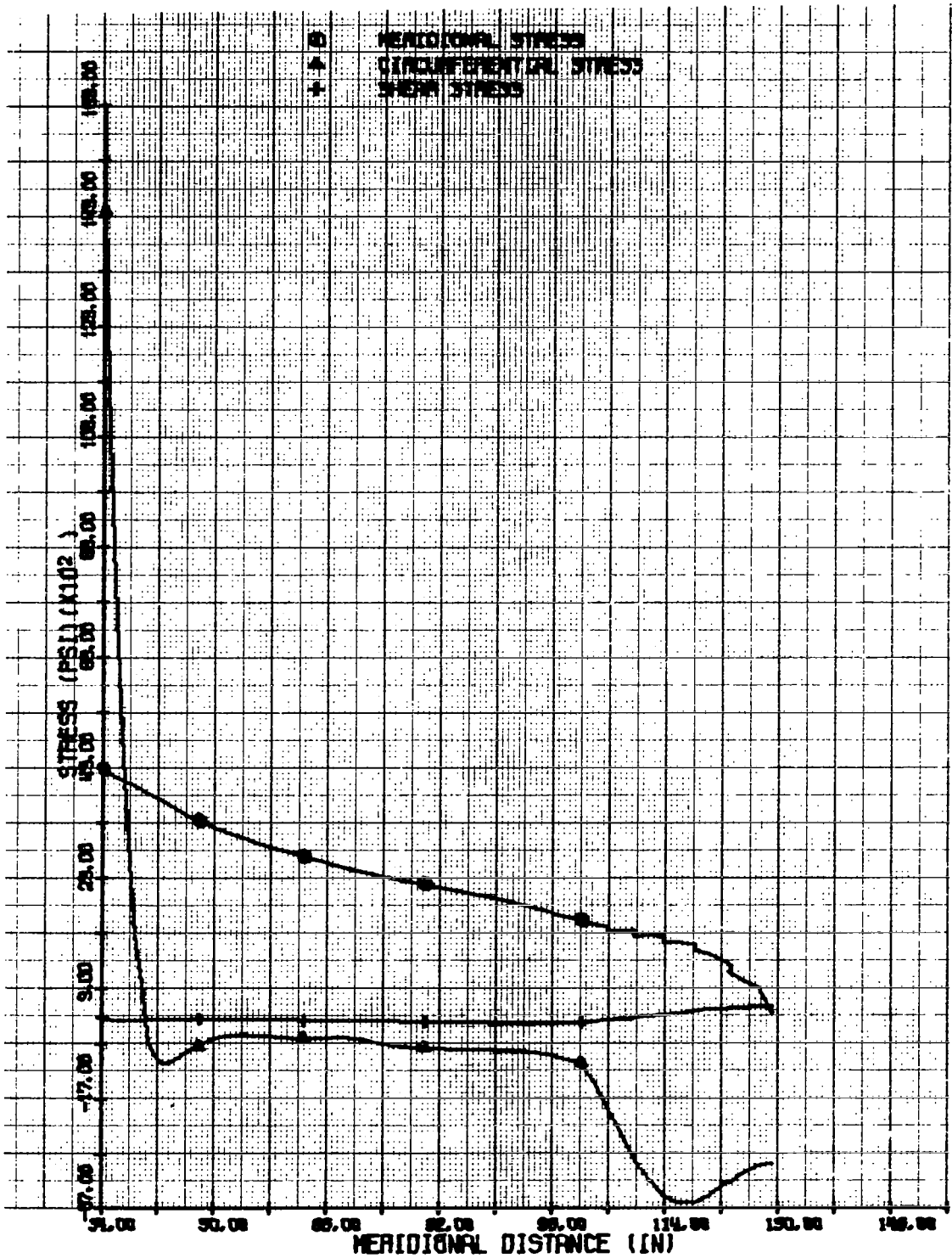


FIGURE 28. MAXIMUM SHELL STRESSES, OA.833 TENSION SHELL
 (0.64 Slug/Ft², 300°F) LAYER NO. 1 (INNER FACE) S.F. = 0.1555

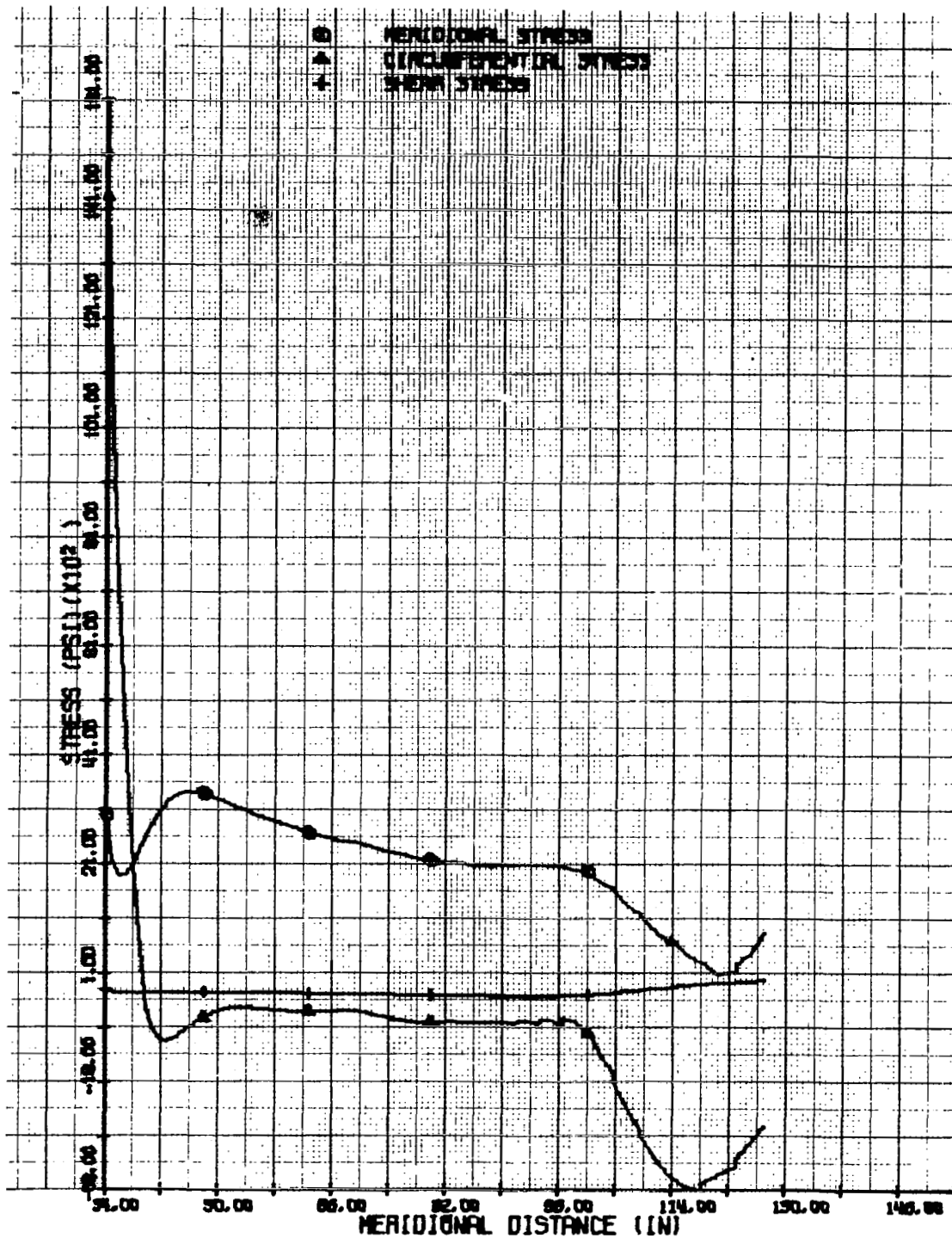
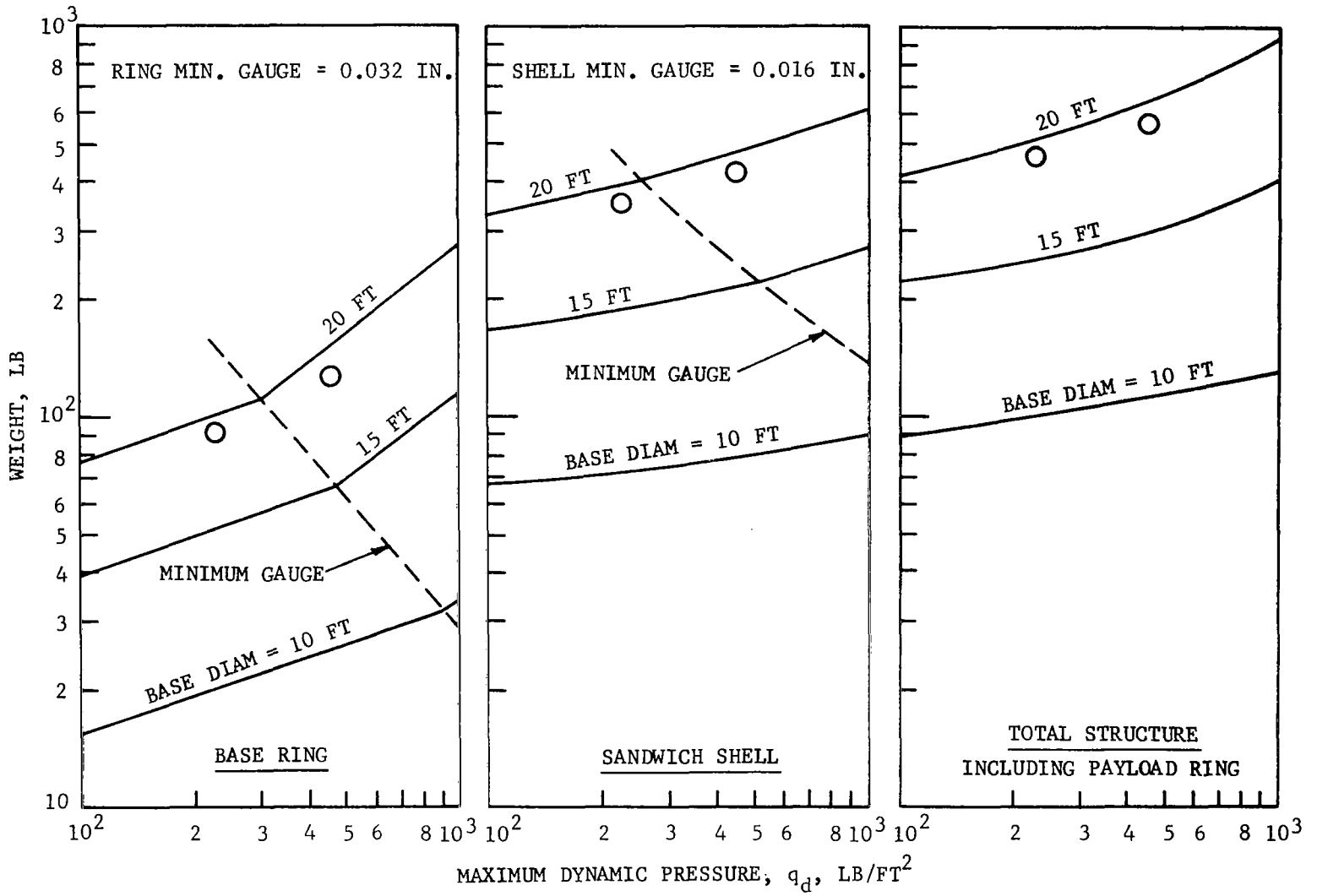


FIGURE 29. MAXIMUM SHELL STRESSES, OA.833 TENSION SHELL
 (0.64 Slug/Ft², 300°F) LAYER NO. 1 (OUTER FACE) S.F. = 0.1555

FIGURE 30. 120° CONICAL CAPSULE WEIGHT
 ALUMINUM HONEYCOMB SANDWICH, $r_p/r_B = 0.3$



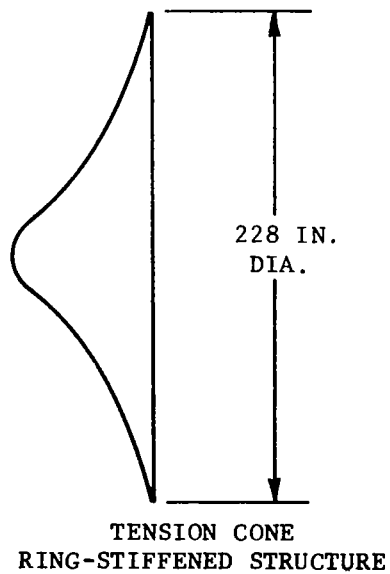
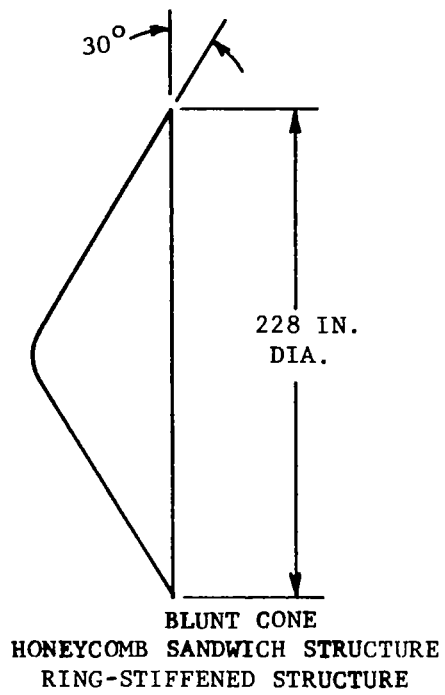


FIGURE 31. AEROSHELL CONFIGURATIONS

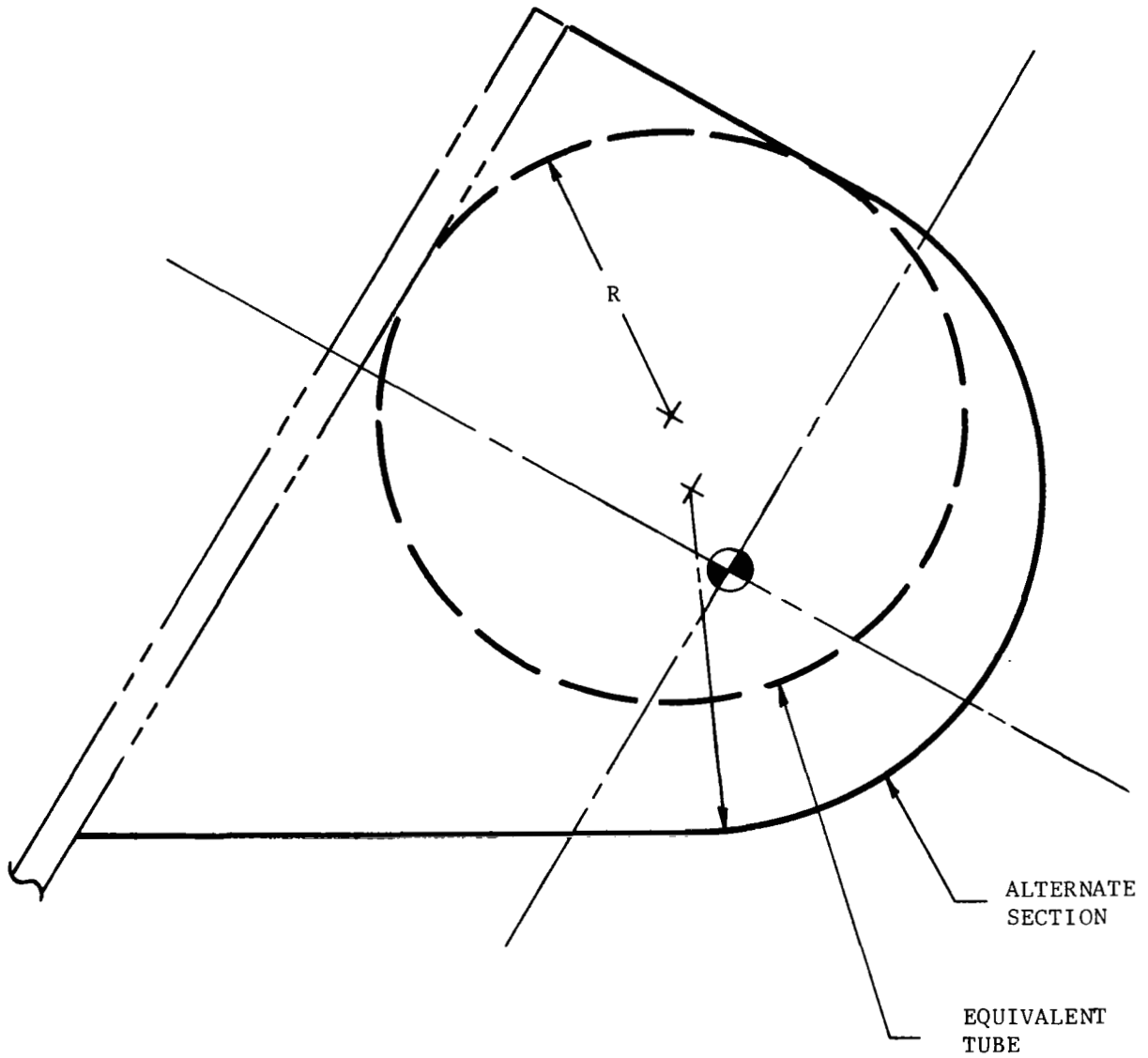
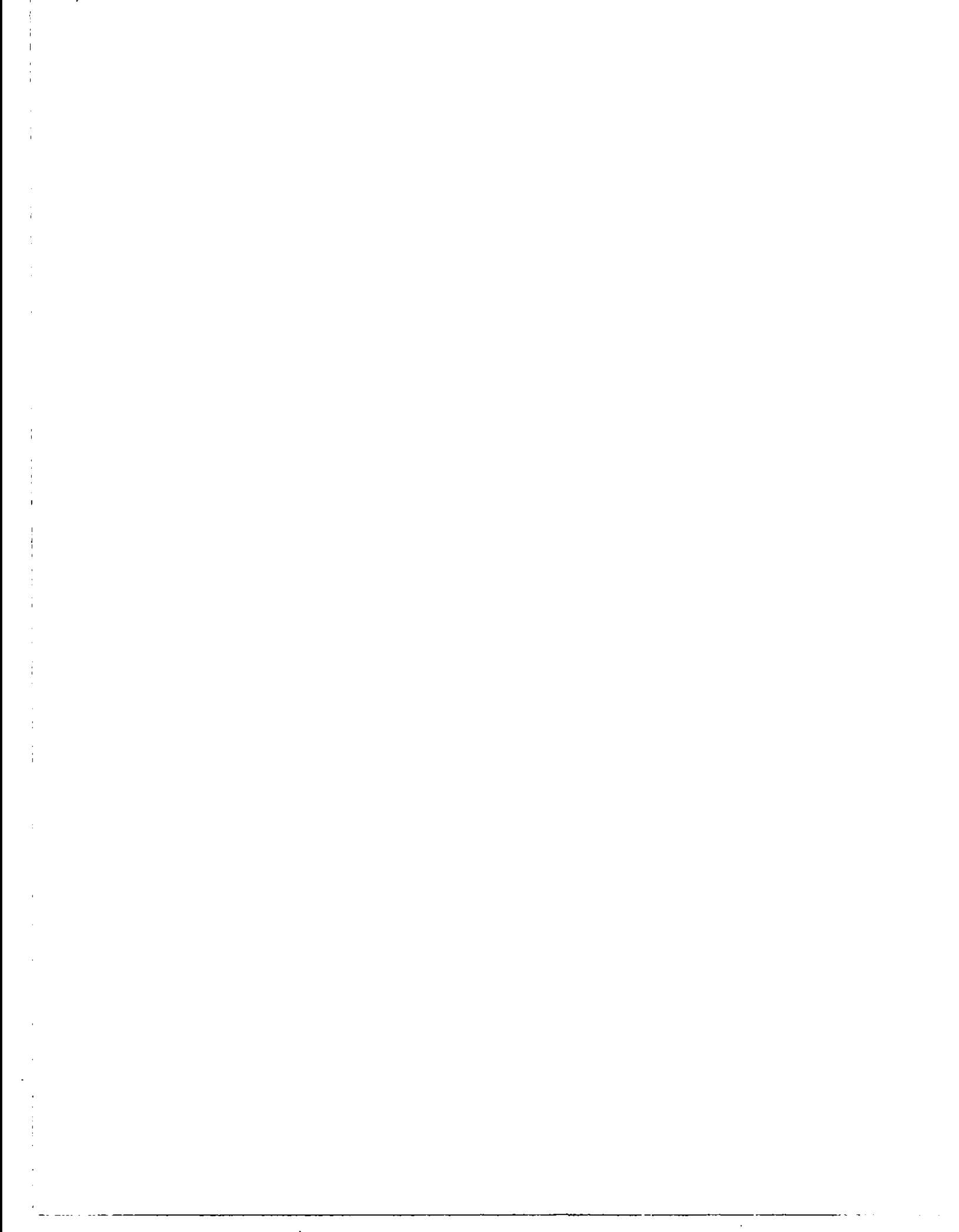
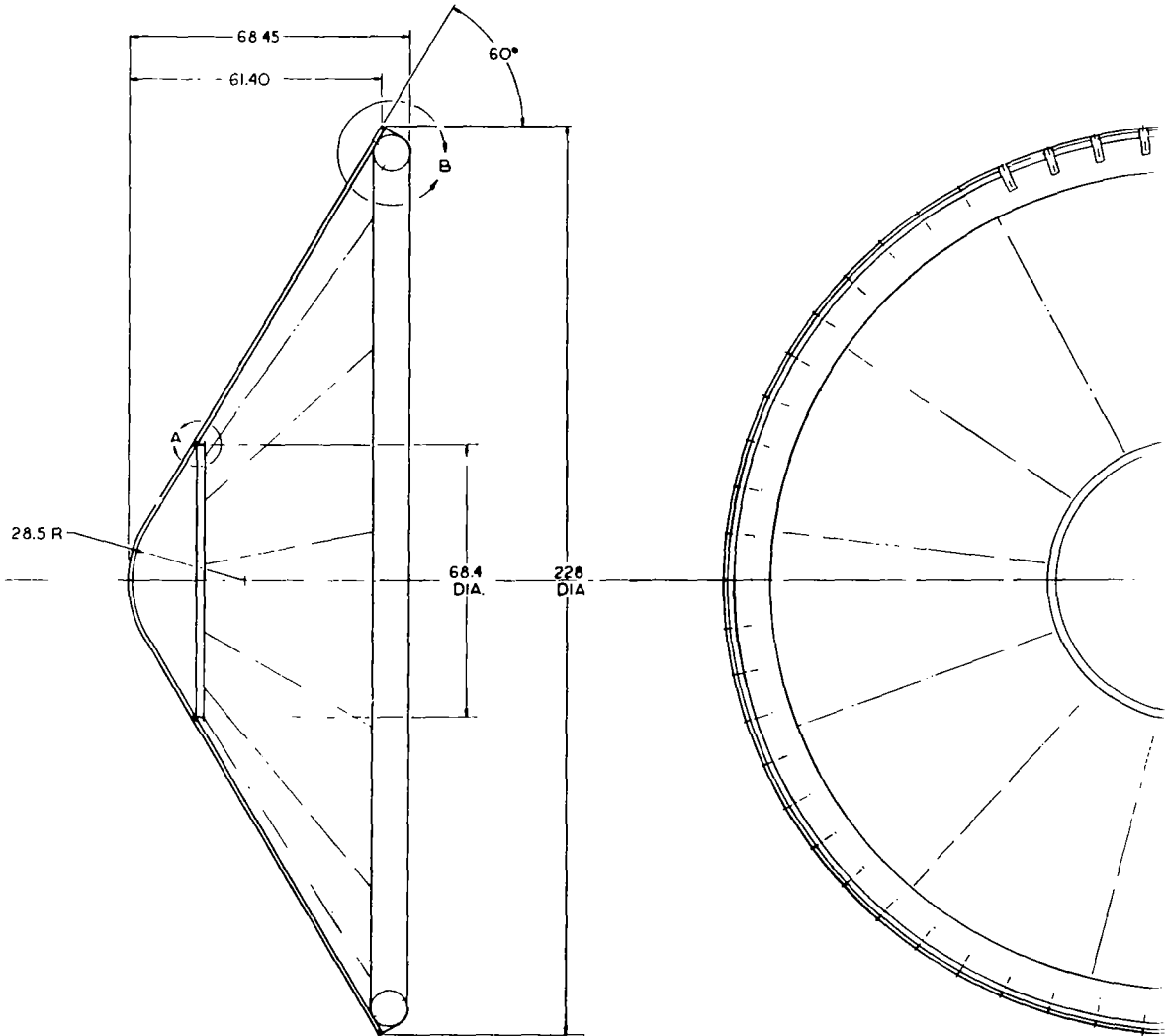


FIGURE 32. ALTERNATE BASE RING GEOMETRY





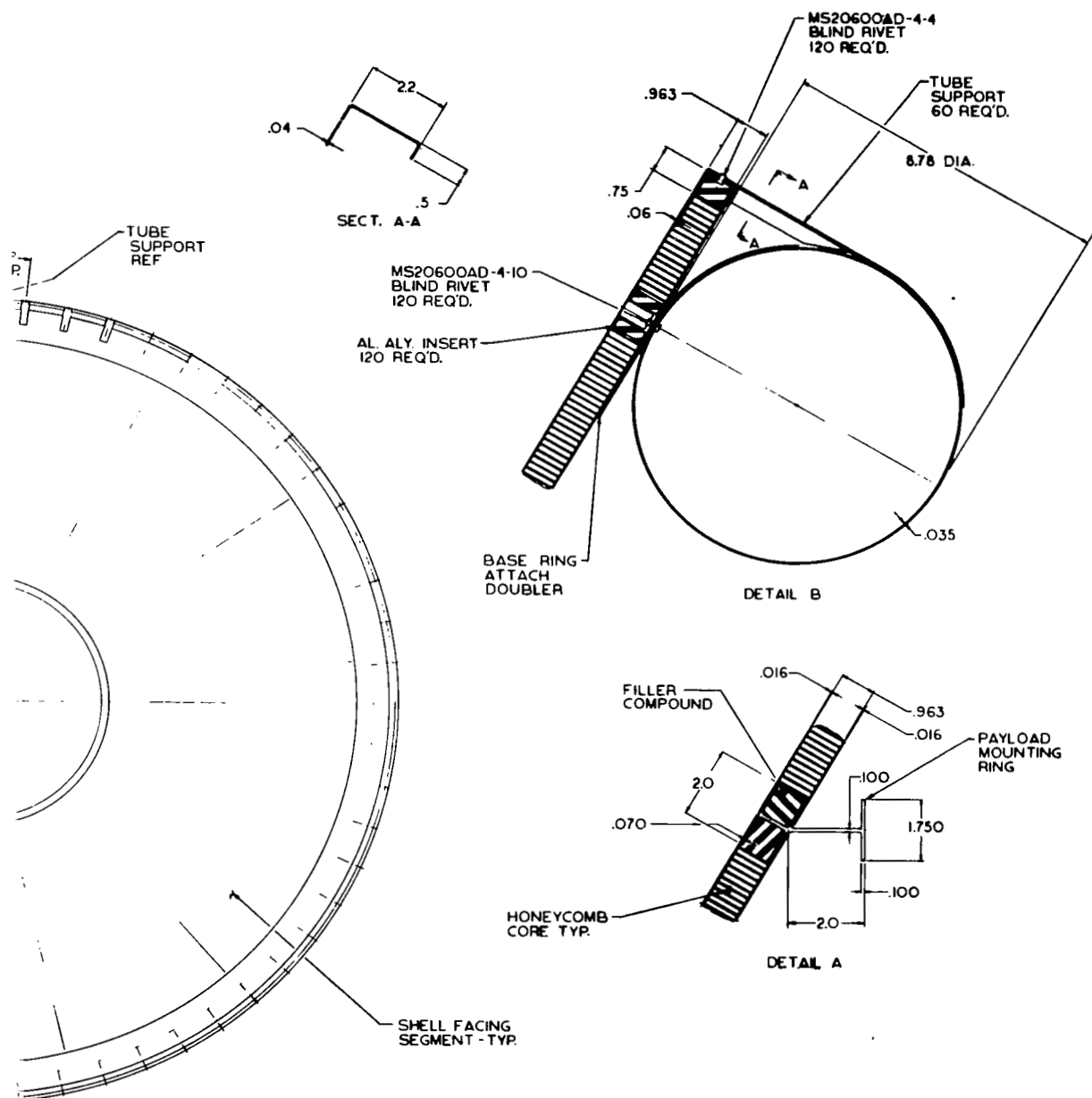
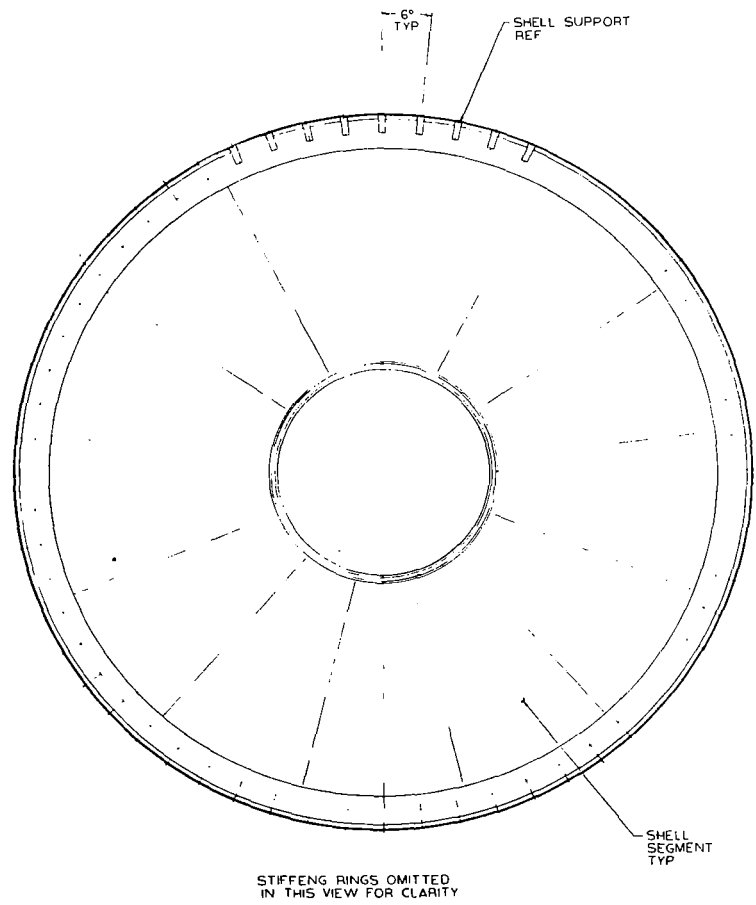
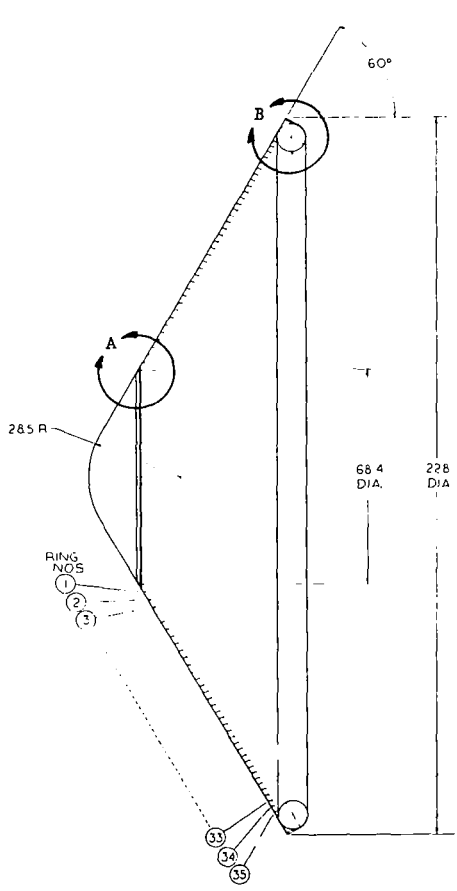


FIGURE 33. 120° HONEYCOMB SANDWICH CONE



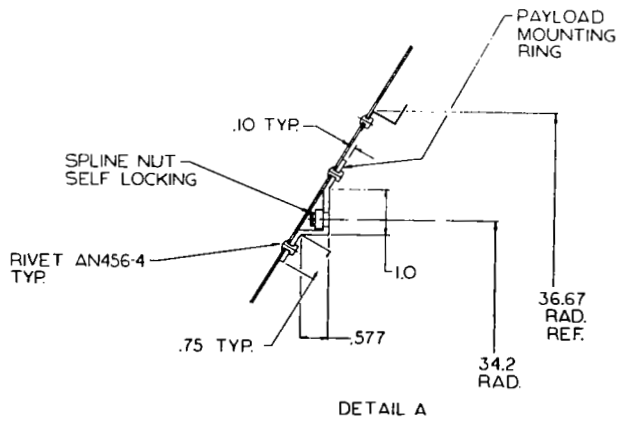
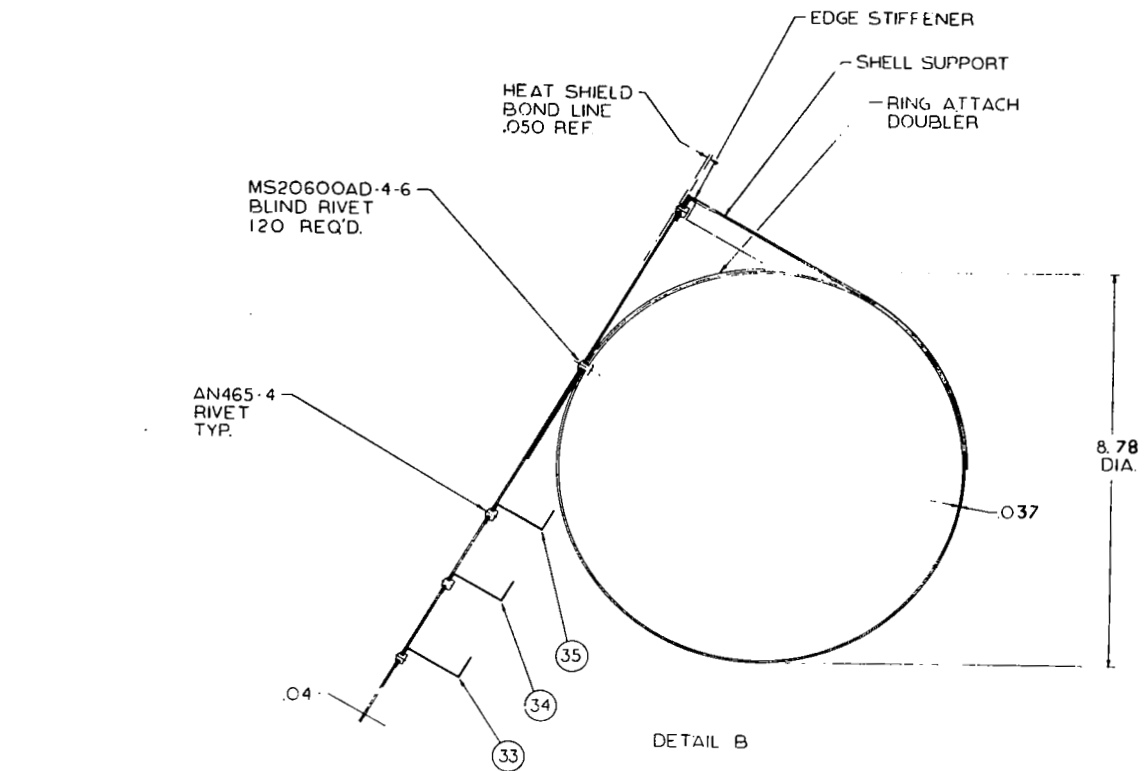
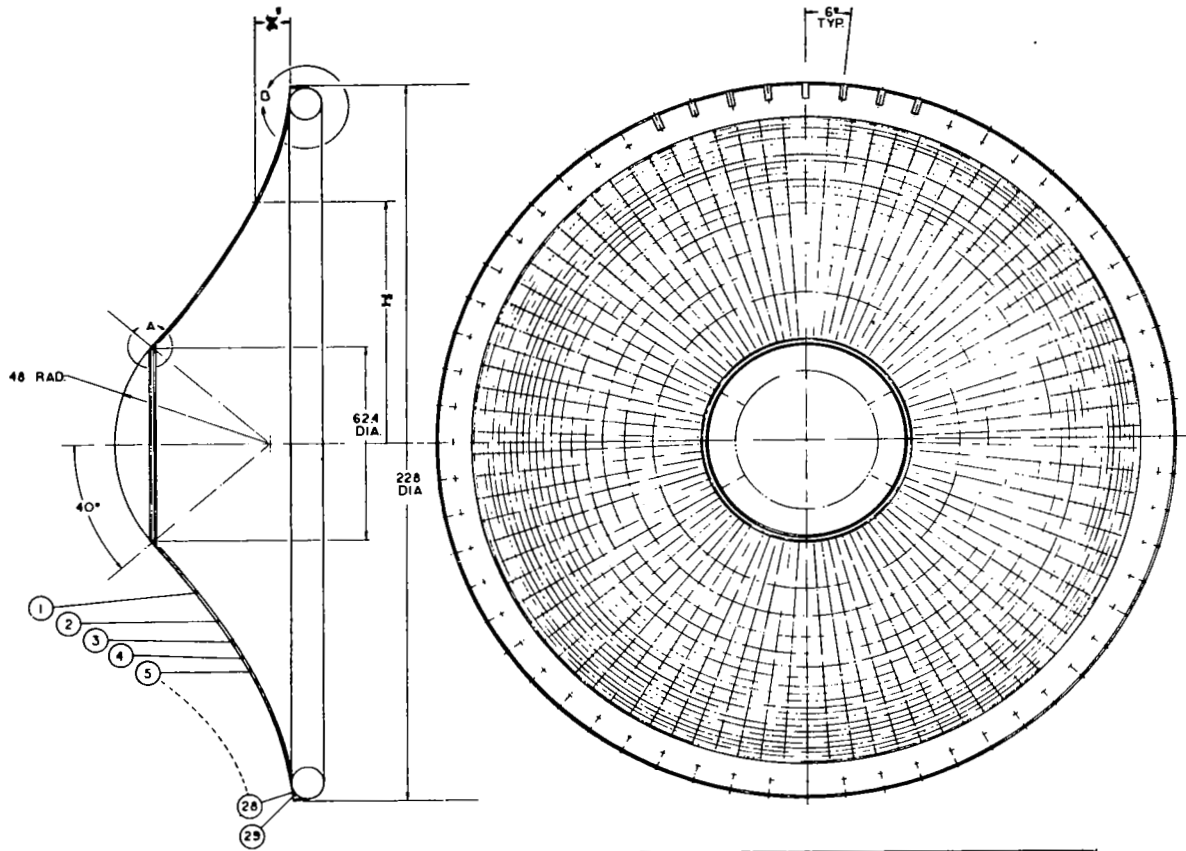
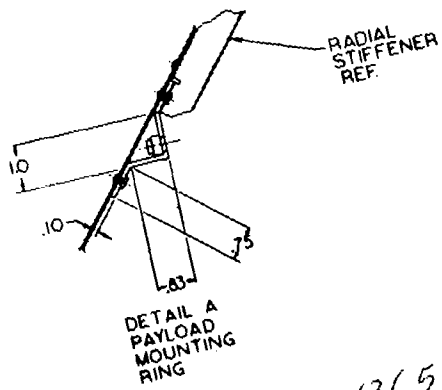
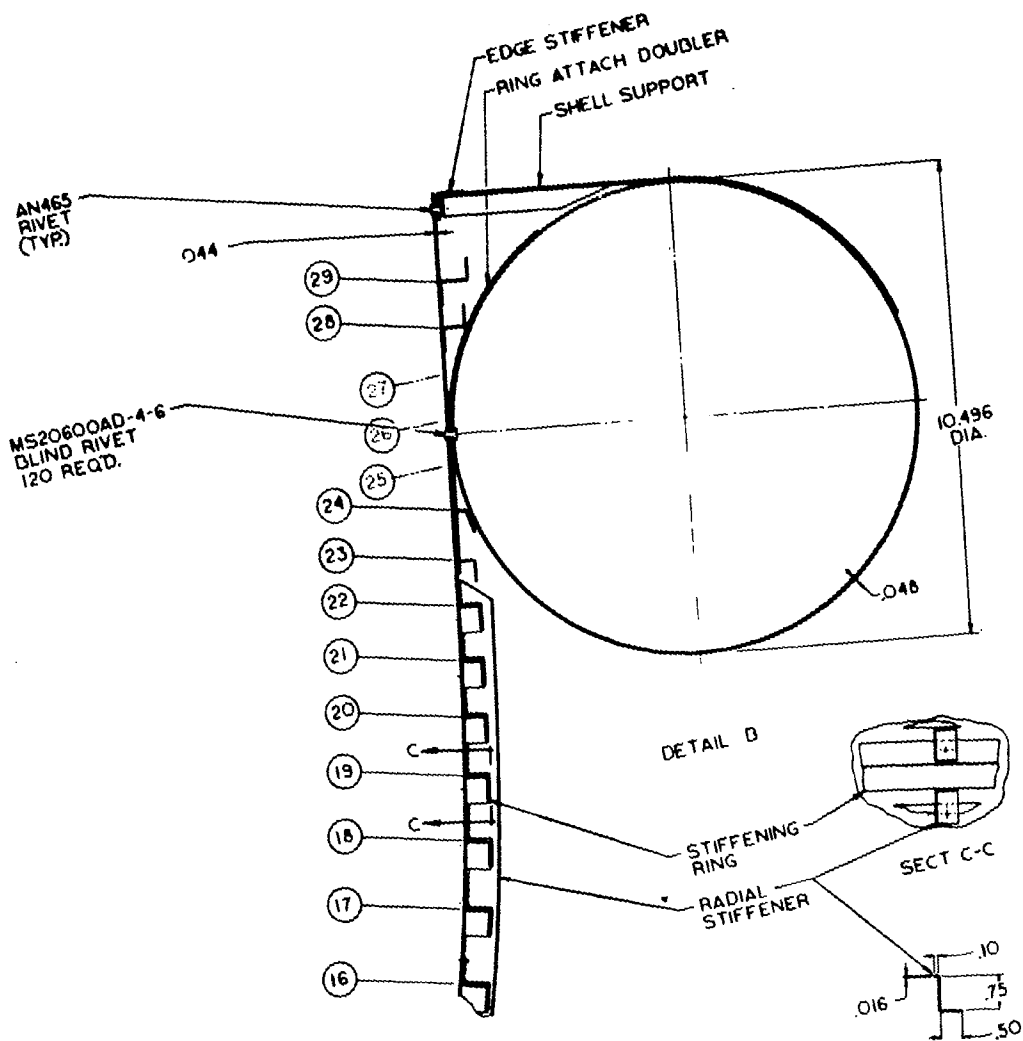


FIGURE 34. 120° RING STIFFENED CONE



Shell coordinates	
r	x'
28.5	45.9
34.2	40.9
39.8	36.2
45.4	31.7
51.3	27.5
57.0	23.4
62.6	19.5
68.4	16.1
74.1	12.8
79.7	9.5
85.5	7.4
91.1	5.1
96.9	3.2
102.6	1.8
108.2	.9
114.0	0



CR-1365

FIGURE 35. OA.833 TENSION SHELL

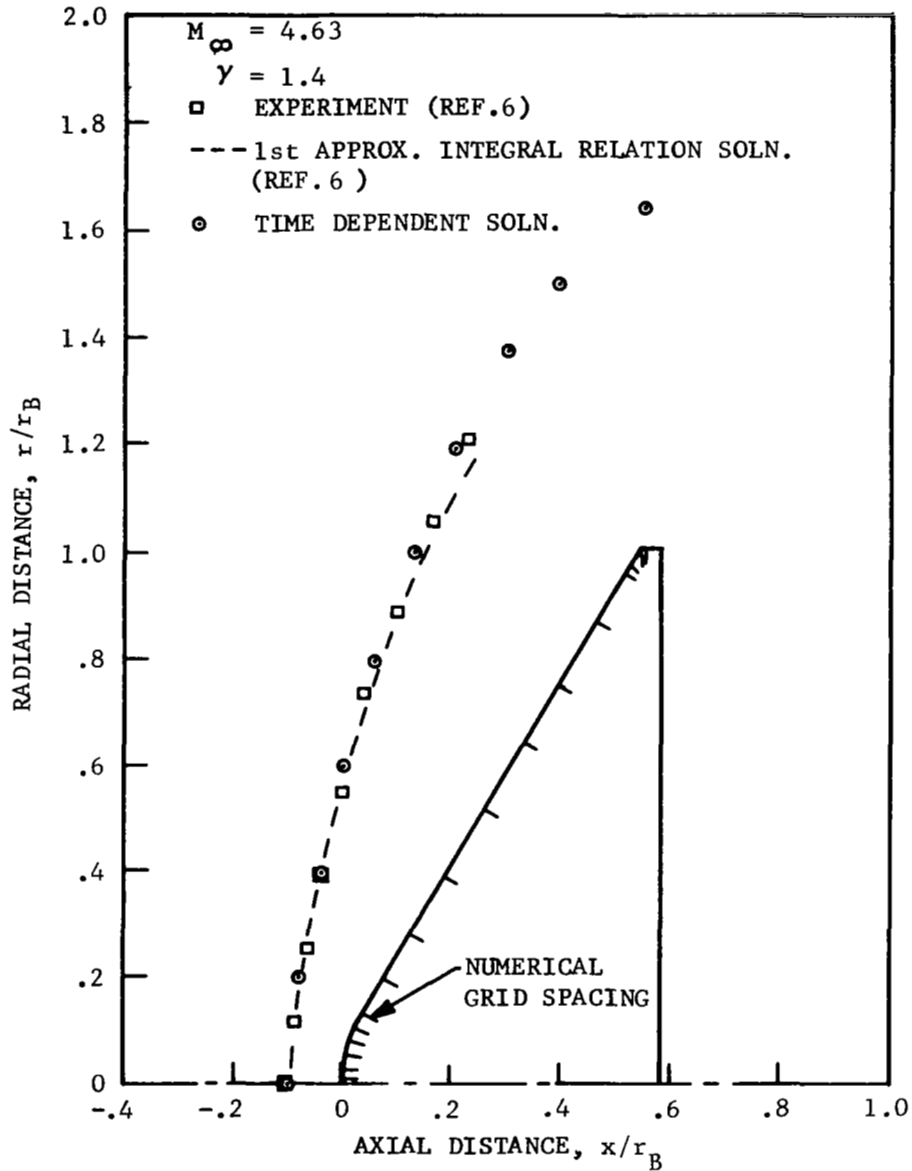


FIGURE 36. 120° SPHERE-CONE SHOCK SHAPE, $R_N/r_B = .25$, $\alpha = 0$

FIGURE 37. 120° SPHERE-CONE PRESSURE DISTRIBUTION, $R_N/r_B = .25$, $\alpha = 0$

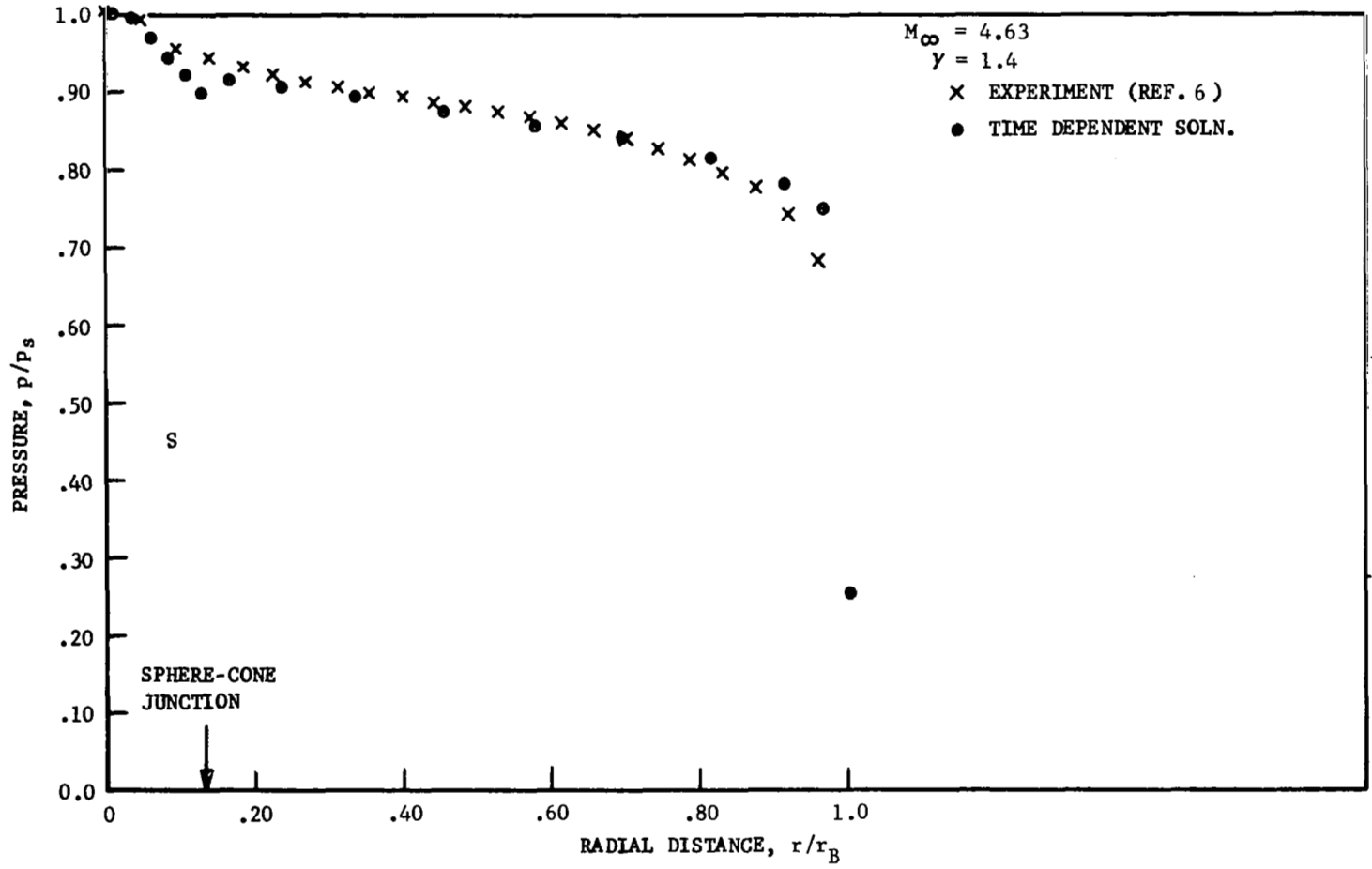


FIGURE 38. 120° SPHERE-CONE ($R_N/\tau_B = .25$) ANGLE OF ATTACK PRESSURE DISTRIBUTION, $\alpha = 10$ DEG

